Numerical Analysis of the Effect of Heterogeneity on CO2 Dissolution Enhanced by Gravity Driven Convection

yufei wang[1], Daniel Fernandez Garcia[2], and Maarten W. Saaltink[3]

[1]Universitat Politècnica de Catalunya
[2]Technical University of Catalonia
[3]Department of Civil and Environmental Engineering, Universitat Politècnica de Catalunya (UPC)

March 07, 2024

Abstract

Dissolution trapping of CO2 in brine can reduce the risk of leakage of supercritical CO2 during long-term Geological Carbon Sequestration (GCS). The dissolution of overlying gaseous CO2 into brine increases the density of brine in its upper portion, which causes gravity-driven convection (GDC) and thus significantly increases the rate of CO2 dissolution. To date, most studies on GDC-driven dissolution are based on homogeneous media and only few studies exist on the effect of heterogeneity on GDC-driven dissolution. Here, we study the effect of heterogeneity on GDC-driven dissolution rate by using numerical simulations with randomly obtained permeability fields. Dissolution rates calculated by these simulations are related to properties of the permeability field by using least-squares regression. We obtained two empirical formulas for predicting the asymptotic GDC-driven dissolution rate. In the first formula the dissolution rate is almost linearly proportional to the dimensionless equivalent vertical permeability. In the second one the dissolution rate is linearly proportional to a dimensionless vertical finger-tip velocity. Both formulas show a non-linear relation between dissolution and anisotropy with higher anisotropy giving lower dissolution rates.

Numerical Analysis of the Effect of Heterogeneity on CO_2 Dissolution Enhanced by Gravity Driven Convection

Yufei Wang[1,2] **Daniel Fernàndez-Garcia**[1,2] **Maarten W. Saaltink**[1,2]

[1]Dept. of Civil and Environmental Engineering. Universitat Politècnica de Catalunya, Jordi Girona 1-3, 08034 Barcelona, Spain
[2]Associated Unit: Hydrogeology Group (UPC-CSIC)

Key Points:

- Gravity-Driven Convection (GDC) enhances the dissolution of overlying supercritical CO_2 into brine in heterogeneous media;
- GDC-driven dissolution is almost linearly proportional to the equivalent vertical intrinsic permeability and the vertical finger velocity;
- The horizontal to equivalent vertical permeability ratio can hinder the GDC-driven dissolution.

Corresponding author: Yufei Wang, `yufei.wang@pku.edu.cn`

Abstract

Dissolution trapping of CO_2 in brine can reduce the risk of leakage of supercritical CO_2 during long-term Geological Carbon Sequestration (GCS). The dissolution of overlying gaseous CO_2 into brine increases the density of brine in its upper portion, which causes gravity-driven convection (GDC) and thus significantly increases the rate of CO_2 dissolution. To date, most studies on GDC-driven dissolution are based on homogeneous media and only few studies exist on the effect of heterogeneity on GDC-driven dissolution. Here, we study the effect of heterogeneity on GDC-driven dissolution rate by using numerical simulations with randomly obtained permeability fields. Dissolution rates calculated by these simulations are related to properties of the permeability field by using least-squares regression. We obtained two empirical formulas for predicting the asymptotic GDC-driven dissolution rate. In the first formula the dissolution rate is almost linearly proportional to the dimensionless equivalent vertical permeability. In the second one the dissolution rate is linearly proportional to a dimensionless vertical finger-tip velocity. Both formulas show a non-linear relation between dissolution and anisotropy with higher anisotropy giving lower dissolution rates.

1 Introduction

Geological Carbon Sequestration (GCS) has proved to be a feasible and necessary approach to mitigate CO_2 emissions [*Vilarrasa et al.*, 2013, 2014; *European Commission*, 2014; *Vilarrasa and Carrera*, 2015; *Tutolo et al.*, 2014, 2015a,b; *Celia et al.*, 2015]. GCS consists of sequestering CO_2, separated from other gases at large point sources (e.g., thermal power plants), into geological brine formations [*Vilarrasa et al.*, 2010; *Brainard*, 2018; *Matacic*, 2018]. The injected CO_2, usually in supercritical state under reservoir condition, is expected to flow over the denser brine during the process of injection, and continuously move upwards and accumulate beneath a low permeability caprock after injection. Because the less dense CO_2 is immiscible but can dissolve in the resident brine, the injected CO_2 is sequestered by four mechanisms: (1) by being sealed under the low permeability caprock (hydrodynamic trapping), (2) by being trapped by capillarity (residual trapping), (3) by dissolving into the brine at the CO_2-brine interface (dissolution trapping) and (4) by reacting with rock formation (mineral trapping) [*Kumar et al.*, 2005; *Riaz et al.*, 2006; *Bachu et al.*, 2007; *Gasda et al.*, 2011, 2012; *Macminn and Juanes*, 2013; *Soltanian et al.*, 2017]. Hydrodynamic trapping is the fastest mechanism but is unstable, because the relatively light CO_2 can escape from the reservoir in case of seismic activity, faults or failing wellbore casings [*Vilarrasa*, 2012]. Mineral trapping is most stable but slow and usually negligible [*Baines and Worden*, 2004; *Saaltink et al.*, 2013; *Sathaye et al.*, 2014]. During the later stage of injection, the safety of the GCS is governed by the dissolution trapping, which is not affected by the non-integrity (e.g., faults) of the formation [*Strandli and Benson*, 2013; *Nicot*, 2008]. Therefore, the dissolution of CO_2 into brine is an important indicator to evaluate the safety of long-term CO_2 sequestration [*Anbar and Akin*, 2011; *Xiao et al.*, 2019].

The dissolution process is enhanced by Gravity-Driven Convection (GDC) [*Lindeberg and Wessel-Berg*, 1997; *Lindeberg and Bergmo*, 2003; *Lindeberg and Wessel-Berg*, 2011; *Tsai et al.*, 2013; *Sathaye et al.*, 2014]. Dissolution of the overlying CO_2 into the brine increases the brine density in the upper portion of the saline formation creating an unstable situation with more dense on top of less dense brine. This causes nonuniform GDC in the brine phase and enhances the downward movement of CO_2-saturated brine [*Weir et al.*, 1996; *Vella and Hupper*, 2006; *Pritchard*, 2007; *Pruess and Zhang*, 2008]. Moreover, the nonuniform downward flux of CO_2-saturated brine is accompanied by an upward flux of CO_2-unsaturated brine, increasing the contact between CO_2-rich phase and unsaturated brine, which further accelerates CO_2 dissolution [*Pruess*, 2005; *Gilfillan et al.*, 2009; *Elenius and Gasda*, 2021]. In contrast to pure molecular diffusion, which quickly fades away as the concentration profile reaches a Gaussian distribution, the GDC can fuel the vertical mass exchange at a high constant rate for a certain long time until the whole domain is close to full CO_2 saturation [*Pau et al.*, 2010; *Slim*, 2014]. Because the dissolution rate enhanced by

GDC can significantly reduce the amount of supercritical CO_2, thus reducing the possibility of leakage, a good understanding of this dissolution is essential [*Elenius et al.*, 2015].

Currently, a large quantity of studies exists on GDC-driven dissolution, ranging from theoretical analysis [e.g., *Elenius et al.*, 2012; *Emami-Meybodi*, 2017], laboratory experiments [e.g., *Neufeld et al.*, 2010; *Rasmusson et al.*, 2017; *Salibindla et al.*, 2018], numerical simulations [e.g., *Chen et al.*, 2013; *Elenius et al.*, 2015] to field observations [e.g., *Sathaye et al.*, 2014]. It is found that GDC depends to a large extent on properties of the formation (e.g., the permeability and porosity) and of the brine phase (e.g., the relation between brine density and concentration of dissolved CO_2, viscosity and molecular diffusion coefficient) [*Hassanzadeh et al.*, 2007, 2008; *Neufeld et al.*, 2010; *Elenius and Johannsen*, 2012; *Emami-Meybodi and Hassanzadeh*, 2015]. For instance, researchers find a linear relation between the dissolution rate and the intrinsic permeability for isotropic homogeneous media [*Rasmusson et al.*, 2015]. However, most of the current researches and conclusions are limited to (isotropic or anisotropic) homogeneous fields [e.g. *Ennis-King and Paterson*, 2005; *Pruess and Nordbotten*, 2011; *Cheng et al.*, 2012; *De Paoli et al.*, 2017; *Ranganathan et al.*, 2012; *Taheri et al.*, 2012].

Studies on heterogeneous fields are usually limited to qualitative analysis of the effect of heterogeneity [*Agartan et al.*, 2015; *Lin et al.*, 2016; *Soltanian et al.*, 2017; *Kim et al.*, 2019; *Yan et al.*, 2019; *Wang et al.*, 2021; *Elgahawy and Azaiez*, 2021]. Heterogeneity in permeability plays an important role in onset, growth, maintenance and decay of the GDC and the dissolution rate [*Schincariol et al.*, 1997; *Simmons et al.*, 2001]. *Frykman and Wessel-Berg* [2014] show that we may overestimate the effects of instability in a real heterogeneous field simply by conducting numerical simulations using a homogeneous field of equivalent permeability. *Prasad and Simmons* [2003] find that while it can trigger early instability, heterogeneity can reduce the instability by dissipating the density fingers through disordered high permeability pathways at a later stage.

Although several researches attempt to quantitatively analyze the relation between GDC and field properties for heterogeneous media, only a few offer explicit formulas between the GDC-driven dissolution rates and permeability heterogeneity. For instance, *Farajzadeh et al.* [2011] and *Kong and Saar* [2013] conducted numerical simulations of GDC in isotropic heterogeneous media, but did not offer a quantitative formula between CO_2 dissolution rates and heterogeneity measures. Therefore, conclusions from these researches cannot be directly applied to estimate the dissolution rate in real reservoirs. Several researches offer quantitative formulas for predicting dissolution rates but only consider simplified binary heterogeneous media [*Elenius and Gasda*, 2013; *Green and Ennis-King*, 2014] or homogeneous media with anisotropic permeability [*Erfani et al.*, 2022]. In these researches, different conclusions are given regarding the effect of permeability anisotropy on the dissolution rate.

Overall, we have a solid understanding of the GDC-driven dissolution process in isotropic homogeneous media, but the GDC-driven dissolution in heterogeneous media needs further study. Especially, we need to quantitatively clarify the impact of the anisotropy ratio on the effective dissolution rate. Moreover, the current predictors are all based on the (equivalent) permeability, and it remains unclear whether we can predict the dissolution rate based on other formation properties or field observations, such as the finger-tip velocity.

Therefore the objective of this work is to quantitatively analyze the effect of permeability heterogeneity on the GDC-driven dissolution rate in a wide range of (isotropic and anisotropic) heterogeneous fields with varying degrees of heterogeneity. We do this in two steps. The first step consists of performing numerical simulations over a large number of heterogeneous fields of different permeability distributions. Numerical simulations are carried out by a finite-difference numerical program developed by *Wang* [2022]. Permeability fields are generated with the sequential Gaussian simulation method implemented in the SGSIM code [*Journel and Huijbregts*, 1976]. In the second step the results of the simulations are analyzed to find relations between the GDC-driven dissolution rate and heterogeneity of permeability, and we compare our results against those given in literature. In this step, ordinary-least-squares linear regressions are used.

The rest of this paper is organized as follows. Section 2 gives a concise description of GDC. In section 3, we review existing formulas for GDC driven dissolution rates. Section 4 describes the computational approach. Section 5 gives the results and discussions. Major conclusions are listed in section 6.

2 Gravity-Driven Convection

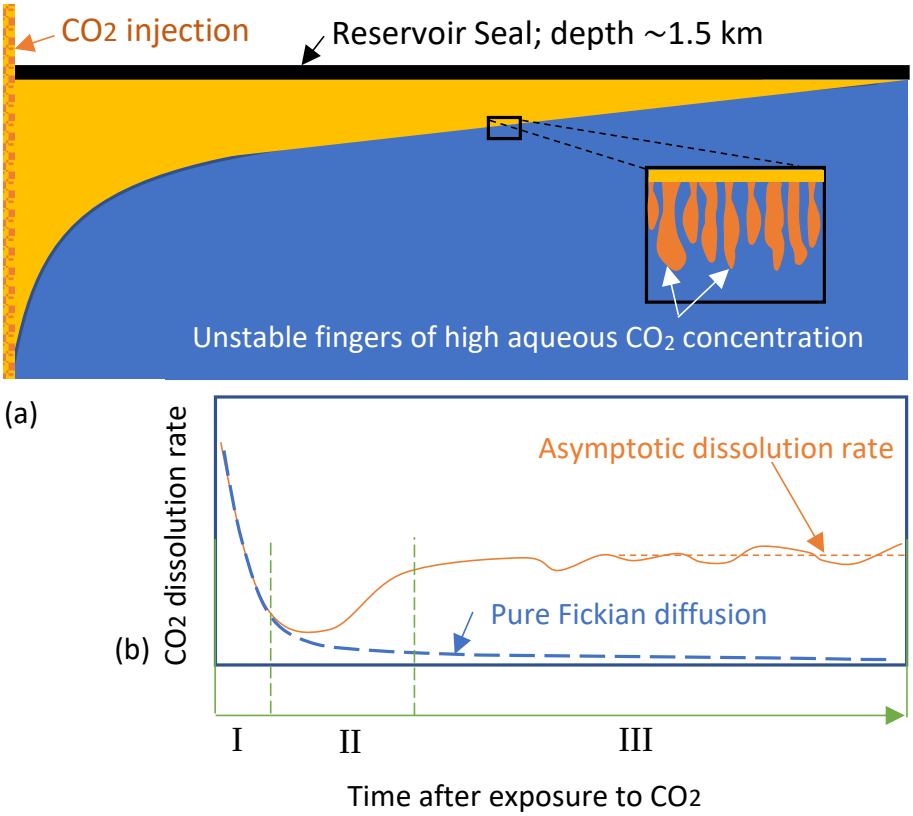

Figure 1: (a) Sketch of the appearance of unstable fingers at the interface of brine and CO_2-rich phase, and (b) enhanced dissolution rate due to vertical mass exchange driven by unstable fingers (I: diffusive regime; II: flux-growth regime; and III: constant-flux regime).

During the later stage of injection, the injected less dense CO_2-rich phase floats over the brine, as shown in Figure 1. This CO_2 moves upwards until it reaches a sealing caprock that traps the CO_2. The trapped CO_2 remains stored in the reservoir over extended periods, contributing to long-term carbon storage. Far from the injection site, a long quasi horizontal interface forms between the brine phase and the CO_2-rich phase. This interface represents a boundary of constant CO_2 concentration for the underlying brine, from which the overlying supercritical CO_2 dissolves into the brine. Importantly, brine with high CO_2 concentration has $\sim 1.0\%$ higher density than the underlying brine of very low CO_2 concentration, triggering Gravity-Driven Convection (GDC) that remarkably increases the CO_2 dissolution rate (see Figure 1). GDC continues until the whole reservoir is fully saturated with CO_2, which may take a long time. The dis-

solution process can be divided into 4 regimes [*Slim*, 2014; *Tsinober et al.*, 2022]. The first regime is called 'diffusive regime', in which the mass flux is controlled by Fickian diffusion that fades away exponentially, as can be seen from Figure 1. After this, GDC starts to develop and dissolution switches from diffusion controlled to convection controlled. During this regime, which is called 'flux-growth regime', the dissolution rate starts to increase. Once the GDC is fully developed, the dissolution rate reaches a quasi constant value for a relatively long time. This regime is known as 'constant-flux regime'. The last regime (not shown in Figure 1) is referred to as 'shutdown regime' or flux decay regime. In this regime, the dissolution rate decreases as the reservoir becomes fully saturated with CO_2 [*Elenius et al.*, 2015].

In this work, we focus on the dissolution rate taking place in the 'constant-flux regime'. This regime controls the overall behavior of the dissolution efficiency during the geological carbon sequestration [*Tsinober et al.*, 2022]. In this 'constant-flux regime', the dissolution rate can be approximated by an asymptotic dissolution rate, as shown in Figure 1.

3 Review of Formulas for GDC-Driven Dissolution Rates

In isotropic homogeneous porous media, the asymptotic dissolution rate [kg·m^{-2}·s^{-1}] can be written as [e.g., *Hesse*, 2008; *Pau et al.*, 2010; *Slim*, 2014],

$$F_\infty = \gamma X_0^C \rho_0 \frac{\Delta\rho g \kappa}{\overline{\mu}}, \tag{1}$$

where γ [-] is a scaling coefficient, X_0^C [kg·kg^{-1}] and ρ_0 [kg·m^{-3}] respectively represent the CO_2 mass fraction in brine and the brine density at the interface of brine and CO_2-rich phase, $\Delta\rho$ [kg·m^{-3}] is the density increase when aqueous CO_2 mass fraction increases from the initial very small background value to X_0^C, g [m·s^{-2}] is the gravitational acceleration, κ [m^2] is the intrinsic permeability, and $\overline{\mu}$ [pa·s] is the mean viscosity of brine. Different researches have obtained different values for the scaling coefficient γ that varies from ~ 0.015 to ~ 0.075, and a summary of γ is given in Table 1.

In heterogeneous porous media, the intrinsic permeability can vary by several orders of magnitude [*Elenius and Johannsen*, 2012; *Elenius et al.*, 2012]. Therefore, it is important to understand the effect of permeability heterogeneity on the GDC dissolution. Although there exists a large amount of studies on GDC dissolution in heterogeneous porous media [e.g. *Green and Ennis-King*, 2010; *Elenius and Gasda*, 2013; *Green and Ennis-King*, 2014; *Taheri et al.*, 2018; *Mahyapour et al.*, 2022], only a few researches offer concise formulas for predicting the dissolution rate. By conducting numerical simulations in homogeneous medium with embedded horizontal barriers, *Elenius and Gasda* [2013] proposed that the asymptotic dissolution rate can be estimated by

$$F_\infty = \gamma X_0^C \rho_0 \frac{\Delta\rho g \kappa_g}{\overline{\mu}} \left(\frac{\kappa_z^e}{\kappa_g}\right), \tag{2}$$

where κ_z^e is the equivalent vertical intrinsic permeability of the heterogeneous medium, and κ_g is the geometric mean of the permeability field. Essentially, these authors proposed to replace the intrinsic permeability by its equivalent quantity in heterogeneous media. Subsequent studies analyze whether and how the anisotropic effect of the permeability distribution affects the GDC, but the results are inconsistent [*Xu et al.*, 2006; *Green and Ennis-King*, 2010; *Cheng et al.*, 2012; *Chen et al.*, 2013; *Green and Ennis-King*, 2014; *Kim*, 2014; *Soltanian et al.*, 2017; *Elgahawy and Azaiez*, 2021]. Inspired by the result for the isotropic heterogeneous field, researchers propose that the dissolution rate in the anisotropic heterogeneous field can be expressed by

$$F_\infty = \gamma X_0^C \rho_0 \frac{\Delta\rho g \kappa_g}{\overline{\mu}} \left(\frac{\kappa_z^e}{\kappa_g}\right) \left(\frac{\kappa_x^e}{\kappa_z^e}\right)^\eta, \tag{3}$$

Table 1: Published data for the scaling coefficient γ in isotropic homogeneous field.

γ	**Top boundary**	**Method**	**Reference**
0.015-0.017	diff. only[a]	Num.	*Pruess and Zhang* [2008]
0.017	diff. only	Num.	*Hesse* [2008]
0.017-0.018	diff. only	Num.	*Pau et al.* [2010]
$0.12Ra^{-0.16}$[e]	-	Num.,Exp.	*Neufeld et al.* [2010]
$0.045Ra^{-0.24}$	Permeable	Exp.	*Backhaus et al.* [2011]
0.017	diff. only	Num..	*Cheng et al.* [2012]
0.02	diff. only	Num.	*Elenius and Johannsen* [2012]
0.02	diff. only	Num.	*Elenius et al.* [2012]
0.075	CTZ[b]	Num.	*Elenius et al.* [2012]
$0.037Ra^{-0.16}$	Permeable	Exp.	*Tsai et al.* [2013]
$0.0794Ra^{-0.168}$	diff. only	Theor.	*Farajzadeh et al.* [2013]
0.017	diff. only	Num.	*Slim* [2014]
0.025	(0.2κ[c])	Num.	*Slim* [2014]
0.044	(0.6κ[d])	Num.	*Slim* [2014]
0.065	CTZ	Num.	*Martinez and Hesse* [2016]
0.018-0.019	diff. only	Num.	*Martinez and Hesse* [2016]
$Ra^{-0.2154}$, 0.06	Permeable	Exp.	*Rasmusson et al.* [2017]
0.09	Permeable	Num.	This study

[a] The top boundary only allows mass to go through the boundary via diffusion.
[b] The top boundary is capillary transition zone.
[c] The permeability of the top boundary is 0.2 the permeability of the domain.
[d] The permeability of the top boundary is 0.6 the permeability of the domain.
[e] Ra is Rayleigh number (cf. [*Neufeld et al.*, 2010]).

where κ_x^e is the equivalent intrinsic permeability along the horizontal direction, and the exponent η describes the impact of anisotropy. The last term represents the anisotropic effect described by the horizontal to vertical equivalent permeability ratio. By conducting numerical simulations of GDC dissolution in homogeneous media with embedded horizontal barriers, which is similar to the aforementioned method used by *Elenius and Gasda* [2013], *Green and Ennis-King* [2014] found that $\eta = 0.5$, which indicates that dissolution increases with horizontal to vertical equivalent permeability ratio. Note that when $\eta = 0.5$, the dissolution rate is actually proportional to the geometric mean of the permeabilities $\sqrt{\kappa_x^e \kappa_z^e}$. In contrast, *Erfani et al.* [2022] give $\eta = 0.21$. However, the results from *Soltanian et al.* [2017] and *Elgahawy and Azaiez* [2021] show that the increasing κ_x^e at fixed κ_z^e can reduce the asymptotic dissolution rate, implying that η may be negative.

4 Computational Approach

4.1 Model Setup

We conduct numerical simulations of Gravity-Driven Convection (GDC) over two-dimensional vertical fields of various permeability heterogeneity, which varies in space as a function of the horizontal and vertical distances. We assume that the interface between the CO_2-rich phase and brine is horizontal under buoyancy force, and that the brine at the interface is always saturated with CO_2. We only study the portion below the interface and therefore all simulations are conducted with a single-phase model. Initially, the CO_2 concentration in brine is very low and the system is at static state. CO_2 enters into the domain through the top boundary that has fixed high CO_2 mass fraction. Brine is represented by a high-concentration Sodium Chloride (NaCl) solution. The objective is to get a quantitative relation between representative properties of the heterogeneous field and the CO_2 dissolution rate through the top boundary.

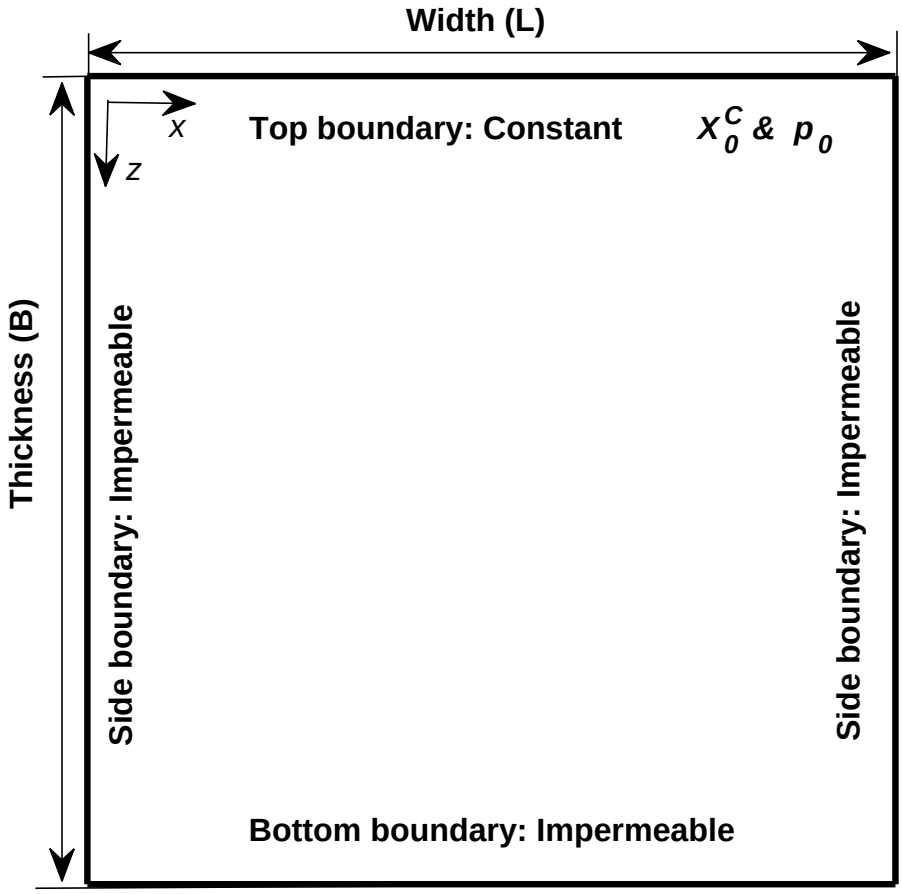

Figure 2: Sketch of setup design.

Figure 2 shows the two-dimensional vertical domain used to simulate the development of dissolution process enhanced by GDC. Detailed parameter settings are as follows. The top boundary, which represents the interface between brine and CO_2-rich phase, has constant liquid pressure $p_0 = 150$ [bar] and constant CO_2 mass fraction $X_0^C = 0.041$ [kg·kg^{-1}]. The bottom and lateral boundaries are no-flow boundaries. Initially, the brine has a very low background CO_2 mass fraction $X_{bg}^C \approx 0.0006$ [kg·kg^{-1}]. An initial brine pressure of p_0 =150 [bar] is imposed at the top layer and increases downwards at a gradient of ρg, which means that the brine is initially at hydrostatic state. The temperature (T_c) is fixed to 60 [°C], and the salinity of brine (m^S) is constant 0.5 [molal]. When the mass fraction of aqueous CO_2 increases from initial X_{bg}^C to X_0^C on the top boundary, the density of brine increases by $\Delta\rho = 8.2$ [kg·m^{-3}]. We note that the viscosity of the brine slightly changes from 1.0 [mpa·s] at the minimum background CO_2 mass fraction (X_{bg}^C) to 0.9 [mpa·s] at the maximum CO_2 mass fraction (X_0^C). Thus, the mean viscosity is approximated by $\overline{\mu}$ = 0.95 [mpa·s]. Table 2 summarizes the parameters that are used in the numerical simulations.

We note that the top boundary condition is different from most of those used in literature where the convection of the CO_2-saturated layer is either totally or partially suppressed (see Table 1). For instance, in *Pau et al.* [2010], the top constant concentration boundary only allows CO_2 to enter the domain via diffusion; this top boundary condition generates a much lower dis-

Table 2: Summary of the parameters adopted during numerical simulations.

Parameters	**Symbol**	**Units**	**Values**
Domain size	$L \times B$	[m ×m]	7.5×7.5
Grid discretization	$n_x \times n_z$	[-]	100×100
Porosity	ϕ	[-]	$0.15^{c,f}$
Geometric mean permeability	κ_g	[m^2]	10^{-12} ^{b,i}
Initial liquid pressure at top layer	p_0	[bar]	150 ^{h}
Initial background CO_2(aq) mass fraction	X^C_{bg}	[kg·kg^{-1}]	$\sim 0.0006^{g,j}$
CO_2(aq) mass fraction at top boundary	X^C_0	[kg·kg^{-1}]	0.041
Brine density at top boundary	ρ_0	[kg·m^{-3}]	1017
Brine density increase due to increased CO_2(aq) mass fraction	$\Delta\rho$	[kg·m^{-3}]	8.2
Salinity	m^S	[molal]	0.5 ^{e,i}
Mean viscosity	$\overline{\mu}$	[mpa·s]	0.95
Molecular diffusion coefficient	D	[m^2· s^{-1}]	2×10^{-9} ^{d,i}
Temperature	T_c	[°C]	$60^{a,k}$

Reference: [a] *Spycher et al.* [2003]; [b] *Chadwick et al.* [2004]; [c] *Maldal and Tappel* [2004]; [d] *Tewes and Boury* [2005]; [e] *Spycher and Pruess* [2005]; [f] *Mathieson et al.* [2009]; [g] *Xu et al.* [2007]; [h] *Iding and Ringrose* [2010]; [i] *Elenius and Johannsen* [2012]; [j] *Saaltink et al.* [2013]; [k] *Strandli and Benson* [2013].

solution rate. In some studies the top boundary is partially permeable and larger dissolution rates are obtained [*Hesse*, 2008; *Elenius et al.*, 2014; *Rasmusson et al.*, 2015]. Although it is more realistic to add a capillary transition zone beneath the top boundary [*Elenius et al.*, 2015], experimental results with totally permeable top boundaries [*Rasmusson et al.*, 2017] show only little discrepancy from the numerical results obtained in a model that includes the capillary transition zone [*Martinez and Hesse*, 2016]. Therefore, we employ the single phase flow model with permeable top boundary in this study, although our model is capable of two-phase flow simulations [*Wang et al.*, 2022].

An initial perturbation of the initial CO_2 mass fraction on the top boundary is added to stimulate the onset of instability at the beginning of simulation. We added a white noise that follows an uncorrelated Gaussian distribution [*Fu et al.*, 2013]. The magnitude of the noise is 1% of the initial mass fraction. *Hidalgo and Carrera* [2009] show that instability can be generated by the numerical error without introducing any external noise. Certainly, even though larger noise strength tends to accelerate the appearance of instability fingers, it is however unlikely to change the statistic behavior of the dissolution rate once the instability has fully developed [*Hidalgo and Carrera*, 2009; *Elenius and Johannsen*, 2012].

4.2 Governing Equations

On the basis of the mass balances of water and CO_2 species, the two governing transport equations are constructed as,

$$0 = \frac{\partial(\phi\rho X^H)}{\partial t} + \nabla\cdot(\rho X^H \boldsymbol{q}) - \nabla\cdot(\phi \boldsymbol{D}\rho\nabla X^H), \tag{4}$$

$$0 = \frac{\partial(\phi\rho X^C)}{\partial t} + \nabla\cdot(\rho X^C \boldsymbol{q}) - \nabla\cdot(\phi \boldsymbol{D}\rho\nabla X^C), \tag{5}$$

where ϕ [-] is the porosity of the saline formation, ρ [kg·m^{-3}] represents the density of brine, X [kg·kg^{-1}] is the mass fraction, superscripts (H, C) represent the water and aqueous CO_2 species, respectively, t [s] denotes the time, $\boldsymbol{D} = D\boldsymbol{I}_d$ [m^2·s^{-1}] denotes the dispersion tensor, which is assumed locally constant. Local dispersion has little impact on the asymptotic dissolution rates, which is the objective of this work [*Prasad and Simmons*, 2003; *Hidalgo and Carrera*, 2009]. The discharge rate ($\boldsymbol{q}$) is given by Darcy's law

$$\boldsymbol{q} = -\frac{\kappa}{\mu}(\nabla p - \rho g \nabla z), \tag{6}$$

where κ [m^2] is the intrinsic permeability, μ [pa· s] is the viscosity, p [pa] is the liquid pressure, and z [m] is the depth. Besides, we have the following constraints:

$$X^S = 0.05844 X^H m^S, \tag{7}$$

and

$$X^H + X^C + X^S = 1, \tag{8}$$

where m^S denotes the molality of salt. Here, we assume that the salt comprises only NaCl, and the molality of NaCl (m^S) is fixed. Define $\omega = (1 + 0.05844 m^S)$ and then Equations (7) and (8) merge to

$$\omega X^H + X^C = 1. \tag{9}$$

Under isotherm and isosalinity condition, ρ and μ are only governed by liquid pressure and aqueous CO_2 mass fraction (see Appendix A).

4.3 Dimensionless variables

In order to facilitate the analysis, results are presented using the following dimensionless variables, which are defined based on the works of *Ennis-King and Paterson* [2003] and *Rasmusson et al.* [2017],

$$X^{C*} = \frac{X^C}{X_0^C}, \qquad X^{H*} = \frac{X^H}{X_0^H}, \tag{10}$$

and

$$t^* = \frac{t}{t_c}, \qquad x^* = \frac{x}{L_c}, \qquad z^* = \frac{z}{L_c}, \tag{11}$$

where X_0^C and X_0^H are, respectively, the maximum CO_2 and water mass fractions, and t_c and L_c are the characteristic time and length scale of the gravity-driven convection problem defined as

$$t_c = \frac{(\overline{\mu}\phi)^2 D}{(\Delta\rho g \kappa_g)^2}, \qquad L_c = \frac{\overline{\mu}\phi D}{\Delta\rho g \kappa_g}. \tag{12}$$

The characteristic time t_c has been found to be closely related to the onset time of gravity-driven convection, and the characteristic length L_c closely related to the earliest finger width. In our simulations, we found that the earliest finger width, denoted as ℓ_c, can be approximated by $\ell_c \approx 70 L_c$. The governing equations are expressed in dimensionless form in the Appendix B.

Importantly, by expressing Darcy's law and the global dissolution rate in dimensionless form, we obtain that

$$q^* = \frac{q}{q_c}, \qquad q_c = \frac{\Delta\rho g \kappa_g}{\overline{\mu}}, \tag{13}$$

$$F^* = \frac{F}{F_c}, \qquad F_c = X_0^C \rho_0 \frac{\Delta\rho g \kappa_g}{\overline{\mu}}. \tag{14}$$

The characteristic velocity $v_c = q_c/\phi$ is closely related to the finger-tip velocity (see *Elenius and Johannsen* [2012]). We note that although the vertical length scale (i.e., domain thickness) and related dimensionless number (e.g., Rayleigh number) have been typically used to study gravity instability in the literature [*Rasmusson et al.*, 2017, and references therein], herein we do not use it because the vertical domain size has little impact on the asymptotic enhanced dissolution rate driven by instability fingers [*Elenius et al.*, 2015; *Tsinober et al.*, 2022]. This definition of the dimensionless length scale without using the domain thickness indicates that the instability is a random statistic behavior that does not change with the domain size provided that the domain is large enough to accommodate sufficient number of density fingers. In the supporting information, we have shown that increasing the vertical domain size employed in this work does not systematically affect the asymptotic dissolution rate [*Elenius and Johannsen*, 2012]. *Simmons et al.* [2001] give a detailed discussion of the limitation of using Rayleigh number based on the domain thickness.

4.4 Heterogeneity

The intrinsic permeability is the only aquifer property considered to vary in space. We represent the natural logarithm of the intrinsic permeability, denoted as $Y = \ln \kappa$, by a random space function to create multiple realizations of the aquifer permeability distribution. The random space function model is characterized by an exponential covariance function with mean ($\overline{Y}$), variance (σ_Y^2), horizontal correlation length (λ_h) and vertical correlation length (λ_v). The geometric mean of the intrinsic permeability is fixed to $\kappa_g = 10^{-12}$ m^2. Different degrees of heterogeneity and correlation anisotropy $\Omega = \lambda_h/\lambda_v$ are explored with σ_Y^2 ranging between highly homogeneous, σ_Y^2=0.1, to relatively highly heterogeneous, σ_Y^2=4, and Ω ranging between isotropic, Ω =1, and perfectly stratified, $\Omega = \infty$. The perfectly stratified random field is formed by separate horizontal layers of constant properties. The vertical correlation length is fixed to $\lambda_z = 2L_c$, and the horizontal correlation length is $\lambda_x = \Omega \cdot \lambda_z$. For comparison purposes, we also considered a homogeneous medium with $\kappa = \kappa_g$. In total, we conduct GDC simulations with 365 realizations. Random fields were generated using the sequential Gaussian simulation method implemented in the SGSIM code of GSLIB [*Journel and Huijbregts*, 1976; *Deutsch et al.*, 1992]. Table 3 summarizes the statistical properties of the random fields. An illustrative realization of each random field type is shown in Figure 4.

Table 3: Permeability heterogeneity adopted for the numerical simulations. The vertical correlation length is fixed to $\lambda_z = 2L_c$, and the horizontal correlation length is $\lambda_x = \Omega \cdot \lambda_z$.

Case	$\boldsymbol{\Omega}$	$\boldsymbol{\sigma_Y^2}$
Homogeneous	-	-
Isotropic	1	1
Isotropic	1	4
Anisotropic	2	0.1
Anisotropic	2	1
Anisotropic	4	0.1
Anisotropic	4	1
Anisotropic	4	4
Anisotropic	∞	1

4.5 Global Measures

Simulation results are analyzed based on two global measures of the dissolution behavior. The global dissolution rate (F [kg·m^{-2}·s^{-1}]) is defined as the rate at which CO_2 dissolves from the upper boundary at z=0. This can be expressed as [*Hidalgo and Carrera*, 2009]

$$F(t) = \frac{1}{L}\int_0^L \left[\rho X^C q_z - \phi D \rho \frac{\partial X^C}{\partial z}\right]_{z=0} dx. \tag{15}$$

Initially, the domain is stable, the convection flux is zero, and only molecular diffusion transports downwards the dissolved CO_2. The density-driven unstable convection does not emerge until the CO_2 mass fraction distribution reaches a critical point. After this, the dissolution rate rapidly increases to a quasi constant value until the domain is almost totally saturated with aqueous CO_2. In our simulations, the asymptotic value of the global dissolution rate F_∞ is estimated as the temporal average of $F(t)$ over the period of $[t_b/3, t_b]$, where t_b is the time when the earliest finger of aqueous CO_2 reaches the bottom (time when the maximum bottom CO_2 mass fraction exceeds 25% of X_0^C).

Another important global parameter that describes the vertical migration or the penetration depth of the CO_2 plume is the vertical finger-tip velocity [*Prasad and Simmons*, 2003]. The representative vertical finger-tip velocity of the CO_2 plume is estimated as,

$$v(t) = \max_{0<z<B}\left\{\frac{1}{L}\int_0^L \frac{1}{\phi} \mid q_z \mid dx\right\}. \tag{16}$$

Figure 3 illustrates the concept of vertical finger-tip velocity in our simulations. Similar to the global dissolution rate behavior, the vertical finger-tip velocity also reaches an asymptotic value [*Elenius and Johannsen*, 2012] in the constant-flux regime and remains at that value until the field is almost saturated. The asymptotic vertical finger-tip velocity v_∞ is also estimated by the temporal average of $v(t)$ over the time interval $[t_b/3, t_b]$.

In order to characterize the overall hydraulic behavior of the permeability field, we estimated the equivalent permeability along the horizontal κ_x^e and vertical κ_z^e direction for each realization of the random fields. For this, to estimate κ_i^e ($i = x, y$), we neglect gravity and saturate the porous medium with only water. We then set the domain sides perpendicular to the ith direction as impermeable, and we impose a pressure decrement $|\Delta_i p|$ along the ith direction. κ_i^e is estimated by the total volumetric flow Q_i passing through the system in the ith direction as $\kappa_i^e = \mu Q_i L_i/(A_i|\Delta_i p|)$, where L_i is the domain size along the ith direction and A_i the corresponding cross-sectional area [*Knudby and Carrera*, 2005; *Wang*, 2022].

4.6 Numerical Features

The model is implemented in a Matlab reservoir simulator toolbox designed for CO_2 storage [*Wang*, 2022]. The program is based on the finite volume method. The two governing equations (4) and (5) are solved simultaneously with an implicit Newton-Raphson method. Two-point flux approximation with up-winding scheme is used to calculate mass transport. Although the unconditional stable implicit method is employed, we should still control the time step in the numerical simulation to avoid significant numerical dispersion. In this work, the time step is limited by either advection ($\Delta t < \Delta l\phi/(\boldsymbol{q}\cdot\boldsymbol{n})$) or diffusion ($\Delta t < \sqrt{\Delta l/(2D\phi)}$), whichever is smaller. Here, Δl and $\boldsymbol{n}$ are respectively the distance between the centroids of two adjacent cells and the unitary perpendicular vector to their interface. Detailed implementation of this numerical solution and related source code can be found in our previous works [*Wang et al.*, 2022, 2023].

The numerical discretization consists in 100×100 squared cells of equal size. The cell size is chosen to strike a balance between capturing small instability fingers and managing computational expenses without compromising accuracy following *Lindeberg and Bergmo* [2003] and

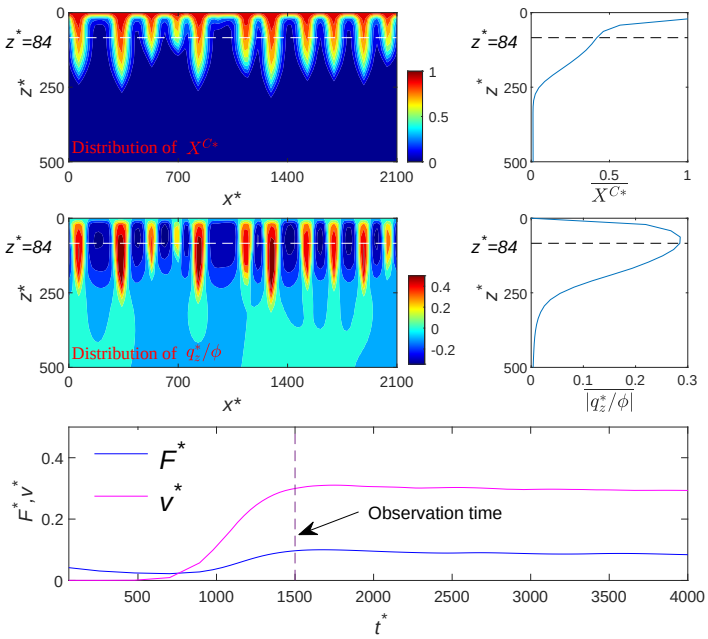

Figure 3: Maps of the dimensionless CO_2 mass fraction (X^{C*}) and its horizontal average ($\overline{X^{C*}}$), the dimensionless vertical flow velocity (q_z^*/ϕ) and the horizontal average of absolute dimensionless vertical flow velocity ($\overline{|q_z^*/\phi|}$), and temporal the development of dimensionless dissolution rate (F^*) and finger velocity (v^*) in an illustrative realization. The dimensionless finger velocity is represented by $v^* = \max \overline{|q_z^*/\phi|}$.

Elenius et al. [2015]. The grid size is smaller than the finger width, $\Delta = 0.3\ell_c = 21L_c$, and at the same time the shortest correlation length is described by at least 7 grid cells. We note that the finger width ℓ_c is close to the approximate value $4\pi^2 L_c$ needed for the generation of instability [*Lapwood*, 1948].

4.7 Effective Asymptotic Dissolution Models

Two effective dissolution models are proposed here based on previous results reported in literature (see Section 3) with the objective to offer a simplified representation of the overall asymptotic dissolution behavior in naturally occurring heterogeneous porous media. In the first effective model, we have extended the formula (3) to a more general expression that incorporates the effect of anisotropy. In dimensionless form, the model expresses that

$$F^*_\infty = \gamma_1 \left(\frac{\kappa^e_z}{\kappa_g}\right)^{\alpha_1} \left(\frac{\kappa^e_x}{\kappa^e_z}\right)^{\beta_1}. \tag{17}$$

Here, the dimensionless asymptotic dissolution rate is $F^*_\infty = F_\infty/F_c$. The last term on the right hand side of this expression represents the anisotropy of the permeability field, defined as $a_f = \kappa^e_x/\kappa^e_z$.

Existing effective asymptotic dissolution models rely exclusively on equivalent permeability values. Thus, it remains uncertain whether predictions of the dissolution rate can be made using field observations, such as the finger-tip velocity v_∞. For this, in the second model, we have considered the following relationship written in dimensionless form as

$$F^*_\infty = \gamma_2 \left(\frac{v_\infty}{v_c}\right)^{\alpha_2} \left(\frac{\kappa^e_x}{\kappa^e_z}\right)^{\beta_2}. \tag{18}$$

Essentially, this expression replaces the equivalent vertical permeability with the vertical finger velocity, which seems to offer a more direct description of the CO_2 plume migration. γ_1, γ_2, α_1, α_2, β_1 and β_2 are tuning coefficients of the two effective asymptotic dissolution models.

5 Results and Discussion

5.1 Impact of Heterogeneity

We first provide a general description of the impact of heterogeneity on the vertical migration of the CO_2 plume and dissolution rates. We focused on the influence of anisotropy in the correlation structure of permeability Ω and the degree of heterogeneity σ^2_Y. Figure 4 shows the temporal evolution of the spatial distribution of CO_2 mass fraction for different types of heterogeneity. For illustrative purposes, we chose a representative permeability realization for each case. These realizations are shown in the first panel of Figure 4. In all cases, results show that instability CO_2 fingers grow, merge and re-initiate as also observed in laboratory experiments [*Rasmusson et al.*, 2017; *Liyanage*, 2018; *Tsinober et al.*, 2022] and numerical simulations [*Elenius et al.*, 2015]. Importantly, from Figure 4, we can see that CO_2 fingering is strongly affected by heterogeneity. In particular, the presence of vertical well-connected high permeability zones (preferential channels) facilitates the initiation and growth of the instability fingers (see for instance the second column of Figure 4). Actually, the white randomness of the top CO_2 mass fraction (needed in homogeneous media to create instabilities) is redundant in heterogeneous porous media as instabilities are controlled by these vertical preferential channels. In accordance with *Simmons et al.* [2001], we also see that heterogeneity dissipates vertical finger growth through dispersive mixing. This effect increases with Ω, i.e., when horizontal well-connected high-permeability structures exist. This is strongly manifested in perfectly stratified media with σ^2_Y=1 and Ω=∞ (fourth column of Figure 4).

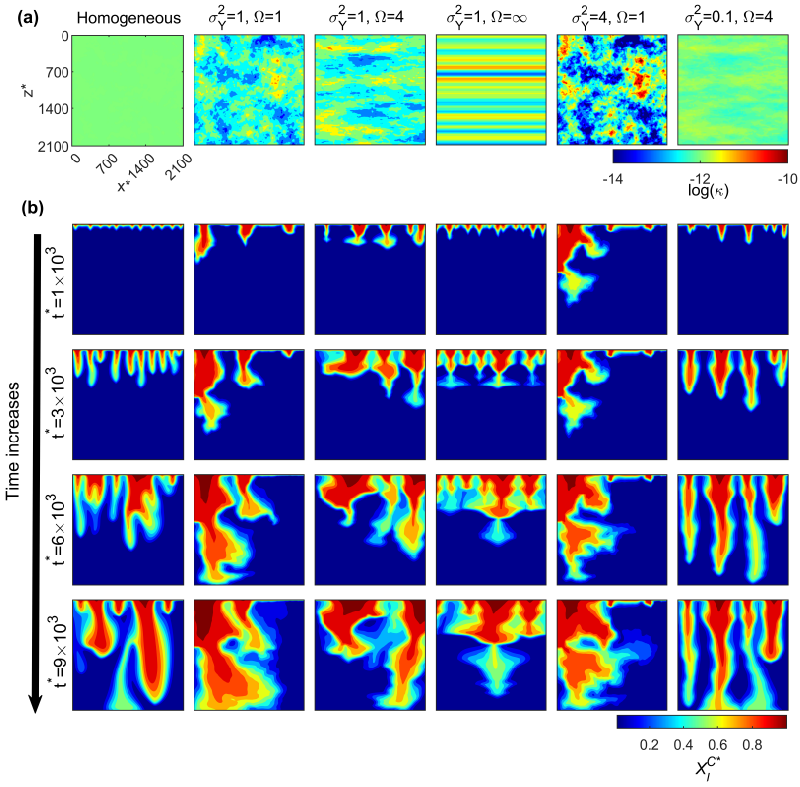

Figure 4: (a) Logarithm permeability ($\log(\kappa)$) distribution. (b) Development of dimensionless CO_2 mass fraction distribution ($X_l^{C^*}$) due to gravity-driven convection.

For completeness, we also show the temporal evolution of the dissolution rate as a function of σ_Y^2 and Ω in Figure 5. Results are presented in terms of the ensemble average and the coefficient of variation of $F^*(t^*)$. As expected, in homogeneous media, the dissolution process, shows the three well-known stages: an initial diffusion-controlled decrease, followed by an onset of nonlinear growth at $t^* = 500$ due to instability, and eventually stabilizing at an approximately constant dissolution rate. However, in heterogeneous media, results show in all cases that the early-time evolution of $F^*(t^*)$ in heterogeneous media is remarkably different than that in homogeneous media. The diffusive and the flux-growth regimes cannot be distinguished anymore and the system seems to be controlled by the interaction between gravity-driven convection and heterogeneity, indicating that heterogeneity helps triggering the onset of instability. This is consistent with results reported by *Schincariol et al.* [1997] and *Simmons et al.* [2001]. Of course, this also indicates that caution is needed when using the onset time of instability for homogeneous media [*Ennis-King and Paterson*, 2005; *Pruess and Zhang*, 2008] in real applications.

The influence of σ_Y^2 and Ω can also be seen from Figure 5. Interestingly, in statistically isotropic heterogeneous media, the degree of heterogeneity σ_Y^2 significantly influences the early behavior of $F^*(t^*)$, eventually converging to a similar asymptotic dissolution rate at large times. This suggests that the asymptotic dissolution rate might be governed by the existence of well-connected high-permeability zones, regardless of the specific high value of permeability. This effect is not seen in anisotropic heterogeneous media where we found that the higher the σ_Y^2 the lower is the

asymptotic dissolution rate. We attribute this to the fact that, when $\Omega > 1$, an increase in σ_Y^2 produces stronger well-connected permeability layers that inhibits gravity-driven convection. For the same reason, for equal σ_Y^2, the higher anisotropy Ω the less significant is the asymptotic dissolution rate. We also report in this figure a measure of the uncertainty in $F^*(t^*)$ given by the coefficient of variation (CV). We can observe that the coefficient of variation reaches a similar asymptotic value for all cases, regardless of the degree of heterogeneity. A similar trend is also observed for the vertical finger velocity, as shown in the second column of Figure 5, indicating a close relation between the dissolution rate and the vertical finger velocity.

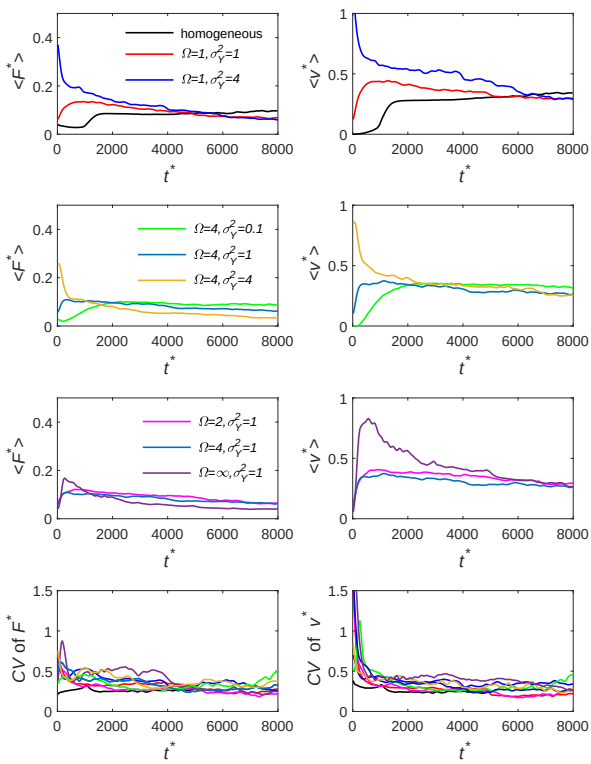

Figure 5: The temporal evolution of the ensemble average of the dimensionless dissolution rate ($\langle F^* \rangle$) through the top boundary and ensemble average of the dimensionless finger velocity ($\langle v^* \rangle$) for all the test cases listed in Table 3. Here, we also give the coefficient of variation (CV), which is the ratio of standard division to the ensemble average.

5.2 The Effective Asymptotic Dissolution Rate

The tuning coefficients of the two effective asymptotic dissolution models were independently adjusted by regression analysis of all simulation data obtained from the 365 realizations of the permeability distributions. These realizations involved random fields with different correlation structures of permeability and degrees of heterogeneity. To do this, we used Ordinary Least Squares (OLS) regression of the natural logarithm of the dissolution rate models (17) and (18). We respectively obtained a coefficient of determination R^2 of 0.71 and 0.84. The significance of all regression coefficients was below 0.05, meaning that both models can properly explain dissolution rates. Table 4 provides a summary of the regression analysis. Similar to the val-

ues reported in the literature, we find that $\alpha_1 = 1.1$, which is close to unity, meaning that the effective dissolution efficiency is almost linearly proportional to the equivalent vertical permeability. Moreover, we find that, in anisotropic heterogeneous media, the anisotropy of the equivalent permeability ($a_f = \kappa_x^e/\kappa_z^e$) can reduce the effectiveness of dissolution with a power law behavior given by $\beta_1 = -0.2$. This contradicts previous results obtained in homogeneous media with embedded horizontal impermeable inclusions [*Green and Ennis-King*, 2014; *Erfani et al.*, 2022], which indicated that $\beta_1 > 0$.

Table 4: Coefficients for effective asymptotic dissolution models obtained from OLS regression of all simulation data; the results from literature are also listed for comparison.

Predictors	**Coefficients**	**Values**	**MAE**	**RMSE**	**Source**
(17)	$(\gamma_1, \alpha_1, \beta_1)$	(0.08, 1.1,-0.2)	27%	22%	This work
(18)	$(\gamma_2, \alpha_2, \beta_2)$	(0.33, 1.0,-0.3)	20%	19%	This work
(17)	$(\gamma_1, \alpha_1, \beta_1)$	(0.09*, 1.0, 0)	40%	24%	*Elenius and Gasda* [2013]
(17)	$(\gamma_1, \alpha_1, \beta_1)$	(0.09*, 1.0, 0.5)	76%	44%	*Green and Ennis-King* [2014]

* Here, we update the value for the reference dissolution rate in the homogeneous case, because the original value was around 0.02 based on the impermeable top boundary (cf. Table 1).

Figure 6 compares the asymptotic dissolution rate predicted by the proposed asymptotic dissolution rate models, expressions (17) and (18), with corresponding simulated values. For completeness, we also show the performance of the reported expressions given by *Elenius and Gasda* [2013] and *Green and Ennis-King* [2014]. We visually differentiate between isotropic and anisotropic random fields. We can see that the predictor given by *Green and Ennis-King* [2014] significantly overestimates the dissolution rate in anisotropic random fields. Actually, the expression by *Green and Ennis-King* [2014] does not seem to improve the prediction given by *Elenius and Gasda* [2013]. The second effective dissolution model given by equation (18), proposed here based on the vertical finger-tip velocity, shows the best performance, indicating that the dissolution rate has a strong relationship with the finger-tip velocity. The Mean Absolute Error (MAE) for formulas (17) and (18) are 27% and 20%, respectively. These error are well accepted considering that even in homogeneous fields, the dissolution rate can fluctuate around 15% [*Pau et al.*, 2010].

In this work, we found a negative impact of the anisotropy of the permeability field a_f on dissolution rates. This can be physically explained in the following manner. Instabilities in the form of fingers exhibit nonuniform periodic high concentration distributions along the horizontal direction. When the spatial continuity of permeability values in the horizontal plane is substantial, any nonuniform concentration in this direction is rapidly eradicated by the enhancement of horizontal mixing induced by the introduction of companion horizontal flows. Consequently, the formation of finger-like instabilities becomes more challenging, especially in scenarios with high horizontal permeability values. In accordance, *Schincariol et al.* [1997] show that increasing the horizontal correlation length of the permeability distribution (increase in κ_x^e), can effectively inhibit instability growth and stabilize perturbations. Through numerical simulations in a wide variety of heterogeneous fields, *Simmons et al.* [2001], *Soltanian et al.* [2017] and *Elgahawy and Azaiez* [2021] also conclude that instability is dampened when κ_x^e/κ_z^e is relatively large. Recent studies by *Tsinober et al.* [2022] and *Hansen et al.* [2023] have also highlighted that the introduction of a minor horizontal background flow in geological carbon sequestration fields enhances horizontal mixing. This enhancement of mixing disrupts the growth of fingers, consequently leading to a reduction in the dissolution rate. All these works also suggest that horizontal flows have the potential to decrease nonuniform instabilities. To better illustrate this, Figure 7 shows simulated and estimated effective dissolution rates as a function aquifer properties $\{\kappa_z^e, \kappa_x^e/\kappa_z^e,$ and $v_\infty^*\}$. The figure shows a clear negative dependence of the asymptotic dissolution rates with permeability anisotropy.

We acknowledge that our numerical simulations have not covered cases with $a_f < 1$, which are uncommon in natural sediment formations. Studies conducted by *Simmons et al.* [2001] have demonstrated that vertically stratified structures with $a_f < 1$ can encourage vertical unstable convection by diminishing horizontal dissipation in instability fingers. Thus, it is observed that instability becomes more pronounced when a_f is small, aligning with the findings of our study.

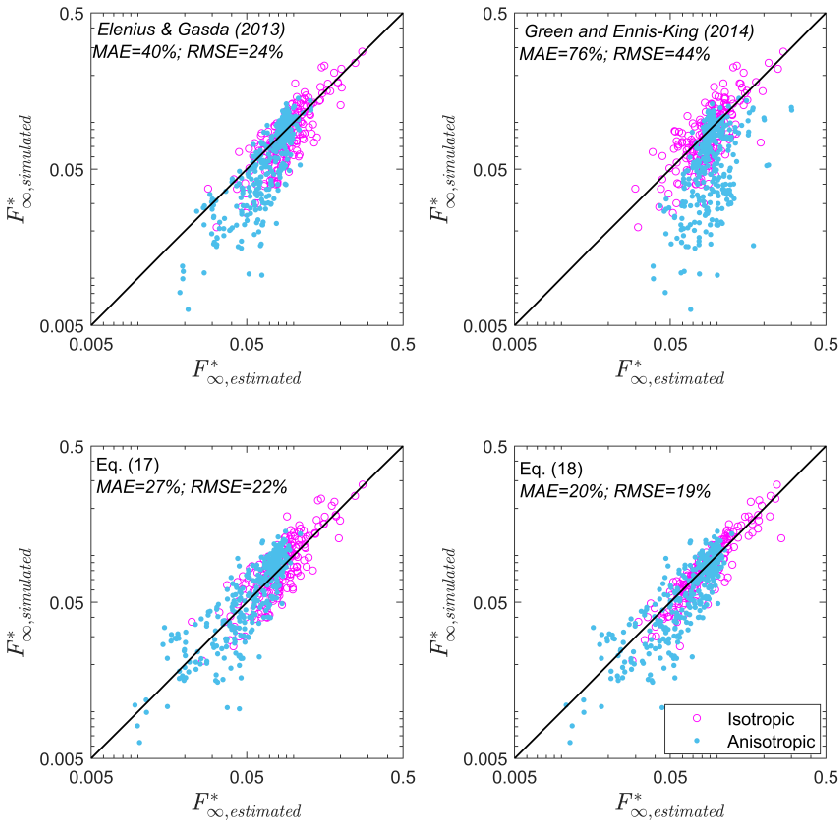

Figure 6: Comparison of the performances of the predictors given by *Elenius and Gasda* [2013], *Green and Ennis-King* [2014] and this work (cf. Table 4).

6 Conclusions

Geological Carbon Sequestration (GCS) in saline aquifers reduces the release of CO_2 into the atmosphere, thereby mitigating its impact on climate change. Once CO_2 is injected, the less dense CO_2-rich phase floats over the brine and gets trapped beneath an impermeable geological formation. At the interface between the brine phase and the CO_2-rich phase, CO_2 slowly dissolves into the brine, thereby reducing the risk of CO_2 leakage. Estimating CO_2 dissolution rates in this context is complex, as it requires characterizing the enhancement of dissolution due to Gravity-Driven Convection (GDC). GDC creates instability fingers that transfer the high CO_2 concentration brine downwards. While many studies offer a deep understanding of GDC in homogeneous porous media, less is known about dissolution rates in more realistic heterogeneous porous me-

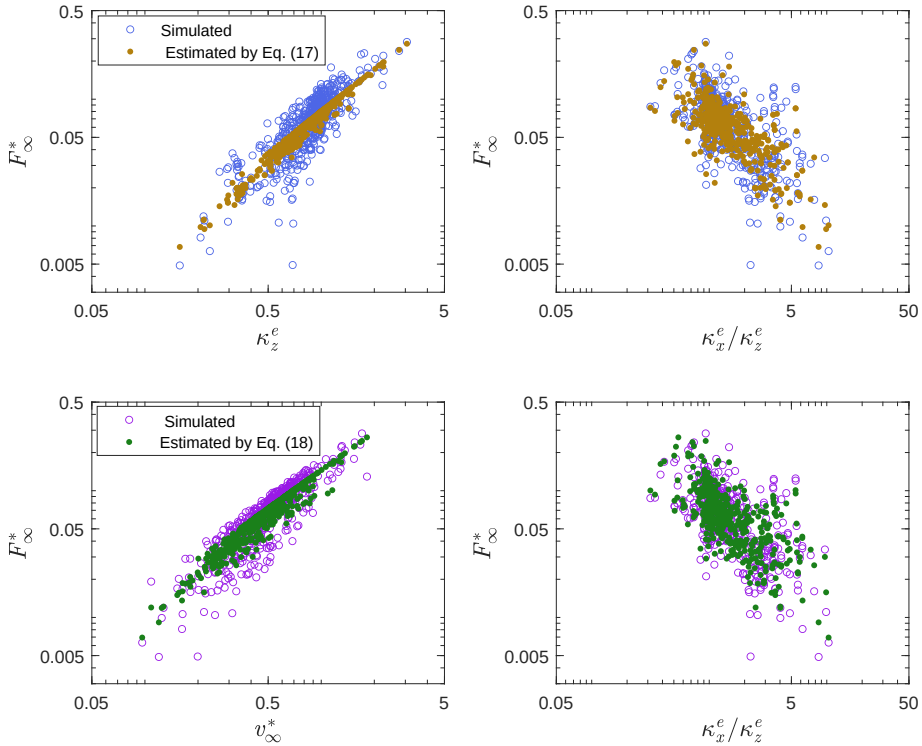

Figure 7: Simulated and estimated effective dissolution rates as a function aquifer properties.

dia. In this work, we have systematically analyzed the effect of heterogeneity on GDC-driven dissolution rates during GCS. To achieve this, we have conducted numerical simulations of GDC in multiple aquifer realizations of various permeability distributions. These distributions follow a random space function that exhibits distinct correlation structures (anisotropy) and degrees of heterogeneity. Based on these simulations, we have developed two effective asymptotic dissolution rate models derived from regression analysis of all the simulated data. The first model estimates the asymptotic dissolution rate using the aquifer's general hydraulic properties. For this model, we achieved a coefficient of determination (R^2) of 0.71, indicating a strong correlation between the variables compared to previous effective dissolution models [*Elenius and Gasda*, 2013; *Green and Ennis-King*, 2014],

$$F_\infty = 0.08 X_0^C \rho_0 \frac{\Delta\rho g \kappa_g}{\overline{\mu}} \left(\frac{\kappa_z^e}{\kappa_g}\right)^{1.1} \left(\frac{\kappa_x^e}{\kappa_z^e}\right)^{-0.2} . \tag{19}$$

This model requires some knowledge of the equivalent permeability value along the x and z directions $\{\kappa_x^e, \kappa_z^e\}$ and fluid properties. The equivalent permeability can be estimated by a wide variety of methods, including hydraulic tests (see *Renard and de Marsily* [1997]; *Sanchez-Vila et al.* [2006] for a review). Alternatively, direct observations of the CO_2 finger-tip velocity v can be used to estimate asymptotic dissolution rates. This velocity refers to the rate at which the fingers or plumes of dissolved CO_2 move downwards through the subsurface. Determining the finger-

tip velocity of CO_2 in the field involves the use of tracer tests, or geophysical or wellbore monitoring [*Würdemann et al.*, 2010; *Jenkins et al.*, 2015; *Michel-Meyer et al.*, 2020, and references therein]. Results have demonstrated that the finger-tip velocity offers a better estimate of dissolution rates with a coefficient of determination (R^2) of 0.84,

$$F_\infty^* = 0.33 X_0^C \rho_0 \frac{\Delta\rho g \kappa_g}{\overline{\mu}} \left(\frac{v_\infty}{v_c}\right)^{1.0} \left(\frac{\kappa_x^e}{\kappa_z^e}\right)^{-0.3}. \tag{20}$$

These effective asymptotic dissolution rate models express that the anisotropy of the permeability field (last term of the expressions) negatively affects dissolution rates. When permeability values have substantial spatial continuity horizontally, the corresponding increase in horizontal mixing inhibits nonuniform concentrations, making it harder for instabilities to form. These results differ from those presented by *Green and Ennis-King* [2014] in homogeneous media with horizontal barriers, where the dissolution rate is proposed to be enhanced by anisotropy with an exponent of 0.5. In accordance with our work, *Soltanian et al.* [2017] and *Elgahawy and Azaiez* [2021] demonstrated that increasing κ_x^e at fixed κ_z^e can reduce the asymptotic dissolution rate.

We have also explored the impact of heterogeneity on the temporal evolution of dissolution rates. We have shown that in heterogeneous porous media, vertical preferential channels, formed by well-connected high-permeability zones, play a significant role in initiating and developing instability fingers. Moreover, the presence of horizontal well-connected high-permeability structures inhibits the vertical growth of fingers by favoring dispersive mixing. Consequently, in anisotropic heterogeneous porous media, an increase in the degree of heterogeneity leads to a decrease in the asymptotic dissolution rate.

We note that the results from this study may have potential application to other common gravity-driven convection problems, such as contaminant migration, geothermal exploitation, saltwater intrusion and mineral precipitation/dissolution, where density differences may exist [*Zhang and Schwartz*, 1995; *Simmons et al.*, 1999; *Nield et al.*, 2008].

Acknowledgments

We acknowledge the help from Oriol Bertran-Oller and Rodrigo Perez in accessing the TITANI-high performance green computing cluster of the civil engineering school. Part of this work is done during Y. W.'s postdoc research at Dept. of Applied Mathematics, IFP Energies nouvelles, 1 et 4 Avenue du Bois-Préau, 92825 Rueil-Malmaison, France. Current correspondence of Y. W. is School of Earth and Space Sciences, Peking University, No.5 Yiheyuan Road Haidian District, 10087 Beijing, China. This work was partially supported by the European Commission, through project MARSOLUT (grant H2020-MSCA-ITN-2018); by the Spanish Ministry of Economy and Competitiveness, through project MONOPOLIOS (RTI 2018-101990-B-100, MINECO/ FEDER); and by the Catalan Agency for Management of University and Research Grants through FI 2017 (EMC/2199/2017).

A Density and Viscosity

In the numerical model, instead of using a simplified linear expression of the brine density based on the aqueous CO_2 concentration [e.g., *Elenius et al.*, 2015; *Martinez and Hesse*, 2016], we incorporated a more realistic brine density expression derived from [*Vilarrasa*, 2012], given the sensitivity of instability to the fluid property [*Jafari Raad et al.*, 2016; *Rasmusson et al.*, 2015, 2017]. In this model, the brine density, ρ [kg· m^{-3}], depends on brine phase pressure, temperature, molality of NaCl and CO_2 concentration. The expression for brine is given by *Garcia* [2003]

$$\rho = \rho_{lr} + cM^C - c\rho_{lr}V_\phi, \tag{A.1}$$

where c [mol·m^{-3}] is the number of moles of CO_2 per unit volume of brine phase; M^C [kg·mol^{-1}] is the molar mass of CO_2; and V_ϕ [m^3· mol^{-1}] is the apparent molar volume of CO_2 given by

$$V_\phi = 3.751 \times 10^{-5} - 9.585 \times 10^{-8} T_c + 8.74 \times 10^{-10} T_c^2 - 5.044 \times 10^{-13} T_c^3, \tag{A.2}$$

where T_c [°C] is temperature in Celsius; ρ_{lr} is the brine density when there is no CO_2 dissolution, calculated by *Phillips et al.* [1982]

$$\rho_{lr} = -3.033405 \times 10^3 + 1.0128163 \times 10^4 \iota - 8.750567 \times 10^3 \iota^2 + 2.66310 \times 10^3 \iota^3, \tag{A.3}$$

with

$$\begin{aligned} \iota = &- 9.9595 \exp\left(-4.539 \times 10^{-3} m^S\right) + 7.0845 \exp\left(-1.638 \times 10^{-4} T_c\right) \\ &+ 3.9093 \exp\left(2.551 \times 10^{-10} p\right), \end{aligned} \tag{A.4}$$

where m^S [molal] is the molality of NaCl and p [pa] is the pressure of brine. Equation (A.1) applies to $5 < T_c < 297$ [°C] and $p_{sv} < p < 300$ [bar]. Equation (A.3) applies to $10 < T_c < 350$ °C, $0.25 < m_l^S < 5$ [molal] and $p_{sv} < p < 500$ [bar] [*Phillips et al.*, 1982]. Here, p_{sv} is saturated vapor pressure. Rearranging Equation (A.1), we have [*Vilarrasa*, 2012]

$$\rho = \rho_{lr} \frac{1}{1 - X^C f_\delta} \approx \rho_{lr} (1 + X^C f_\delta), \tag{A.5}$$

with

$$f_\delta = 1 - \rho_{lr} \frac{V_\phi}{M^C}; \tag{A.6}$$

here X^C denotes the mass fraction of CO_2. The viscosity of brine is calculated following the works of *Garcia* [2003] and *Kumagai and Yokoyama* [1999]

$$\begin{aligned} \mu =& (3.85971 - 1.32561 \times 10^{-2} T_k) m^S + (-5.37539 + 1.90621 \times 10^{-2} T_k)(m^S)^{1/2} \\ &+ (8.79552 - 3.17229 \times 10^{-2} T_k) m^C + (-7.22796 + 2.64498 \times 10^{-2} T_k)(m^C)^2 \\ &+ 1.69956 \times 10^{-9} (p - 1 \times 10^5) + \mu_w (T_k, p = 10^5 [\text{Pa}]), \end{aligned} \tag{A.7}$$

where T_k [K] is temperature in Kelvin, m^C [molal] is the molality of CO_2, and μ_w [mPa· s] is the viscosity of pure water.

B Dimensionless Governing Equations

Given the dimensionless variables defined in section 4.2, the governing mass balance equations (4) and (5) can be written in dimensionless form as

$$\frac{\partial X^{C*}}{\partial t^*} = -\nabla^* \cdot \left(X^{C*} \boldsymbol{q}^* \right) + \nabla^* \cdot \left(\nabla^* X^{C*} \right), \tag{B.1}$$

$$\frac{\partial X^{H*}}{\partial t^*} = -\nabla^* \cdot \left(X^{H*} \boldsymbol{q}^* \right) + \nabla^* \cdot \left(\nabla^* X^{H*} \right), \tag{B.2}$$

where Darcy's law is expressed as

$$\boldsymbol{q}^* = -\exp(Y')\,(\nabla^* p^* - \rho^* \nabla^* z^*)\,, \tag{B.3}$$

and $\nabla^* = [\partial/\partial x^*, \partial/\partial z^*]$. Y' is the deviation of the natural log of the intrinsic permeability from the mean, i.e., $Y' = Y - \langle Y \rangle$. The geometric mean permeability is $\kappa_g = \exp(\langle Y \rangle)$. The fluid pressure and the density are normalized by

$$p^* = \frac{p\kappa_g}{\mu\phi D}, \text{ and } \rho^* = \frac{\rho}{\Delta\rho}. \tag{B.4}$$

Open Research

This work has no data-sharing issues, because all of the results are obtained by numerical solutions and have been provided in the figures and tables.

References

Agartan, E., L. Trevisan, A. Cihan, J. Birkholzer, Q. Zhou, and T. H. Illangasekare (2015), Experimental study on effects of geologic heterogeneity in enhancing dissolution trapping of supercritical CO2, *Water Resources Research*, doi:10.1002/2014WR015778.

Anbar, S., and S. Akin (2011), Development of a linear predictive model for carbon dioxide sequestration in deep saline carbonate aquifers, *Computers & geosciences*, *37*(11), 1802–1815.

Bachu, S., D. Bonijoly, J. Bradshaw, R. Burruss, S. Holloway, N. P. Christensen, and O. M. Mathiassen (2007), Co2 storage capacity estimation: Methodology and gaps, *International Journal of Greenhouse Gas Control*, *1*(4), 430 – 443, doi:https://doi.org/10.1016/S1750-5836(07)00086-2.

Backhaus, S., K. Turitsyn, and R. E. Ecke (2011), Convective instability and mass transport of diffusion layers in a Hele-Shaw geometry, *Physical Review Letters*, doi:10.1103/PhysRevLett.106.104501.

Baines, S. J., and R. H. Worden (2004), The long-term fate of co2 in the subsurface: natural analogues for co2 storage, *Geological Society, London, Special Publications*, *233*(1), 59–85.

Brainard, J. (2018), News at a glance, *Science*, *362*(6414), 504–506, doi:10.1126/science.362.6414.504.

Celia, M. A., S. Bachu, J. M. Nordbotten, and K. W. Bandilla (2015), Status of CO2 storage in deep saline aquifers with emphasis on modeling approaches and practical simulations, *Water Resources Research*, doi:10.1002/2015WR017609.

Chadwick, R., P. Zweigel, U. Gregersen, G. Kirby, S. Holloway, and P. Johannessen (2004), Geological reservoir characterization of a co2 storage site: The utsira sand, sleipner, northern north sea, *Energy*, *29*(9-10), 1371–1381.

Chen, C., L. Zeng, and L. Shi (2013), Continuum-scale convective mixing in geological CO2 sequestration in anisotropic and heterogeneous saline aquifers, *Advances in Water Resources*, doi:10.1016/j.advwatres.2012.10.012.

Cheng, P., M. Bestehorn, and A. Firoozabadi (2012), Effect of permeability anisotropy on buoyancy-driven flow for CO 2 sequestration in saline aquifers, *Water Resources Research*, doi:10.1029/2012WR011939.

De Paoli, M., F. Zonta, and A. Soldati (2017), Dissolution in anisotropic porous media: Modelling convection regimes from onset to shutdown, *Physics of Fluids*, *29*(2), 026,601.

Deutsch, C. V., A. G. Journel, et al. (1992), Geostatistical software library and user's guide, *New York*, *119*(147), 578.

Elenius, M., and S. E. Gasda (2021), Convective mixing driven by non-monotonic density, *Transport in Porous Media*, *138*(1), 133–155.

Elenius, M. T., and S. E. Gasda (2013), Convective mixing in formations with horizontal barriers, *Advances in Water Resources*, doi:10.1016/j.advwatres.2013.10.010.

Elenius, M. T., and K. Johannsen (2012), On the time scales of nonlinear instability in miscible displacement porous media flow, *Computational Geosciences*, doi: 10.1007/s10596-012-9294-2.

Elenius, M. T., J. M. Nordbotten, and H. Kalisch (2012), Effects of a capillary transition zone on the stability of a diffusive boundary layer, *IMA Journal of Applied Mathematics (Institute of Mathematics and Its Applications)*, doi:10.1093/imamat/hxs054.

Elenius, M. T., J. M. Nordbotten, and H. Kalisch (2014), Convective mixing influenced by the capillary transition zone, *Computational Geosciences*, doi:10.1007/s10596-014-9415-1.

Elenius, M. T., D. V. Voskov, and H. A. Tchelepi (2015), Interactions between gravity currents and convective dissolution, *Advances in Water Resources*, doi:10.1016/j.advwatres.2015.05.006.

Elgahawy, Y., and J. Azaiez (2021), Dynamics of buoyancy driven miscible iso-viscous flows in heterogeneous layered porous media, *Physics of Fluids*, *33*(7), 074,104.

Emami-Meybodi, H. (2017), Stability analysis of dissolution-driven convection in porous media, *Physics of Fluids*, *29*(1), 014,102.

Emami-Meybodi, H., and H. Hassanzadeh (2015), Two-phase convective mixing under a buoyant plume of co2 in deep saline aquifers, *Advances in Water Resources*, *76*, 55 – 71, doi:https://doi.org/10.1016/j.advwatres.2014.11.011.

Ennis-King, J., and L. Paterson (2003), Role of convective mixing in the long-term storage of carbon dioxide in deep saline formations, in *SPE Annual Technical Conference and Exhibition?*, pp. SPE–84,344, SPE.

Ennis-King, J., and L. Paterson (2005), Role of convective mixing in the long-term storage of carbon dioxide in deep saline formations, *SPE Journal*, doi:10.2118/84344-PA.

Erfani, H., M. Babaei, C. F. Berg, and V. Niasar (2022), Scaling co2 convection in confined aquifers: Effects of dispersion, permeability anisotropy and geochemistry, *Advances in Water Resources*, *164*, 104,191.

European Commission (2014), General union environment action programme to 2020. living well, within the limits of our planet, *1386/2013/EU. 2013, The 7th Environment Action Programme: European Union*, p. 30.

Farajzadeh, R., P. Ranganathan, P. L. Zitha, and J. Bruining (2011), The effect of heterogeneity on the character of density-driven natural convection of CO2 overlying a brine layer, *Advances in Water Resources*, doi:10.1016/j.advwatres.2010.12.012.

Farajzadeh, R., B. Meulenbroek, D. Daniel, A. Riaz, and J. Bruining (2013), An empirical theory for gravitationally unstable flow in porous media, *Computational Geosciences*, doi:10.1007/s10596-012-9336-9.

Frykman, P., and D. Wessel-Berg (2014), Dissolution trapping-convection enhancement limited by geology, *Energy Procedia*, *63*, 5467–5478.

Fu, X., L. Cueto-Felgueroso, and R. Juanes (2013), Pattern formation and coarsening dynamics in three-dimensional convective mixing in porous media, *Philosophical Transactions of the Royal Society A: Mathematical, Physical and Engineering Sciences*, *371*(2004), 20120,355.

Garcia, J. E. (2003), Fluid Dynamics of Carbon Dioxide Disposal into Saline Aquifers, *TH: Thesis (Ph.D.); Submitted to the University of California, Berkeley, CA (US); PBD: 18 Dec 2003*.

Gasda, S. E., J. M. Nordbotten, and M. A. Celia (2011), Vertically averaged approaches for CO2 migration with solubility trapping, doi:10.1029/2010WR009075.

Gasda, S. E., J. M. Nordbotten, and M. A. Celia (2012), Application of simplified models to CO 2 migration and immobilization in large-scale geological systems, *International Journal of Greenhouse Gas Control*, doi:10.1016/j.ijggc.2012.03.001.

Gilfillan, S. M., B. S. Lollar, G. Holland, D. Blagburn, S. Stevens, M. Schoell, M. Cassidy, Z. Ding, Z. Zhou, G. Lacrampe-Couloume, and C. J. Ballentine (2009), Solubility trapping in formation water as dominant CO2 sink in natural gas fields, *Nature*, doi: 10.1038/nature07852.

Green, C. P., and J. Ennis-King (2010), Effect of vertical heterogeneity on long-term migration of CO2 in saline formations, *Transport in Porous Media*, doi:10.1007/s11242-009-9498-7.

Green, C. P., and J. Ennis-King (2014), Steady dissolution rate due to convective mixing in anisotropic porous media, *Advances in Water Resources*, doi:10.1016/j.advwatres.2014.07.002.

Hansen, S. K., Y. Tao, and S. Karra (2023), Impacts of permeability heterogeneity and background flow on supercritical co2 dissolution in the deep subsurface, *Water Resources Research*, *59*(11), e2023WR035,394.

Hassanzadeh, H., M. Pooladi-Darvish, and D. W. Keith (2007), Scaling behavior of convective mixing, with application to geological storage of CO2, *AIChE Journal*, doi: 10.1002/aic.11157.

Hassanzadeh, H., M. Pooladi-Darvish, A. M. Elsharkawy, D. W. Keith, and Y. Leonenko (2008), Predicting PVT data for CO2-brine mixtures for black-oil simulation of CO2 geological storage, *International Journal of Greenhouse Gas Control*, doi: 10.1016/S1750-5836(07)00010-2.

Hesse, M. (2008), Mathematical modeling and multiscale simulation for co2 storage in saline aquifers, Ph.D. thesis, Stanford, CA: Department of Energy Resources Engineering, Stanford University.

Hidalgo, J. J., and J. Carrera (2009), Effect of dispersion on the onset of convection during co2 sequestration, *Journal of Fluid Mechanics*, *640*, 441–452.

Iding, M., and P. Ringrose (2010), Evaluating the impact of fractures on the performance of the in salah co2 storage site, *International Journal of Greenhouse Gas Control*, *4*(2), 242–248.

Jafari Raad, S. M., H. Emami-Meybodi, and H. Hassanzadeh (2016), On the choice of analogue fluids in co2 convective dissolution experiments, *Water Resources Research*, *52*(6), 4458–4468, doi:10.1002/2015WR018040.

Jenkins, C., A. Chadwick, and S. D. Hovorka (2015), The state of the art in monitoring and verification—ten years on, *International Journal of Greenhouse Gas Control*, *40*, 312–349.

Journel, A., and C. Huijbregts (1976), Mining geostatistics.

Kim, M., K. Y. Kim, W. S. Han, J. Oh, and E. Park (2019), Density-Driven Convection in a Fractured Porous Media: Implications for Geological CO2 Storage, *Water Resources Research*, doi:10.1029/2019WR024822.

Kim, M. C. (2014), Onset of buoyancy-driven convection in a liquid-saturated cylindrical anisotropic porous layer supported by a gas phase, *Transport in porous media*, *102*(1), 31–42.

Knudby, C., and J. Carrera (2005), On the relationship between indicators of geostatistical, flow and transport connectivity, *Advances in Water Resources*, *28*(4), 405 – 421, doi:https://doi.org/10.1016/j.advwatres.2004.09.001.

Kong, X. Z., and M. O. Saar (2013), Numerical study of the effects of permeability heterogeneity on density-driven convective mixing during CO2 dissolution storage, *International Journal of Greenhouse Gas Control*, doi:10.1016/j.ijggc.2013.08.020.

Kumagai, A., and C. Yokoyama (1999), Viscosities of aqueous NaCl solutions containing CO2 at high pressures, *Journal of Chemical and Engineering Data*, doi: 10.1021/je980178p.

Kumar, A., R. Ozah, M. Noh, G. A. Pope, S. Bryant, K. Sepehmoori, and L. W. Lake (2005), Reservoir simulation of CO2 storage in deep saline aquifers, *SPE Journal*, doi: 10.2118/89343-pa.

Lapwood, E. (1948), Convection of a fluid in a porous medium, in *Mathematical proceedings of the cambridge philosophical society*, vol. 44, pp. 508–521, Cambridge University Press.

Lin, C.-P., C.-F. Ni, I.-H. Lee, and W.-C. Li (2016), Effects of permeability variations on co 2 convection in anisotropic and heterogeneous saline formations., *Terrestrial, Atmospheric & Oceanic Sciences*, *27*(1).

Lindeberg, E., and P. Bergmo (2003), The Long-Term Fate of CO2 Injected into an Aquifer, in *Greenhouse Gas Control Technologies - 6th International Conference*, doi: 10.1016/b978-008044276-1/50078-7.

Lindeberg, E., and D. Wessel-Berg (1997), Vertical convection in an aquifer column under a gas cap of co2, *Energy Conversion and Management*, *38*, S229 – S234, doi: https://doi.org/10.1016/S0196-8904(96)00274-9, proceedings of the Third International Conference on Carbon Dioxide Removal.

Lindeberg, E., and D. Wessel-Berg (2011), Upscaling studies of diffusion induced convection in homogeneous and heterogeneous aquifers, *Energy Procedia*, *4*, 3927–3934.

Liyanage, R. (2018), Convective dissolution in porous media: three-dimensional imaging experiments and numerical simulations, Ph.D. thesis, Imperial College London.

Macminn, C. W., and R. Juanes (2013), Buoyant currents arrested by convective dissolution, *Geophysical Research Letters*, doi:10.1002/grl.50473.

Mahyapour, R., S. Mahmoodpour, M. Singh, and S. Omrani (2022), Effect of permeability heterogeneity on the dissolution process during carbon dioxide sequestration in saline aquifers: two-and three-dimensional structures, *Geomechanics and Geophysics for Geo-Energy and Geo-Resources*, *8*(2), 1–22.

Maldal, T., and I. Tappel (2004), Co2 underground storage for snøhvit gas field development, *Energy*, *29*(9-10), 1403–1411.

Martinez, M. J., and M. A. Hesse (2016), Two-phase convective co2 dissolution in saline aquifers, *Water Resources Research*, *52*(1), 585–599, doi:10.1002/2015WR017085.

Matacic, C. (2018), News at a glance, *Science*, *362*(6421), 1334–1336, doi:10.1126/science.362.6421.1334.

Mathieson, A., I. Wright, D. Roberts, and P. Ringrose (2009), Satellite imaging to monitor co2 movement at krechba, algeria, *Energy Procedia*, *1*(1), 2201–2209.

Michel-Meyer, I., U. Shavit, A. Tsinober, and R. Rosenzweig (2020), The role of water flow and dispersive fluxes in the dissolution of co2 in deep saline aquifers, *Water Resources Research*, *56*(11), e2020WR028,184.

Neufeld, J. A., M. A. Hesse, A. Riaz, M. A. Hallworth, H. A. Tchelepi, and H. E. Huppert (2010), Convective dissolution of carbon dioxide in saline aquifers, *Geophysical Research Letters*, *37*(22), doi:10.1029/2010GL044728.

Nicot, J.-P. (2008), Evaluation of large-scale co2 storage on fresh-water sections of aquifers: An example from the texas gulf coast basin, *International Journal of Greenhouse Gas Control*, *2*(4), 582–593.

Nield, D. A., C. T. Simmons, A. V. Kuznetsov, and J. D. Ward (2008), On the evolution of salt lakes: Episodic convection beneath an evaporating salt lake, *Water Resources Research*, doi:10.1029/2007WR006161.

Pau, G. S., J. B. Bell, K. Pruess, A. S. Almgren, M. J. Lijewski, and K. Zhang (2010), High-resolution simulation and characterization of density-driven flow in co2 storage in saline aquifers, *Advances in Water Resources*, *33*(4), 443 – 455, doi:https://doi.org/10.1016/j.advwatres.2010.01.009.

Phillips, S. L., A. Igbene, J. A. Fair, H. Ozbek, and M. Tavana (1982), Technical Databook for Geothermal energy utilization., in *Proceedings of the Symposium on Thermophysical Properties*.

Prasad, A., and C. T. Simmons (2003), Unstable density-driven flow in heterogeneous porous media: A stochastic study of the elder [1967b]"short heater" problem, *Water Resources Research*, *39*(1), SBH–4.

Pritchard, D. (2007), Gravity currents over fractured substrates in a porous medium, *Journal of Fluid Mechanics*, doi:10.1017/S0022112007006623.

Pruess, K. (2005), Numerical studies of fluid leakage from a geologic disposal reservoir for CO2 show self-limiting feedback between fluid flow and heat transfer, *Geophysical Research Letters*, doi:10.1029/2005GL023250.

Pruess, K., and J. Nordbotten (2011), Numerical Simulation Studies of the Long-term Evolution of a CO2 Plume in a Saline Aquifer with a Sloping Caprock, *Transport in Porous Media*, doi:10.1007/s11242-011-9729-6.

Pruess, K., and K. Zhang (2008), Numerical Modeling Studies of The Dissolution-Diffusion-Convection Process During CO2 Storage in Saline Aquifers, *Lawrence Berkeley National Laboratory*.

Ranganathan, P., R. Farajzadeh, H. Bruining, and P. L. Zitha (2012), Numerical Simulation of Natural Convection in Heterogeneous Porous media for CO 2 Geological Storage, *Transport in Porous Media*, doi:10.1007/s11242-012-0031-z.

Rasmusson, M., F. Fagerlund, Y. Tsang, K. Rasmusson, and A. Niemi (2015), Prerequisites for density-driven instabilities and convective mixing under broad geological CO2 storage conditions, *Advances in Water Resources*, doi:10.1016/j.advwatres.2015.08.009.

Rasmusson, M., F. Fagerlund, K. Rasmusson, Y. Tsang, and A. Niemi (2017), Refractive-Light-Transmission Technique Applied to Density-Driven Convective Mixing in Porous Media With Implications for Geological CO2 Storage, *Water Resources Research*, doi: 10.1002/2017WR020730.

Renard, P., and G. de Marsily (1997), Calculating equivalent permeability: a review, *Advances in Water Resources*, *20*(5), 253–278, doi:https://doi.org/10.1016/S0309-1708(96)00050-4.

Riaz, A., M. HESSE, H. A. TCHELEPI, and F. M. ORR (2006), Onset of convection in a gravitationally unstable diffusive boundary layer in porous media, *Journal of Fluid Mechanics*, *548*, 87–111, doi:10.1017/S0022112005007494.

Saaltink, M. W., V. Vilarrasa, F. De Gaspari, O. Silva, J. Carrera, and T. S. Rötting (2013), A method for incorporating equilibrium chemical reactions into multiphase flow models for co2 storage, *Advances in Water Resources*, *62*, 431 – 441, doi: https://doi.org/10.1016/j.advwatres.2013.09.013, computational Methods in Geologic CO2 Sequestration.

Salibindla, A. K. R., R. Subedi, V. C. Shen, A. U. M. Masuk, and R. Ni (2018), Dissolution-driven convection in a heterogeneous porous medium, *Journal of Fluid Mechanics*, *857*, 61–79, doi:10.1017/jfm.2018.732.

Sanchez-Vila, X., A. Guadagnini, and J. Carrera (2006), Representative hydraulic conductivities in saturated groundwater flow, *Reviews of Geophysics*, *44*(3), doi: https://doi.org/10.1029/2005RG000169.

Sathaye, K. J., M. A. Hesse, M. Cassidy, and D. F. Stockli (2014), Constraints on the magnitude and rate of co2 dissolution at bravo dome natural gas field, *Proceedings of the National Academy of Sciences*, *111*(43), 15,332–15,337.

Schincariol, R. A., F. W. Schwartz, and C. A. Mendoza (1997), Instabilities in variable density flows: Stability and sensitivity analyses for homogeneous and heterogeneous media, *Water resources research*, *33*(1), 31–41.

Simmons, C. T., K. A. Narayan, and R. A. Wooding (1999), On a test case for density-dependent groundwater flow and solute transport models: The salt lake problem, *Water Resources Research*, doi:10.1029/1999WR900254.

Simmons, C. T., T. R. Fenstemaker, and J. M. Sharp Jr (2001), Variable-density groundwater flow and solute transport in heterogeneous porous media: approaches, resolutions and future challenges, *Journal of contaminant hydrology*, *52*(1-4), 245–275.

Slim, A. C. (2014), Solutal-convection regimes in a two-dimensional porous medium, *Journal of Fluid Mechanics*, *741*, 461–491, doi:10.1017/jfm.2013.673.

Soltanian, M. R., M. A. Amooie, N. Gershenzon, Z. Dai, R. Ritzi, F. Xiong, D. Cole, and J. Moortgat (2017), Dissolution Trapping of Carbon Dioxide in Heterogeneous Aquifers, *Environmental Science and Technology*, doi:10.1021/acs.est.7b01540.

Spycher, N., and K. Pruess (2005), CO2-H2O mixtures in the geological sequestration of CO2. II. Partitioning in chloride brines at 12-100°C and up to 600 bar, *Geochimica et Cosmochimica Acta*, doi:10.1016/j.gca.2005.01.015.

Spycher, N., K. Pruess, and J. Ennis-King (2003), CO2-H2O mixtures in the geological sequestration of CO2. I. Assessment and calculation of mutual solubilities from 12 to 100°C and up to 600 bar, *Geochimica et Cosmochimica Acta*, doi: 10.1016/S0016-7037(03)00273-4.

Strandli, C. W., and S. M. Benson (2013), Identifying diagnostics for reservoir structure and CO2 plume migration from multilevel pressure measurements, *Water Resources Research*, doi:10.1002/wrcr.20285.

Taheri, A., D. Wessel-Berg, O. Torsaeter, and M. Soroush (2012), The effects of anisotropy and heterogeneity on CO2 dissolution in deep saline aquifers, in *Society of Petroleum Engineers - Carbon Management Technology Conference 2012*, doi:10.7122/151345-ms.

Taheri, A., O. Torsæter, E. Lindeberg, N. J. Hadia, and D. Wessel-Berg (2018), Qualitative and quantitative experimental study of convective mixing process during storage of co2 in heterogeneous saline aquifers, *International Journal of Greenhouse Gas Control*, *71*, 212–226.

Tewes, F., and F. Boury (2005), Formation and rheological properties of the supercritical co2- water pure interface, *The Journal of Physical Chemistry B*, *109*(9), 3990–3997.

Tsai, P. A., K. Riesing, and H. A. Stone (2013), Density-driven convection enhanced by an inclined boundary: Implications for geological CO2 storage, *Physical Review E - Statistical, Nonlinear, and Soft Matter Physics*, doi:10.1103/PhysRevE.87.011003.

Tsinober, A., R. Rosenzweig, H. Class, R. Helmig, and U. Shavit (2022), The role of mixed convection and hydrodynamic dispersion during co2 dissolution in saline aquifers: A numerical study, *Water Resources Research*, *58*(3), e2021WR030,494.

Tutolo, B. M., A. J. Luhmann, X.-Z. Kong, M. O. Saar, and W. E. Seyfried Jr (2014), Experimental observation of permeability changes in dolomite at co2 sequestration conditions, *Environmental science & technology*, *48*(4), 2445–2452.

Tutolo, B. M., A. J. Luhmann, X.-Z. Kong, M. O. Saar, and W. E. Seyfried Jr (2015a), Co2 sequestration in feldspar-rich sandstone: coupled evolution of fluid chemistry, mineral reaction rates, and hydrogeochemical properties, *Geochimica et Cosmochimica Acta*, *160*, 132–154.

Tutolo, B. M., X.-Z. Kong, W. E. Seyfried Jr, and M. O. Saar (2015b), High performance reactive transport simulations examining the effects of thermal, hydraulic, and chemical (thc) gradients on fluid injectivity at carbonate ccus reservoir scales, *International Journal of Greenhouse Gas Control*, *39*, 285–301.

Vella, D., and H. E. Hupper (2006), Gravity currents in a porous medium at an inclined plane, *Journal of Fluid Mechanics*, doi:10.1017/S0022112006009578.

Vilarrasa, V. (2012), Thermo-hydro-mechanical impacts of carbon dioxide (co2) injection in deep saline aquifers, Ph.D. thesis, Technical University of Catalonia.

Vilarrasa, V., and J. Carrera (2015), Geologic carbon storage is unlikely to trigger large earthquakes and reactivate faults through which co2 could leak, *Proceedings of the National Academy of Sciences*, *112*(19), 5938–5943.

Vilarrasa, V., D. Bolster, S. Olivella, and J. Carrera (2010), Coupled hydromechanical modeling of co2 sequestration in deep saline aquifers, *International Journal of Greenhouse Gas Control*, *4*(6), 910 – 919, doi:https://doi.org/10.1016/j.ijggc.2010.06.006, cO2 Storage at the EGU General Assembly 2009.

Vilarrasa, V., O. Silva, J. Carrera, and S. Olivella (2013), Liquid co2 injection for geological storage in deep saline aquifers, *International Journal of Greenhouse Gas Control*, *14*, 84–96.

Vilarrasa, V., S. Olivella, J. Carrera, and J. Rutqvist (2014), Long term impacts of cold co2 injection on the caprock integrity, *International Journal of Greenhouse Gas Control*, *24*, 1–13.

Wang, S., C. Zucheng, Y. Zhang, L. Jiang, Y. Liu, and S. Yongchen (2021), Unstable Density-Driven Convection of CO 2 in Homogeneous and Heterogeneous Porous Media with Implications for Deep Saline Aquifers , *Water Resources Research*, doi: 10.1029/2020wr028132.

Wang, Y. (2022), Numerical Modeling of Geological Carbon Sequestration: Enhanced Dissolution in Randomly Heterogeneous Media, doi:10.5281/zenodo.6769788.

Wang, Y., D. Fernàndez-Garcia, and M. W. Saaltink (2022), Carbon dioxide (co2) dissolution efficiency during geological carbon sequestration (gcs) in randomly stratified formations, *Water Resources Research*, *58*(8), e2022WR032,325.

Wang, Y., D. Fernàndez-Garcia, and M. W. Saaltink (2023), Modeling reactive multi-component multi-phase flow for geological carbon sequestration (gcs) with matlab, *Computers & Geosciences*, p. 105300.

Weir, G. J., S. P. White, and W. M. Kissling (1996), Reservoir storage and containment of greenhouse gases, *Transport in Porous Media*, doi:10.1007/BF00145265.

Würdemann, H., F. Möller, M. Kühn, W. Heidug, N. P. Christensen, G. Borm, F. R. Schilling, C. Group, et al. (2010), Co2sink—from site characterisation and risk assessment to monitoring and verification: One year of operational experience with the field laboratory for co2 storage at ketzin, germany, *International Journal of Greenhouse Gas Control*, *4*(6), 938–951.

Xiao, T., B. McPherson, R. Esser, W. Jia, N. Moodie, S. Chu, and S.-Y. Lee (2019), Forecasting commercial-scale co2 storage capacity in deep saline reservoirs: Case study of buzzard's bench, central utah, *Computers & Geosciences*, *126*, 41–51.

Xu, T., J. A. Apps, K. Pruess, and H. Yamamoto (2007), Numerical modeling of injection and mineral trapping of co2 with h2s and so2 in a sandstone formation, *Chemical Geology*, *242*(3-4), 319–346.

Xu, X., S. Chen, and D. Zhang (2006), Convective stability analysis of the long-term storage of carbon dioxide in deep saline aquifers, *Advances in Water Resources*, doi: 10.1007/s11432-006-0397-z.

Yan, M., C. Lu, J. Yang, Y. Xie, and J. Luo (2019), Impact of low-or high-permeability inclusion on free convection in a porous medium, *Geofluids*, *2019*.

Zhang, H., and F. W. Schwartz (1995), Multispecies Contaminant Plumes in Variable Density Flow Systems, *Water Resources Research*, doi:10.1029/94WR02567.

Numerical Analysis of the Effect of Heterogeneity on CO_2 Dissolution Enhanced by Gravity Driven Convection

Yufei Wang[1,2] **Daniel Fernàndez-Garcia**[1,2] **Maarten W. Saaltink**[1,2]

[1]Dept. of Civil and Environmental Engineering. Universitat Politècnica de Catalunya, Jordi Girona 1-3, 08034 Barcelona, Spain
[2]Associated Unit: Hydrogeology Group (UPC-CSIC)

Key Points:

- Gravity-Driven Convection (GDC) enhances the dissolution of overlying supercritical CO_2 into brine in heterogeneous media;
- GDC-driven dissolution is almost linearly proportional to the equivalent vertical intrinsic permeability and the vertical finger velocity;
- The horizontal to equivalent vertical permeability ratio can hinder the GDC-driven dissolution.

Corresponding author: Yufei Wang, `yufei.wang@pku.edu.cn`

Abstract

Dissolution trapping of CO_2 in brine can reduce the risk of leakage of supercritical CO_2 during long-term Geological Carbon Sequestration (GCS). The dissolution of overlying gaseous CO_2 into brine increases the density of brine in its upper portion, which causes gravity-driven convection (GDC) and thus significantly increases the rate of CO_2 dissolution. To date, most studies on GDC-driven dissolution are based on homogeneous media and only few studies exist on the effect of heterogeneity on GDC-driven dissolution. Here, we study the effect of heterogeneity on GDC-driven dissolution rate by using numerical simulations with randomly obtained permeability fields. Dissolution rates calculated by these simulations are related to properties of the permeability field by using least-squares regression. We obtained two empirical formulas for predicting the asymptotic GDC-driven dissolution rate. In the first formula the dissolution rate is almost linearly proportional to the dimensionless equivalent vertical permeability. In the second one the dissolution rate is linearly proportional to a dimensionless vertical finger-tip velocity. Both formulas show a non-linear relation between dissolution and anisotropy with higher anisotropy giving lower dissolution rates.

1 Introduction

Geological Carbon Sequestration (GCS) has proved to be a feasible and necessary approach to mitigate CO_2 emissions [*Vilarrasa et al.*, 2013, 2014; *European Commission*, 2014; *Vilarrasa and Carrera*, 2015; *Tutolo et al.*, 2014, 2015a,b; *Celia et al.*, 2015]. GCS consists of sequestering CO_2, separated from other gases at large point sources (e.g., thermal power plants), into geological brine formations [*Vilarrasa et al.*, 2010; *Brainard*, 2018; *Matacic*, 2018]. The injected CO_2, usually in supercritical state under reservoir condition, is expected to flow over the denser brine during the process of injection, and continuously move upwards and accumulate beneath a low permeability caprock after injection. Because the less dense CO_2 is immiscible but can dissolve in the resident brine, the injected CO_2 is sequestered by four mechanisms: (1) by being sealed under the low permeability caprock (hydrodynamic trapping), (2) by being trapped by capillarity (residual trapping), (3) by dissolving into the brine at the CO_2-brine interface (dissolution trapping) and (4) by reacting with rock formation (mineral trapping) [*Kumar et al.*, 2005; *Riaz et al.*, 2006; *Bachu et al.*, 2007; *Gasda et al.*, 2011, 2012; *Macminn and Juanes*, 2013; *Soltanian et al.*, 2017]. Hydrodynamic trapping is the fastest mechanism but is unstable, because the relatively light CO_2 can escape from the reservoir in case of seismic activity, faults or failing wellbore casings [*Vilarrasa*, 2012]. Mineral trapping is most stable but slow and usually negligible [*Baines and Worden*, 2004; *Saaltink et al.*, 2013; *Sathaye et al.*, 2014]. During the later stage of injection, the safety of the GCS is governed by the dissolution trapping, which is not affected by the non-integrity (e.g., faults) of the formation [*Strandli and Benson*, 2013; *Nicot*, 2008]. Therefore, the dissolution of CO_2 into brine is an important indicator to evaluate the safety of long-term CO_2 sequestration [*Anbar and Akin*, 2011; *Xiao et al.*, 2019].

The dissolution process is enhanced by Gravity-Driven Convection (GDC) [*Lindeberg and Wessel-Berg*, 1997; *Lindeberg and Bergmo*, 2003; *Lindeberg and Wessel-Berg*, 2011; *Tsai et al.*, 2013; *Sathaye et al.*, 2014]. Dissolution of the overlying CO_2 into the brine increases the brine density in the upper portion of the saline formation creating an unstable situation with more dense on top of less dense brine. This causes nonuniform GDC in the brine phase and enhances the downward movement of CO_2-saturated brine [*Weir et al.*, 1996; *Vella and Hupper*, 2006; *Pritchard*, 2007; *Pruess and Zhang*, 2008]. Moreover, the nonuniform downward flux of CO_2-saturated brine is accompanied by an upward flux of CO_2-unsaturated brine, increasing the contact between CO_2-rich phase and unsaturated brine, which further accelerates CO_2 dissolution [*Pruess*, 2005; *Gilfillan et al.*, 2009; *Elenius and Gasda*, 2021]. In contrast to pure molecular diffusion, which quickly fades away as the concentration profile reaches a Gaussian distribution, the GDC can fuel the vertical mass exchange at a high constant rate for a certain long time until the whole domain is close to full CO_2 saturation [*Pau et al.*, 2010; *Slim*, 2014]. Because the dissolution rate enhanced by

GDC can significantly reduce the amount of supercritical CO_2, thus reducing the possibility of leakage, a good understanding of this dissolution is essential [*Elenius et al.*, 2015].

Currently, a large quantity of studies exists on GDC-driven dissolution, ranging from theoretical analysis [e.g., *Elenius et al.*, 2012; *Emami-Meybodi*, 2017], laboratory experiments [e.g., *Neufeld et al.*, 2010; *Rasmusson et al.*, 2017; *Salibindla et al.*, 2018], numerical simulations [e.g., *Chen et al.*, 2013; *Elenius et al.*, 2015] to field observations [e.g., *Sathaye et al.*, 2014]. It is found that GDC depends to a large extent on properties of the formation (e.g., the permeability and porosity) and of the brine phase (e.g., the relation between brine density and concentration of dissolved CO_2, viscosity and molecular diffusion coefficient) [*Hassanzadeh et al.*, 2007, 2008; *Neufeld et al.*, 2010; *Elenius and Johannsen*, 2012; *Emami-Meybodi and Hassanzadeh*, 2015]. For instance, researchers find a linear relation between the dissolution rate and the intrinsic permeability for isotropic homogeneous media [*Rasmusson et al.*, 2015]. However, most of the current researches and conclusions are limited to (isotropic or anisotropic) homogeneous fields [e.g. *Ennis-King and Paterson*, 2005; *Pruess and Nordbotten*, 2011; *Cheng et al.*, 2012; *De Paoli et al.*, 2017; *Ranganathan et al.*, 2012; *Taheri et al.*, 2012].

Studies on heterogeneous fields are usually limited to qualitative analysis of the effect of heterogeneity [*Agartan et al.*, 2015; *Lin et al.*, 2016; *Soltanian et al.*, 2017; *Kim et al.*, 2019; *Yan et al.*, 2019; *Wang et al.*, 2021; *Elgahawy and Azaiez*, 2021]. Heterogeneity in permeability plays an important role in onset, growth, maintenance and decay of the GDC and the dissolution rate [*Schincariol et al.*, 1997; *Simmons et al.*, 2001]. *Frykman and Wessel-Berg* [2014] show that we may overestimate the effects of instability in a real heterogeneous field simply by conducting numerical simulations using a homogeneous field of equivalent permeability. *Prasad and Simmons* [2003] find that while it can trigger early instability, heterogeneity can reduce the instability by dissipating the density fingers through disordered high permeability pathways at a later stage.

Although several researches attempt to quantitatively analyze the relation between GDC and field properties for heterogeneous media, only a few offer explicit formulas between the GDC-driven dissolution rates and permeability heterogeneity. For instance, *Farajzadeh et al.* [2011] and *Kong and Saar* [2013] conducted numerical simulations of GDC in isotropic heterogeneous media, but did not offer a quantitative formula between CO_2 dissolution rates and heterogeneity measures. Therefore, conclusions from these researches cannot be directly applied to estimate the dissolution rate in real reservoirs. Several researches offer quantitative formulas for predicting dissolution rates but only consider simplified binary heterogeneous media [*Elenius and Gasda*, 2013; *Green and Ennis-King*, 2014] or homogeneous media with anisotropic permeability [*Erfani et al.*, 2022]. In these researches, different conclusions are given regarding the effect of permeability anisotropy on the dissolution rate.

Overall, we have a solid understanding of the GDC-driven dissolution process in isotropic homogeneous media, but the GDC-driven dissolution in heterogeneous media needs further study. Especially, we need to quantitatively clarify the impact of the anisotropy ratio on the effective dissolution rate. Moreover, the current predictors are all based on the (equivalent) permeability, and it remains unclear whether we can predict the dissolution rate based on other formation properties or field observations, such as the finger-tip velocity.

Therefore the objective of this work is to quantitatively analyze the effect of permeability heterogeneity on the GDC-driven dissolution rate in a wide range of (isotropic and anisotropic) heterogeneous fields with varying degrees of heterogeneity. We do this in two steps. The first step consists of performing numerical simulations over a large number of heterogeneous fields of different permeability distributions. Numerical simulations are carried out by a finite-difference numerical program developed by *Wang* [2022]. Permeability fields are generated with the sequential Gaussian simulation method implemented in the SGSIM code [*Journel and Huijbregts*, 1976]. In the second step the results of the simulations are analyzed to find relations between the GDC-driven dissolution rate and heterogeneity of permeability, and we compare our results against those given in literature. In this step, ordinary-least-squares linear regressions are used.

The rest of this paper is organized as follows. Section 2 gives a concise description of GDC. In section 3, we review existing formulas for GDC driven dissolution rates. Section 4 describes the computational approach. Section 5 gives the results and discussions. Major conclusions are listed in section 6.

2 Gravity-Driven Convection

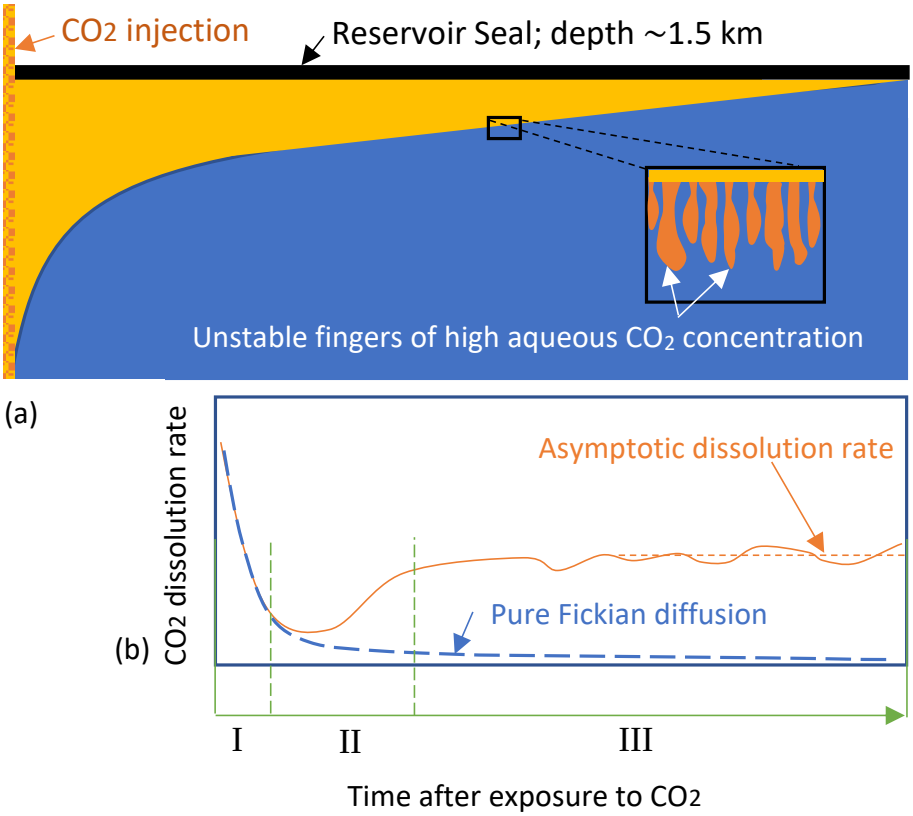

Figure 1: (a) Sketch of the appearance of unstable fingers at the interface of brine and CO_2-rich phase, and (b) enhanced dissolution rate due to vertical mass exchange driven by unstable fingers (I: diffusive regime; II: flux-growth regime; and III: constant-flux regime).

During the later stage of injection, the injected less dense CO_2-rich phase floats over the brine, as shown in Figure 1. This CO_2 moves upwards until it reaches a sealing caprock that traps the CO_2. The trapped CO_2 remains stored in the reservoir over extended periods, contributing to long-term carbon storage. Far from the injection site, a long quasi horizontal interface forms between the brine phase and the CO_2-rich phase. This interface represents a boundary of constant CO_2 concentration for the underlying brine, from which the overlying supercritical CO_2 dissolves into the brine. Importantly, brine with high CO_2 concentration has $\sim 1.0\%$ higher density than the underlying brine of very low CO_2 concentration, triggering Gravity-Driven Convection (GDC) that remarkably increases the CO_2 dissolution rate (see Figure 1). GDC continues until the whole reservoir is fully saturated with CO_2, which may take a long time. The dis-

solution process can be divided into 4 regimes [*Slim*, 2014; *Tsinober et al.*, 2022]. The first regime is called 'diffusive regime', in which the mass flux is controlled by Fickian diffusion that fades away exponentially, as can be seen from Figure 1. After this, GDC starts to develop and dissolution switches from diffusion controlled to convection controlled. During this regime, which is called 'flux-growth regime', the dissolution rate starts to increase. Once the GDC is fully developed, the dissolution rate reaches a quasi constant value for a relatively long time. This regime is known as 'constant-flux regime'. The last regime (not shown in Figure 1) is referred to as 'shutdown regime' or flux decay regime. In this regime, the dissolution rate decreases as the reservoir becomes fully saturated with CO_2 [*Elenius et al.*, 2015].

In this work, we focus on the dissolution rate taking place in the 'constant-flux regime'. This regime controls the overall behavior of the dissolution efficiency during the geological carbon sequestration [*Tsinober et al.*, 2022]. In this 'constant-flux regime', the dissolution rate can be approximated by an asymptotic dissolution rate, as shown in Figure 1.

3 Review of Formulas for GDC-Driven Dissolution Rates

In isotropic homogeneous porous media, the asymptotic dissolution rate [kg·m^{-2}·s^{-1}] can be written as [e.g., *Hesse*, 2008; *Pau et al.*, 2010; *Slim*, 2014],

$$F_\infty = \gamma X_0^C \rho_0 \frac{\Delta\rho g \kappa}{\overline{\mu}}, \tag{1}$$

where γ [-] is a scaling coefficient, X_0^C [kg·kg^{-1}] and ρ_0 [kg·m^{-3}] respectively represent the CO_2 mass fraction in brine and the brine density at the interface of brine and CO_2-rich phase, $\Delta\rho$ [kg·m^{-3}] is the density increase when aqueous CO_2 mass fraction increases from the initial very small background value to X_0^C, g [m·s^{-2}] is the gravitational acceleration, κ [m^2] is the intrinsic permeability, and $\overline{\mu}$ [pa·s] is the mean viscosity of brine. Different researches have obtained different values for the scaling coefficient γ that varies from ~ 0.015 to ~ 0.075, and a summary of γ is given in Table 1.

In heterogeneous porous media, the intrinsic permeability can vary by several orders of magnitude [*Elenius and Johannsen*, 2012; *Elenius et al.*, 2012]. Therefore, it is important to understand the effect of permeability heterogeneity on the GDC dissolution. Although there exists a large amount of studies on GDC dissolution in heterogeneous porous media [e.g. *Green and Ennis-King*, 2010; *Elenius and Gasda*, 2013; *Green and Ennis-King*, 2014; *Taheri et al.*, 2018; *Mahyapour et al.*, 2022], only a few researches offer concise formulas for predicting the dissolution rate. By conducting numerical simulations in homogeneous medium with embedded horizontal barriers, *Elenius and Gasda* [2013] proposed that the asymptotic dissolution rate can be estimated by

$$F_\infty = \gamma X_0^C \rho_0 \frac{\Delta\rho g \kappa_g}{\overline{\mu}} \left(\frac{\kappa_z^e}{\kappa_g}\right), \tag{2}$$

where κ_z^e is the equivalent vertical intrinsic permeability of the heterogeneous medium, and κ_g is the geometric mean of the permeability field. Essentially, these authors proposed to replace the intrinsic permeability by its equivalent quantity in heterogeneous media. Subsequent studies analyze whether and how the anisotropic effect of the permeability distribution affects the GDC, but the results are inconsistent [*Xu et al.*, 2006; *Green and Ennis-King*, 2010; *Cheng et al.*, 2012; *Chen et al.*, 2013; *Green and Ennis-King*, 2014; *Kim*, 2014; *Soltanian et al.*, 2017; *Elgahawy and Azaiez*, 2021]. Inspired by the result for the isotropic heterogeneous field, researchers propose that the dissolution rate in the anisotropic heterogeneous field can be expressed by

$$F_\infty = \gamma X_0^C \rho_0 \frac{\Delta\rho g \kappa_g}{\overline{\mu}} \left(\frac{\kappa_z^e}{\kappa_g}\right) \left(\frac{\kappa_x^e}{\kappa_z^e}\right)^\eta, \tag{3}$$

Table 1: Published data for the scaling coefficient γ in isotropic homogeneous field.

γ	**Top boundary**	**Method**	**Reference**
0.015-0.017	diff. only[a]	Num.	*Pruess and Zhang* [2008]
0.017	diff. only	Num.	*Hesse* [2008]
0.017-0.018	diff. only	Num.	*Pau et al.* [2010]
$0.12Ra^{-0.16}$[e]	-	Num.,Exp.	*Neufeld et al.* [2010]
$0.045Ra^{-0.24}$	Permeable	Exp.	*Backhaus et al.* [2011]
0.017	diff. only	Num..	*Cheng et al.* [2012]
0.02	diff. only	Num.	*Elenius and Johannsen* [2012]
0.02	diff. only	Num.	*Elenius et al.* [2012]
0.075	CTZ[b]	Num.	*Elenius et al.* [2012]
$0.037Ra^{-0.16}$	Permeable	Exp.	*Tsai et al.* [2013]
$0.0794Ra^{-0.168}$	diff. only	Theor.	*Farajzadeh et al.* [2013]
0.017	diff. only	Num.	*Slim* [2014]
0.025	(0.2κ[c])	Num.	*Slim* [2014]
0.044	(0.6κ[d])	Num.	*Slim* [2014]
0.065	CTZ	Num.	*Martinez and Hesse* [2016]
0.018-0.019	diff. only	Num.	*Martinez and Hesse* [2016]
$Ra^{-0.2154}$, 0.06	Permeable	Exp.	*Rasmusson et al.* [2017]
0.09	Permeable	Num.	This study

[a] The top boundary only allows mass to go through the boundary via diffusion.
[b] The top boundary is capillary transition zone.
[c] The permeability of the top boundary is 0.2 the permeability of the domain.
[d] The permeability of the top boundary is 0.6 the permeability of the domain.
[e] Ra is Rayleigh number (cf. [*Neufeld et al.*, 2010]).

where κ_x^e is the equivalent intrinsic permeability along the horizontal direction, and the exponent η describes the impact of anisotropy. The last term represents the anisotropic effect described by the horizontal to vertical equivalent permeability ratio. By conducting numerical simulations of GDC dissolution in homogeneous media with embedded horizontal barriers, which is similar to the aforementioned method used by *Elenius and Gasda* [2013], *Green and Ennis-King* [2014] found that $\eta = 0.5$, which indicates that dissolution increases with horizontal to vertical equivalent permeability ratio. Note that when $\eta = 0.5$, the dissolution rate is actually proportional to the geometric mean of the permeabilities $\sqrt{\kappa_x^e \kappa_z^e}$. In contrast, *Erfani et al.* [2022] give $\eta = 0.21$. However, the results from *Soltanian et al.* [2017] and *Elgahawy and Azaiez* [2021] show that the increasing κ_x^e at fixed κ_z^e can reduce the asymptotic dissolution rate, implying that η may be negative.

4 Computational Approach

4.1 Model Setup

We conduct numerical simulations of Gravity-Driven Convection (GDC) over two-dimensional vertical fields of various permeability heterogeneity, which varies in space as a function of the horizontal and vertical distances. We assume that the interface between the CO_2-rich phase and brine is horizontal under buoyancy force, and that the brine at the interface is always saturated with CO_2. We only study the portion below the interface and therefore all simulations are conducted with a single-phase model. Initially, the CO_2 concentration in brine is very low and the system is at static state. CO_2 enters into the domain through the top boundary that has fixed high CO_2 mass fraction. Brine is represented by a high-concentration Sodium Chloride (NaCl) solution. The objective is to get a quantitative relation between representative properties of the heterogeneous field and the CO_2 dissolution rate through the top boundary.

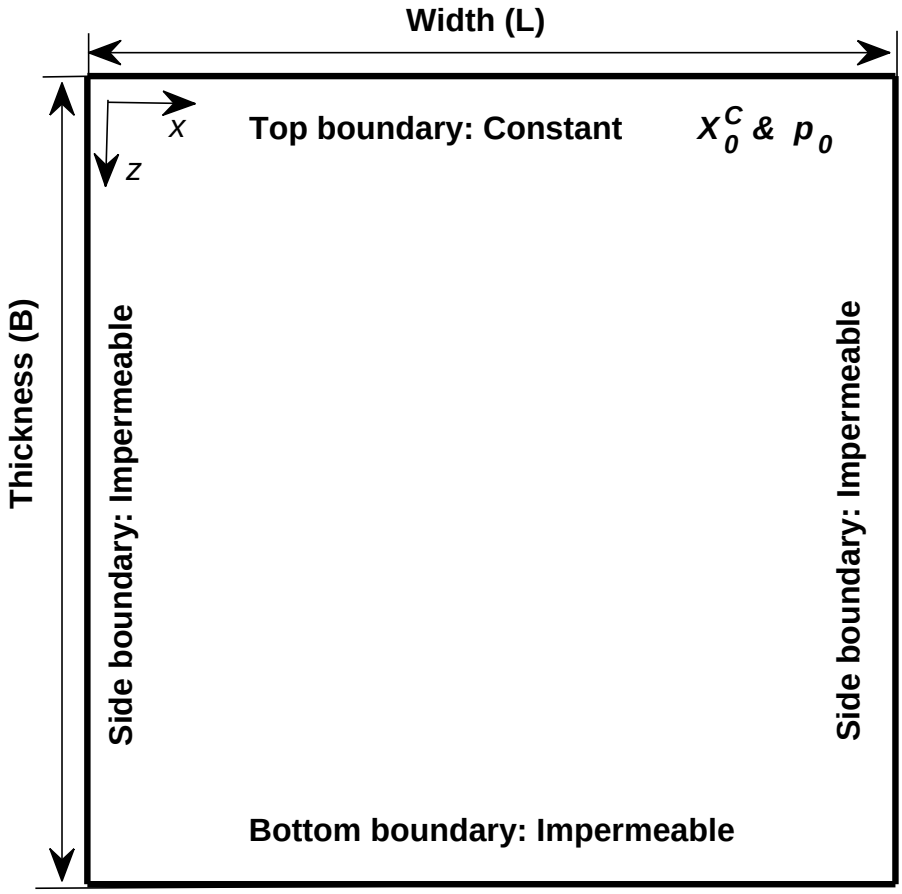

Figure 2: Sketch of setup design.

Figure 2 shows the two-dimensional vertical domain used to simulate the development of dissolution process enhanced by GDC. Detailed parameter settings are as follows. The top boundary, which represents the interface between brine and CO_2-rich phase, has constant liquid pressure $p_0 = 150$ [bar] and constant CO_2 mass fraction $X_0^C = 0.041$ [kg·kg^{-1}]. The bottom and lateral boundaries are no-flow boundaries. Initially, the brine has a very low background CO_2 mass fraction $X_{bg}^C \approx 0.0006$ [kg·kg^{-1}]. An initial brine pressure of p_0 =150 [bar] is imposed at the top layer and increases downwards at a gradient of ρg, which means that the brine is initially at hydrostatic state. The temperature (T_c) is fixed to 60 [°C], and the salinity of brine (m^S) is constant 0.5 [molal]. When the mass fraction of aqueous CO_2 increases from initial X_{bg}^C to X_0^C on the top boundary, the density of brine increases by $\Delta\rho = 8.2$ [kg·m^{-3}]. We note that the viscosity of the brine slightly changes from 1.0 [mpa·s] at the minimum background CO_2 mass fraction (X_{bg}^C) to 0.9 [mpa·s] at the maximum CO_2 mass fraction (X_0^C). Thus, the mean viscosity is approximated by $\overline{\mu}$ = 0.95 [mpa·s]. Table 2 summarizes the parameters that are used in the numerical simulations.

We note that the top boundary condition is different from most of those used in literature where the convection of the CO_2-saturated layer is either totally or partially suppressed (see Table 1). For instance, in *Pau et al.* [2010], the top constant concentration boundary only allows CO_2 to enter the domain via diffusion; this top boundary condition generates a much lower dis-

Table 2: Summary of the parameters adopted during numerical simulations.

Parameters	**Symbol**	**Units**	**Values**
Domain size	$L \times B$	[m ×m]	7.5×7.5
Grid discretization	$n_x \times n_z$	[-]	100×100
Porosity	ϕ	[-]	$0.15^{c,f}$
Geometric mean permeability	κ_g	[m^2]	10^{-12} ^{b,i}
Initial liquid pressure at top layer	p_0	[bar]	150 ^{h}
Initial background CO_2(aq) mass fraction	X^C_{bg}	[kg·kg^{-1}]	$\sim 0.0006^{g,j}$
CO_2(aq) mass fraction at top boundary	X^C_0	[kg·kg^{-1}]	0.041
Brine density at top boundary	ρ_0	[kg·m^{-3}]	1017
Brine density increase due to increased CO_2(aq) mass fraction	$\Delta\rho$	[kg·m^{-3}]	8.2
Salinity	m^S	[molal]	0.5 ^{e,i}
Mean viscosity	$\overline{\mu}$	[mpa·s]	0.95
Molecular diffusion coefficient	D	[m^2· s^{-1}]	2×10^{-9} ^{d,i}
Temperature	T_c	[°C]	$60^{a,k}$

Reference: [a] *Spycher et al.* [2003]; [b] *Chadwick et al.* [2004]; [c] *Maldal and Tappel* [2004]; [d] *Tewes and Boury* [2005]; [e] *Spycher and Pruess* [2005]; [f] *Mathieson et al.* [2009]; [g] *Xu et al.* [2007]; [h] *Iding and Ringrose* [2010]; [i] *Elenius and Johannsen* [2012]; [j] *Saaltink et al.* [2013]; [k] *Strandli and Benson* [2013].

solution rate. In some studies the top boundary is partially permeable and larger dissolution rates are obtained [*Hesse*, 2008; *Elenius et al.*, 2014; *Rasmusson et al.*, 2015]. Although it is more realistic to add a capillary transition zone beneath the top boundary [*Elenius et al.*, 2015], experimental results with totally permeable top boundaries [*Rasmusson et al.*, 2017] show only little discrepancy from the numerical results obtained in a model that includes the capillary transition zone [*Martinez and Hesse*, 2016]. Therefore, we employ the single phase flow model with permeable top boundary in this study, although our model is capable of two-phase flow simulations [*Wang et al.*, 2022].

An initial perturbation of the initial CO_2 mass fraction on the top boundary is added to stimulate the onset of instability at the beginning of simulation. We added a white noise that follows an uncorrelated Gaussian distribution [*Fu et al.*, 2013]. The magnitude of the noise is 1% of the initial mass fraction. *Hidalgo and Carrera* [2009] show that instability can be generated by the numerical error without introducing any external noise. Certainly, even though larger noise strength tends to accelerate the appearance of instability fingers, it is however unlikely to change the statistic behavior of the dissolution rate once the instability has fully developed [*Hidalgo and Carrera*, 2009; *Elenius and Johannsen*, 2012].

4.2 Governing Equations

On the basis of the mass balances of water and CO_2 species, the two governing transport equations are constructed as,

$$0 = \frac{\partial(\phi\rho X^H)}{\partial t} + \nabla\cdot(\rho X^H \boldsymbol{q}) - \nabla\cdot(\phi \boldsymbol{D}\rho\nabla X^H), \tag{4}$$

$$0 = \frac{\partial(\phi\rho X^C)}{\partial t} + \nabla\cdot(\rho X^C \boldsymbol{q}) - \nabla\cdot(\phi \boldsymbol{D}\rho\nabla X^C), \tag{5}$$

where ϕ [-] is the porosity of the saline formation, ρ [kg·m^{-3}] represents the density of brine, X [kg·kg^{-1}] is the mass fraction, superscripts (H, C) represent the water and aqueous CO_2 species, respectively, t [s] denotes the time, $\boldsymbol{D} = D\boldsymbol{I}_d$ [m^2·s^{-1}] denotes the dispersion tensor, which is assumed locally constant. Local dispersion has little impact on the asymptotic dissolution rates, which is the objective of this work [*Prasad and Simmons*, 2003; *Hidalgo and Carrera*, 2009]. The discharge rate ($\boldsymbol{q}$) is given by Darcy's law

$$\boldsymbol{q} = -\frac{\kappa}{\mu}(\nabla p - \rho g \nabla z), \tag{6}$$

where κ [m^2] is the intrinsic permeability, μ [pa· s] is the viscosity, p [pa] is the liquid pressure, and z [m] is the depth. Besides, we have the following constraints:

$$X^S = 0.05844 X^H m^S, \tag{7}$$

and

$$X^H + X^C + X^S = 1, \tag{8}$$

where m^S denotes the molality of salt. Here, we assume that the salt comprises only NaCl, and the molality of NaCl (m^S) is fixed. Define $\omega = (1 + 0.05844 m^S)$ and then Equations (7) and (8) merge to

$$\omega X^H + X^C = 1. \tag{9}$$

Under isotherm and isosalinity condition, ρ and μ are only governed by liquid pressure and aqueous CO_2 mass fraction (see Appendix A).

4.3 Dimensionless variables

In order to facilitate the analysis, results are presented using the following dimensionless variables, which are defined based on the works of *Ennis-King and Paterson* [2003] and *Rasmusson et al.* [2017],

$$X^{C*} = \frac{X^C}{X_0^C}, \qquad X^{H*} = \frac{X^H}{X_0^H}, \tag{10}$$

and

$$t^* = \frac{t}{t_c}, \qquad x^* = \frac{x}{L_c}, \qquad z^* = \frac{z}{L_c}, \tag{11}$$

where X_0^C and X_0^H are, respectively, the maximum CO_2 and water mass fractions, and t_c and L_c are the characteristic time and length scale of the gravity-driven convection problem defined as

$$t_c = \frac{(\overline{\mu}\phi)^2 D}{(\Delta\rho g \kappa_g)^2}, \qquad L_c = \frac{\overline{\mu}\phi D}{\Delta\rho g \kappa_g}. \tag{12}$$

The characteristic time t_c has been found to be closely related to the onset time of gravity-driven convection, and the characteristic length L_c closely related to the earliest finger width. In our simulations, we found that the earliest finger width, denoted as ℓ_c, can be approximated by $\ell_c \approx 70 L_c$. The governing equations are expressed in dimensionless form in the Appendix B.

Importantly, by expressing Darcy's law and the global dissolution rate in dimensionless form, we obtain that

$$q^* = \frac{q}{q_c}, \qquad q_c = \frac{\Delta\rho g \kappa_g}{\overline{\mu}}, \tag{13}$$

$$F^* = \frac{F}{F_c}, \qquad F_c = X_0^C \rho_0 \frac{\Delta\rho g \kappa_g}{\overline{\mu}}. \tag{14}$$

The characteristic velocity $v_c = q_c/\phi$ is closely related to the finger-tip velocity (see *Elenius and Johannsen* [2012]). We note that although the vertical length scale (i.e., domain thickness) and related dimensionless number (e.g., Rayleigh number) have been typically used to study gravity instability in the literature [*Rasmusson et al.*, 2017, and references therein], herein we do not use it because the vertical domain size has little impact on the asymptotic enhanced dissolution rate driven by instability fingers [*Elenius et al.*, 2015; *Tsinober et al.*, 2022]. This definition of the dimensionless length scale without using the domain thickness indicates that the instability is a random statistic behavior that does not change with the domain size provided that the domain is large enough to accommodate sufficient number of density fingers. In the supporting information, we have shown that increasing the vertical domain size employed in this work does not systematically affect the asymptotic dissolution rate [*Elenius and Johannsen*, 2012]. *Simmons et al.* [2001] give a detailed discussion of the limitation of using Rayleigh number based on the domain thickness.

4.4 Heterogeneity

The intrinsic permeability is the only aquifer property considered to vary in space. We represent the natural logarithm of the intrinsic permeability, denoted as $Y = \ln \kappa$, by a random space function to create multiple realizations of the aquifer permeability distribution. The random space function model is characterized by an exponential covariance function with mean ($\overline{Y}$), variance (σ_Y^2), horizontal correlation length (λ_h) and vertical correlation length (λ_v). The geometric mean of the intrinsic permeability is fixed to $\kappa_g = 10^{-12}$ m^2. Different degrees of heterogeneity and correlation anisotropy $\Omega = \lambda_h/\lambda_v$ are explored with σ_Y^2 ranging between highly homogeneous, σ_Y^2=0.1, to relatively highly heterogeneous, σ_Y^2=4, and Ω ranging between isotropic, Ω =1, and perfectly stratified, $\Omega = \infty$. The perfectly stratified random field is formed by separate horizontal layers of constant properties. The vertical correlation length is fixed to $\lambda_z = 2L_c$, and the horizontal correlation length is $\lambda_x = \Omega \cdot \lambda_z$. For comparison purposes, we also considered a homogeneous medium with $\kappa = \kappa_g$. In total, we conduct GDC simulations with 365 realizations. Random fields were generated using the sequential Gaussian simulation method implemented in the SGSIM code of GSLIB [*Journel and Huijbregts*, 1976; *Deutsch et al.*, 1992]. Table 3 summarizes the statistical properties of the random fields. An illustrative realization of each random field type is shown in Figure 4.

Table 3: Permeability heterogeneity adopted for the numerical simulations. The vertical correlation length is fixed to $\lambda_z = 2L_c$, and the horizontal correlation length is $\lambda_x = \Omega \cdot \lambda_z$.

Case	$\boldsymbol{\Omega}$	$\boldsymbol{\sigma_Y^2}$
Homogeneous	-	-
Isotropic	1	1
Isotropic	1	4
Anisotropic	2	0.1
Anisotropic	2	1
Anisotropic	4	0.1
Anisotropic	4	1
Anisotropic	4	4
Anisotropic	∞	1

4.5 Global Measures

Simulation results are analyzed based on two global measures of the dissolution behavior. The global dissolution rate (F [kg·m^{-2}·s^{-1}]) is defined as the rate at which CO_2 dissolves from the upper boundary at z=0. This can be expressed as [*Hidalgo and Carrera*, 2009]

$$F(t) = \frac{1}{L}\int_0^L \left[\rho X^C q_z - \phi D \rho \frac{\partial X^C}{\partial z}\right]_{z=0} dx. \tag{15}$$

Initially, the domain is stable, the convection flux is zero, and only molecular diffusion transports downwards the dissolved CO_2. The density-driven unstable convection does not emerge until the CO_2 mass fraction distribution reaches a critical point. After this, the dissolution rate rapidly increases to a quasi constant value until the domain is almost totally saturated with aqueous CO_2. In our simulations, the asymptotic value of the global dissolution rate F_∞ is estimated as the temporal average of $F(t)$ over the period of $[t_b/3, t_b]$, where t_b is the time when the earliest finger of aqueous CO_2 reaches the bottom (time when the maximum bottom CO_2 mass fraction exceeds 25% of X_0^C).

Another important global parameter that describes the vertical migration or the penetration depth of the CO_2 plume is the vertical finger-tip velocity [*Prasad and Simmons*, 2003]. The representative vertical finger-tip velocity of the CO_2 plume is estimated as,

$$v(t) = \max_{0<z<B}\left\{\frac{1}{L}\int_0^L \frac{1}{\phi} \mid q_z \mid dx\right\}. \tag{16}$$

Figure 3 illustrates the concept of vertical finger-tip velocity in our simulations. Similar to the global dissolution rate behavior, the vertical finger-tip velocity also reaches an asymptotic value [*Elenius and Johannsen*, 2012] in the constant-flux regime and remains at that value until the field is almost saturated. The asymptotic vertical finger-tip velocity v_∞ is also estimated by the temporal average of $v(t)$ over the time interval $[t_b/3, t_b]$.

In order to characterize the overall hydraulic behavior of the permeability field, we estimated the equivalent permeability along the horizontal κ_x^e and vertical κ_z^e direction for each realization of the random fields. For this, to estimate κ_i^e ($i = x, y$), we neglect gravity and saturate the porous medium with only water. We then set the domain sides perpendicular to the ith direction as impermeable, and we impose a pressure decrement $|\Delta_i p|$ along the ith direction. κ_i^e is estimated by the total volumetric flow Q_i passing through the system in the ith direction as $\kappa_i^e = \mu Q_i L_i/(A_i|\Delta_i p|)$, where L_i is the domain size along the ith direction and A_i the corresponding cross-sectional area [*Knudby and Carrera*, 2005; *Wang*, 2022].

4.6 Numerical Features

The model is implemented in a Matlab reservoir simulator toolbox designed for CO_2 storage [*Wang*, 2022]. The program is based on the finite volume method. The two governing equations (4) and (5) are solved simultaneously with an implicit Newton-Raphson method. Two-point flux approximation with up-winding scheme is used to calculate mass transport. Although the unconditional stable implicit method is employed, we should still control the time step in the numerical simulation to avoid significant numerical dispersion. In this work, the time step is limited by either advection ($\Delta t < \Delta l\phi/(\boldsymbol{q}\cdot\boldsymbol{n})$) or diffusion ($\Delta t < \sqrt{\Delta l/(2D\phi)}$), whichever is smaller. Here, Δl and $\boldsymbol{n}$ are respectively the distance between the centroids of two adjacent cells and the unitary perpendicular vector to their interface. Detailed implementation of this numerical solution and related source code can be found in our previous works [*Wang et al.*, 2022, 2023].

The numerical discretization consists in 100×100 squared cells of equal size. The cell size is chosen to strike a balance between capturing small instability fingers and managing computational expenses without compromising accuracy following *Lindeberg and Bergmo* [2003] and

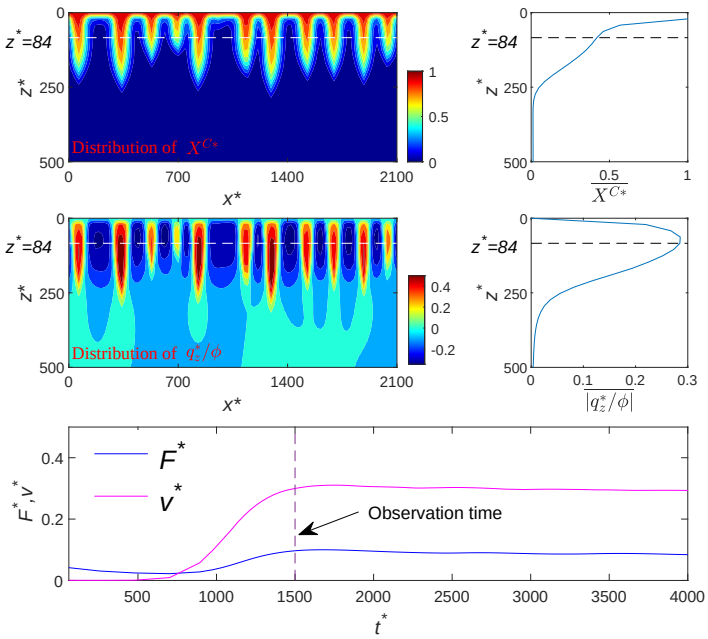

Figure 3: Maps of the dimensionless CO_2 mass fraction (X^{C*}) and its horizontal average ($\overline{X^{C*}}$), the dimensionless vertical flow velocity (q_z^*/ϕ) and the horizontal average of absolute dimensionless vertical flow velocity ($\overline{|q_z^*/\phi|}$), and temporal the development of dimensionless dissolution rate (F^*) and finger velocity (v^*) in an illustrative realization. The dimensionless finger velocity is represented by $v^* = \max \overline{|q_z^*/\phi|}$.

Elenius et al. [2015]. The grid size is smaller than the finger width, $\Delta = 0.3\ell_c = 21L_c$, and at the same time the shortest correlation length is described by at least 7 grid cells. We note that the finger width ℓ_c is close to the approximate value $4\pi^2 L_c$ needed for the generation of instability [*Lapwood*, 1948].

4.7 Effective Asymptotic Dissolution Models

Two effective dissolution models are proposed here based on previous results reported in literature (see Section 3) with the objective to offer a simplified representation of the overall asymptotic dissolution behavior in naturally occurring heterogeneous porous media. In the first effective model, we have extended the formula (3) to a more general expression that incorporates the effect of anisotropy. In dimensionless form, the model expresses that

$$F^*_\infty = \gamma_1 \left(\frac{\kappa^e_z}{\kappa_g}\right)^{\alpha_1} \left(\frac{\kappa^e_x}{\kappa^e_z}\right)^{\beta_1}. \tag{17}$$

Here, the dimensionless asymptotic dissolution rate is $F^*_\infty = F_\infty/F_c$. The last term on the right hand side of this expression represents the anisotropy of the permeability field, defined as $a_f = \kappa^e_x/\kappa^e_z$.

Existing effective asymptotic dissolution models rely exclusively on equivalent permeability values. Thus, it remains uncertain whether predictions of the dissolution rate can be made using field observations, such as the finger-tip velocity v_∞. For this, in the second model, we have considered the following relationship written in dimensionless form as

$$F^*_\infty = \gamma_2 \left(\frac{v_\infty}{v_c}\right)^{\alpha_2} \left(\frac{\kappa^e_x}{\kappa^e_z}\right)^{\beta_2}. \tag{18}$$

Essentially, this expression replaces the equivalent vertical permeability with the vertical finger velocity, which seems to offer a more direct description of the CO_2 plume migration. γ_1, γ_2, α_1, α_2, β_1 and β_2 are tuning coefficients of the two effective asymptotic dissolution models.

5 Results and Discussion

5.1 Impact of Heterogeneity

We first provide a general description of the impact of heterogeneity on the vertical migration of the CO_2 plume and dissolution rates. We focused on the influence of anisotropy in the correlation structure of permeability Ω and the degree of heterogeneity σ^2_Y. Figure 4 shows the temporal evolution of the spatial distribution of CO_2 mass fraction for different types of heterogeneity. For illustrative purposes, we chose a representative permeability realization for each case. These realizations are shown in the first panel of Figure 4. In all cases, results show that instability CO_2 fingers grow, merge and re-initiate as also observed in laboratory experiments [*Rasmusson et al.*, 2017; *Liyanage*, 2018; *Tsinober et al.*, 2022] and numerical simulations [*Elenius et al.*, 2015]. Importantly, from Figure 4, we can see that CO_2 fingering is strongly affected by heterogeneity. In particular, the presence of vertical well-connected high permeability zones (preferential channels) facilitates the initiation and growth of the instability fingers (see for instance the second column of Figure 4). Actually, the white randomness of the top CO_2 mass fraction (needed in homogeneous media to create instabilities) is redundant in heterogeneous porous media as instabilities are controlled by these vertical preferential channels. In accordance with *Simmons et al.* [2001], we also see that heterogeneity dissipates vertical finger growth through dispersive mixing. This effect increases with Ω, i.e., when horizontal well-connected high-permeability structures exist. This is strongly manifested in perfectly stratified media with σ^2_Y=1 and Ω=∞ (fourth column of Figure 4).

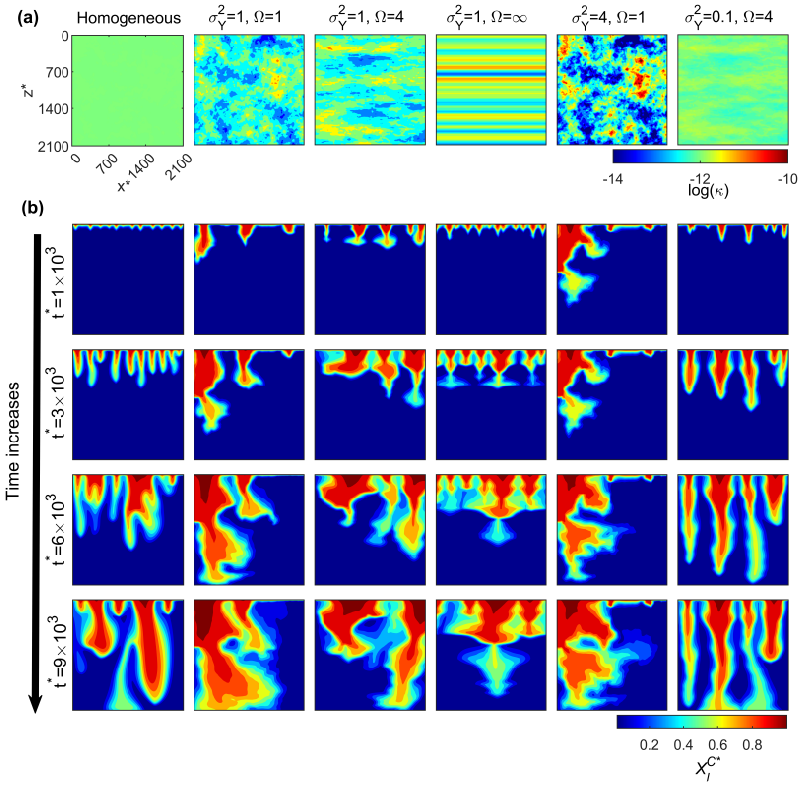

Figure 4: (a) Logarithm permeability ($\log(\kappa)$) distribution. (b) Development of dimensionless CO_2 mass fraction distribution ($X_l^{C^*}$) due to gravity-driven convection.

For completeness, we also show the temporal evolution of the dissolution rate as a function of σ_Y^2 and Ω in Figure 5. Results are presented in terms of the ensemble average and the coefficient of variation of $F^*(t^*)$. As expected, in homogeneous media, the dissolution process, shows the three well-known stages: an initial diffusion-controlled decrease, followed by an onset of nonlinear growth at $t^* = 500$ due to instability, and eventually stabilizing at an approximately constant dissolution rate. However, in heterogeneous media, results show in all cases that the early-time evolution of $F^*(t^*)$ in heterogeneous media is remarkably different than that in homogeneous media. The diffusive and the flux-growth regimes cannot be distinguished anymore and the system seems to be controlled by the interaction between gravity-driven convection and heterogeneity, indicating that heterogeneity helps triggering the onset of instability. This is consistent with results reported by *Schincariol et al.* [1997] and *Simmons et al.* [2001]. Of course, this also indicates that caution is needed when using the onset time of instability for homogeneous media [*Ennis-King and Paterson*, 2005; *Pruess and Zhang*, 2008] in real applications.

The influence of σ_Y^2 and Ω can also be seen from Figure 5. Interestingly, in statistically isotropic heterogeneous media, the degree of heterogeneity σ_Y^2 significantly influences the early behavior of $F^*(t^*)$, eventually converging to a similar asymptotic dissolution rate at large times. This suggests that the asymptotic dissolution rate might be governed by the existence of well-connected high-permeability zones, regardless of the specific high value of permeability. This effect is not seen in anisotropic heterogeneous media where we found that the higher the σ_Y^2 the lower is the

asymptotic dissolution rate. We attribute this to the fact that, when $\Omega > 1$, an increase in σ_Y^2 produces stronger well-connected permeability layers that inhibits gravity-driven convection. For the same reason, for equal σ_Y^2, the higher anisotropy Ω the less significant is the asymptotic dissolution rate. We also report in this figure a measure of the uncertainty in $F^*(t^*)$ given by the coefficient of variation (CV). We can observe that the coefficient of variation reaches a similar asymptotic value for all cases, regardless of the degree of heterogeneity. A similar trend is also observed for the vertical finger velocity, as shown in the second column of Figure 5, indicating a close relation between the dissolution rate and the vertical finger velocity.

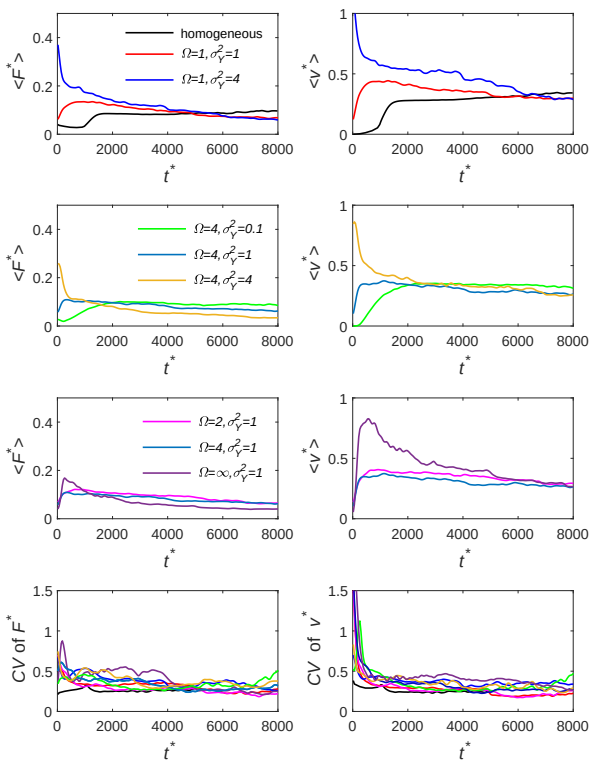

Figure 5: The temporal evolution of the ensemble average of the dimensionless dissolution rate ($\langle F^* \rangle$) through the top boundary and ensemble average of the dimensionless finger velocity ($\langle v^* \rangle$) for all the test cases listed in Table 3. Here, we also give the coefficient of variation (CV), which is the ratio of standard division to the ensemble average.

5.2 The Effective Asymptotic Dissolution Rate

The tuning coefficients of the two effective asymptotic dissolution models were independently adjusted by regression analysis of all simulation data obtained from the 365 realizations of the permeability distributions. These realizations involved random fields with different correlation structures of permeability and degrees of heterogeneity. To do this, we used Ordinary Least Squares (OLS) regression of the natural logarithm of the dissolution rate models (17) and (18). We respectively obtained a coefficient of determination R^2 of 0.71 and 0.84. The significance of all regression coefficients was below 0.05, meaning that both models can properly explain dissolution rates. Table 4 provides a summary of the regression analysis. Similar to the val-

ues reported in the literature, we find that $\alpha_1 = 1.1$, which is close to unity, meaning that the effective dissolution efficiency is almost linearly proportional to the equivalent vertical permeability. Moreover, we find that, in anisotropic heterogeneous media, the anisotropy of the equivalent permeability ($a_f = \kappa_x^e/\kappa_z^e$) can reduce the effectiveness of dissolution with a power law behavior given by $\beta_1 = -0.2$. This contradicts previous results obtained in homogeneous media with embedded horizontal impermeable inclusions [*Green and Ennis-King*, 2014; *Erfani et al.*, 2022], which indicated that $\beta_1 > 0$.

Table 4: Coefficients for effective asymptotic dissolution models obtained from OLS regression of all simulation data; the results from literature are also listed for comparison.

Predictors	**Coefficients**	**Values**	**MAE**	**RMSE**	**Source**
(17)	$(\gamma_1, \alpha_1, \beta_1)$	(0.08, 1.1,-0.2)	27%	22%	This work
(18)	$(\gamma_2, \alpha_2, \beta_2)$	(0.33, 1.0,-0.3)	20%	19%	This work
(17)	$(\gamma_1, \alpha_1, \beta_1)$	(0.09*, 1.0, 0)	40%	24%	*Elenius and Gasda* [2013]
(17)	$(\gamma_1, \alpha_1, \beta_1)$	(0.09*, 1.0, 0.5)	76%	44%	*Green and Ennis-King* [2014]

* Here, we update the value for the reference dissolution rate in the homogeneous case, because the original value was around 0.02 based on the impermeable top boundary (cf. Table 1).

Figure 6 compares the asymptotic dissolution rate predicted by the proposed asymptotic dissolution rate models, expressions (17) and (18), with corresponding simulated values. For completeness, we also show the performance of the reported expressions given by *Elenius and Gasda* [2013] and *Green and Ennis-King* [2014]. We visually differentiate between isotropic and anisotropic random fields. We can see that the predictor given by *Green and Ennis-King* [2014] significantly overestimates the dissolution rate in anisotropic random fields. Actually, the expression by *Green and Ennis-King* [2014] does not seem to improve the prediction given by *Elenius and Gasda* [2013]. The second effective dissolution model given by equation (18), proposed here based on the vertical finger-tip velocity, shows the best performance, indicating that the dissolution rate has a strong relationship with the finger-tip velocity. The Mean Absolute Error (MAE) for formulas (17) and (18) are 27% and 20%, respectively. These error are well accepted considering that even in homogeneous fields, the dissolution rate can fluctuate around 15% [*Pau et al.*, 2010].

In this work, we found a negative impact of the anisotropy of the permeability field a_f on dissolution rates. This can be physically explained in the following manner. Instabilities in the form of fingers exhibit nonuniform periodic high concentration distributions along the horizontal direction. When the spatial continuity of permeability values in the horizontal plane is substantial, any nonuniform concentration in this direction is rapidly eradicated by the enhancement of horizontal mixing induced by the introduction of companion horizontal flows. Consequently, the formation of finger-like instabilities becomes more challenging, especially in scenarios with high horizontal permeability values. In accordance, *Schincariol et al.* [1997] show that increasing the horizontal correlation length of the permeability distribution (increase in κ_x^e), can effectively inhibit instability growth and stabilize perturbations. Through numerical simulations in a wide variety of heterogeneous fields, *Simmons et al.* [2001], *Soltanian et al.* [2017] and *Elgahawy and Azaiez* [2021] also conclude that instability is dampened when κ_x^e/κ_z^e is relatively large. Recent studies by *Tsinober et al.* [2022] and *Hansen et al.* [2023] have also highlighted that the introduction of a minor horizontal background flow in geological carbon sequestration fields enhances horizontal mixing. This enhancement of mixing disrupts the growth of fingers, consequently leading to a reduction in the dissolution rate. All these works also suggest that horizontal flows have the potential to decrease nonuniform instabilities. To better illustrate this, Figure 7 shows simulated and estimated effective dissolution rates as a function aquifer properties $\{\kappa_z^e, \kappa_x^e/\kappa_z^e,$ and $v_\infty^*\}$. The figure shows a clear negative dependence of the asymptotic dissolution rates with permeability anisotropy.

We acknowledge that our numerical simulations have not covered cases with $a_f < 1$, which are uncommon in natural sediment formations. Studies conducted by *Simmons et al.* [2001] have demonstrated that vertically stratified structures with $a_f < 1$ can encourage vertical unstable convection by diminishing horizontal dissipation in instability fingers. Thus, it is observed that instability becomes more pronounced when a_f is small, aligning with the findings of our study.

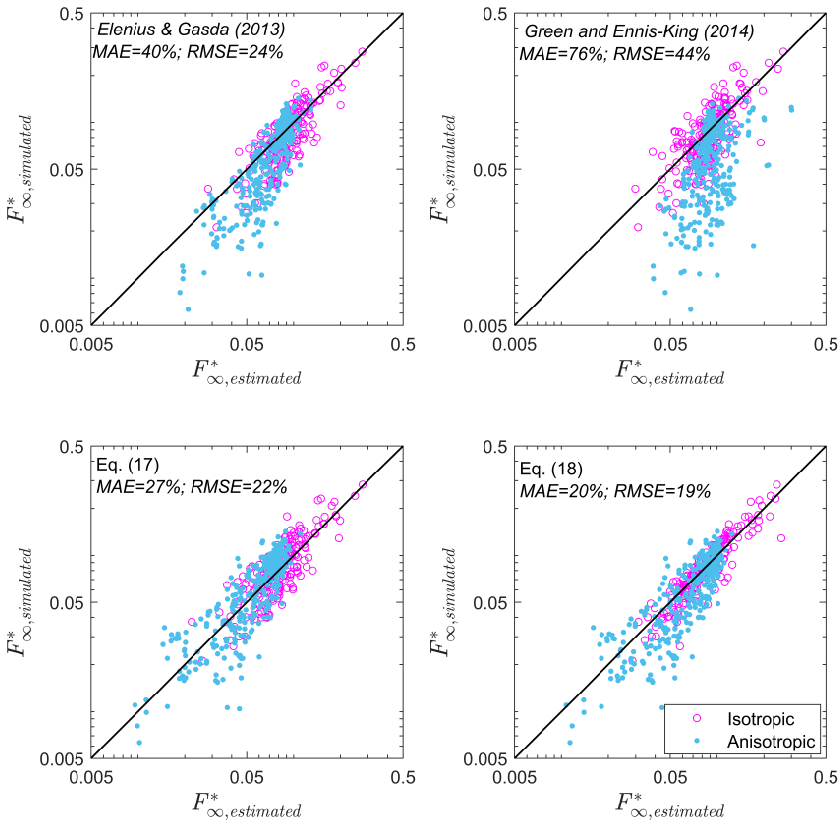

Figure 6: Comparison of the performances of the predictors given by *Elenius and Gasda* [2013], *Green and Ennis-King* [2014] and this work (cf. Table 4).

6 Conclusions

Geological Carbon Sequestration (GCS) in saline aquifers reduces the release of CO_2 into the atmosphere, thereby mitigating its impact on climate change. Once CO_2 is injected, the less dense CO_2-rich phase floats over the brine and gets trapped beneath an impermeable geological formation. At the interface between the brine phase and the CO_2-rich phase, CO_2 slowly dissolves into the brine, thereby reducing the risk of CO_2 leakage. Estimating CO_2 dissolution rates in this context is complex, as it requires characterizing the enhancement of dissolution due to Gravity-Driven Convection (GDC). GDC creates instability fingers that transfer the high CO_2 concentration brine downwards. While many studies offer a deep understanding of GDC in homogeneous porous media, less is known about dissolution rates in more realistic heterogeneous porous me-

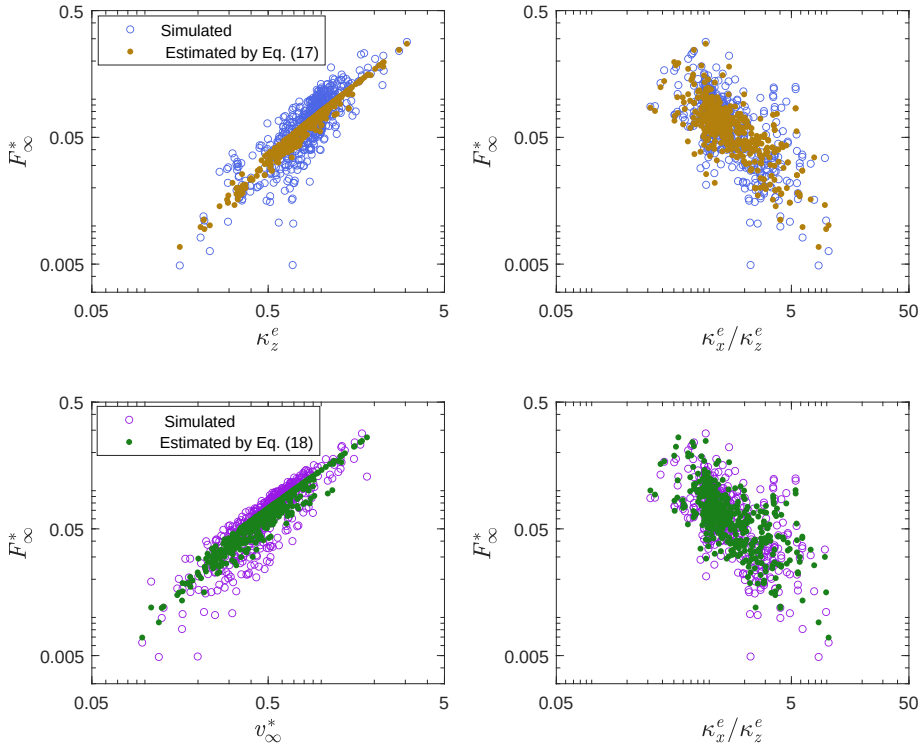

Figure 7: Simulated and estimated effective dissolution rates as a function aquifer properties.

dia. In this work, we have systematically analyzed the effect of heterogeneity on GDC-driven dissolution rates during GCS. To achieve this, we have conducted numerical simulations of GDC in multiple aquifer realizations of various permeability distributions. These distributions follow a random space function that exhibits distinct correlation structures (anisotropy) and degrees of heterogeneity. Based on these simulations, we have developed two effective asymptotic dissolution rate models derived from regression analysis of all the simulated data. The first model estimates the asymptotic dissolution rate using the aquifer's general hydraulic properties. For this model, we achieved a coefficient of determination (R^2) of 0.71, indicating a strong correlation between the variables compared to previous effective dissolution models [*Elenius and Gasda*, 2013; *Green and Ennis-King*, 2014],

$$F_\infty = 0.08 X_0^C \rho_0 \frac{\Delta\rho g \kappa_g}{\overline{\mu}} \left(\frac{\kappa_z^e}{\kappa_g}\right)^{1.1} \left(\frac{\kappa_x^e}{\kappa_z^e}\right)^{-0.2} . \tag{19}$$

This model requires some knowledge of the equivalent permeability value along the x and z directions $\{\kappa_x^e, \kappa_z^e\}$ and fluid properties. The equivalent permeability can be estimated by a wide variety of methods, including hydraulic tests (see *Renard and de Marsily* [1997]; *Sanchez-Vila et al.* [2006] for a review). Alternatively, direct observations of the CO_2 finger-tip velocity v can be used to estimate asymptotic dissolution rates. This velocity refers to the rate at which the fingers or plumes of dissolved CO_2 move downwards through the subsurface. Determining the finger-

tip velocity of CO_2 in the field involves the use of tracer tests, or geophysical or wellbore monitoring [*Würdemann et al.*, 2010; *Jenkins et al.*, 2015; *Michel-Meyer et al.*, 2020, and references therein]. Results have demonstrated that the finger-tip velocity offers a better estimate of dissolution rates with a coefficient of determination (R^2) of 0.84,

$$F_\infty^* = 0.33 X_0^C \rho_0 \frac{\Delta\rho g \kappa_g}{\overline{\mu}} \left(\frac{v_\infty}{v_c}\right)^{1.0} \left(\frac{\kappa_x^e}{\kappa_z^e}\right)^{-0.3}. \tag{20}$$

These effective asymptotic dissolution rate models express that the anisotropy of the permeability field (last term of the expressions) negatively affects dissolution rates. When permeability values have substantial spatial continuity horizontally, the corresponding increase in horizontal mixing inhibits nonuniform concentrations, making it harder for instabilities to form. These results differ from those presented by *Green and Ennis-King* [2014] in homogeneous media with horizontal barriers, where the dissolution rate is proposed to be enhanced by anisotropy with an exponent of 0.5. In accordance with our work, *Soltanian et al.* [2017] and *Elgahawy and Azaiez* [2021] demonstrated that increasing κ_x^e at fixed κ_z^e can reduce the asymptotic dissolution rate.

We have also explored the impact of heterogeneity on the temporal evolution of dissolution rates. We have shown that in heterogeneous porous media, vertical preferential channels, formed by well-connected high-permeability zones, play a significant role in initiating and developing instability fingers. Moreover, the presence of horizontal well-connected high-permeability structures inhibits the vertical growth of fingers by favoring dispersive mixing. Consequently, in anisotropic heterogeneous porous media, an increase in the degree of heterogeneity leads to a decrease in the asymptotic dissolution rate.

We note that the results from this study may have potential application to other common gravity-driven convection problems, such as contaminant migration, geothermal exploitation, saltwater intrusion and mineral precipitation/dissolution, where density differences may exist [*Zhang and Schwartz*, 1995; *Simmons et al.*, 1999; *Nield et al.*, 2008].

Acknowledgments

We acknowledge the help from Oriol Bertran-Oller and Rodrigo Perez in accessing the TITANI-high performance green computing cluster of the civil engineering school. Part of this work is done during Y. W.'s postdoc research at Dept. of Applied Mathematics, IFP Energies nouvelles, 1 et 4 Avenue du Bois-Préau, 92825 Rueil-Malmaison, France. Current correspondence of Y. W. is School of Earth and Space Sciences, Peking University, No.5 Yiheyuan Road Haidian District, 10087 Beijing, China. This work was partially supported by the European Commission, through project MARSOLUT (grant H2020-MSCA-ITN-2018); by the Spanish Ministry of Economy and Competitiveness, through project MONOPOLIOS (RTI 2018-101990-B-100, MINECO/ FEDER); and by the Catalan Agency for Management of University and Research Grants through FI 2017 (EMC/2199/2017).

A Density and Viscosity

In the numerical model, instead of using a simplified linear expression of the brine density based on the aqueous CO_2 concentration [e.g., *Elenius et al.*, 2015; *Martinez and Hesse*, 2016], we incorporated a more realistic brine density expression derived from [*Vilarrasa*, 2012], given the sensitivity of instability to the fluid property [*Jafari Raad et al.*, 2016; *Rasmusson et al.*, 2015, 2017]. In this model, the brine density, ρ [kg· m^{-3}], depends on brine phase pressure, temperature, molality of NaCl and CO_2 concentration. The expression for brine is given by *Garcia* [2003]

$$\rho = \rho_{lr} + cM^C - c\rho_{lr}V_\phi, \tag{A.1}$$

where c [mol·m^{-3}] is the number of moles of CO_2 per unit volume of brine phase; M^C [kg·mol^{-1}] is the molar mass of CO_2; and V_ϕ [m^3· mol^{-1}] is the apparent molar volume of CO_2 given by

$$V_\phi = 3.751 \times 10^{-5} - 9.585 \times 10^{-8} T_c + 8.74 \times 10^{-10} T_c^2 - 5.044 \times 10^{-13} T_c^3, \tag{A.2}$$

where T_c [°C] is temperature in Celsius; ρ_{lr} is the brine density when there is no CO_2 dissolution, calculated by *Phillips et al.* [1982]

$$\rho_{lr} = -3.033405 \times 10^3 + 1.0128163 \times 10^4 \iota - 8.750567 \times 10^3 \iota^2 + 2.66310 \times 10^3 \iota^3, \tag{A.3}$$

with

$$\begin{aligned} \iota = &- 9.9595 \exp\left(-4.539 \times 10^{-3} m^S\right) + 7.0845 \exp\left(-1.638 \times 10^{-4} T_c\right) \\ &+ 3.9093 \exp\left(2.551 \times 10^{-10} p\right), \end{aligned} \tag{A.4}$$

where m^S [molal] is the molality of NaCl and p [pa] is the pressure of brine. Equation (A.1) applies to $5 < T_c < 297$ [°C] and $p_{sv} < p < 300$ [bar]. Equation (A.3) applies to $10 < T_c < 350$ °C, $0.25 < m_l^S < 5$ [molal] and $p_{sv} < p < 500$ [bar] [*Phillips et al.*, 1982]. Here, p_{sv} is saturated vapor pressure. Rearranging Equation (A.1), we have [*Vilarrasa*, 2012]

$$\rho = \rho_{lr} \frac{1}{1 - X^C f_\delta} \approx \rho_{lr} (1 + X^C f_\delta), \tag{A.5}$$

with

$$f_\delta = 1 - \rho_{lr} \frac{V_\phi}{M^C}; \tag{A.6}$$

here X^C denotes the mass fraction of CO_2. The viscosity of brine is calculated following the works of *Garcia* [2003] and *Kumagai and Yokoyama* [1999]

$$\begin{aligned} \mu =& (3.85971 - 1.32561 \times 10^{-2} T_k) m^S + (-5.37539 + 1.90621 \times 10^{-2} T_k)(m^S)^{1/2} \\ &+ (8.79552 - 3.17229 \times 10^{-2} T_k) m^C + (-7.22796 + 2.64498 \times 10^{-2} T_k)(m^C)^2 \\ &+ 1.69956 \times 10^{-9} (p - 1 \times 10^5) + \mu_w (T_k, p = 10^5 [\text{Pa}]), \end{aligned} \tag{A.7}$$

where T_k [K] is temperature in Kelvin, m^C [molal] is the molality of CO_2, and μ_w [mPa· s] is the viscosity of pure water.

B Dimensionless Governing Equations

Given the dimensionless variables defined in section 4.2, the governing mass balance equations (4) and (5) can be written in dimensionless form as

$$\frac{\partial X^{C*}}{\partial t^*} = -\nabla^* \cdot \left(X^{C*} \boldsymbol{q}^* \right) + \nabla^* \cdot \left(\nabla^* X^{C*} \right), \tag{B.1}$$

$$\frac{\partial X^{H*}}{\partial t^*} = -\nabla^* \cdot \left(X^{H*} \boldsymbol{q}^* \right) + \nabla^* \cdot \left(\nabla^* X^{H*} \right), \tag{B.2}$$

where Darcy's law is expressed as

$$\boldsymbol{q}^* = -\exp(Y')\,(\nabla^* p^* - \rho^* \nabla^* z^*)\,, \tag{B.3}$$

and $\nabla^* = [\partial/\partial x^*, \partial/\partial z^*]$. Y' is the deviation of the natural log of the intrinsic permeability from the mean, i.e., $Y' = Y - \langle Y \rangle$. The geometric mean permeability is $\kappa_g = \exp(\langle Y \rangle)$. The fluid pressure and the density are normalized by

$$p^* = \frac{p\kappa_g}{\mu\phi D}, \text{ and } \rho^* = \frac{\rho}{\Delta\rho}. \tag{B.4}$$

Open Research

This work has no data-sharing issues, because all of the results are obtained by numerical solutions and have been provided in the figures and tables.

References

Agartan, E., L. Trevisan, A. Cihan, J. Birkholzer, Q. Zhou, and T. H. Illangasekare (2015), Experimental study on effects of geologic heterogeneity in enhancing dissolution trapping of supercritical CO2, *Water Resources Research*, doi:10.1002/2014WR015778.

Anbar, S., and S. Akin (2011), Development of a linear predictive model for carbon dioxide sequestration in deep saline carbonate aquifers, *Computers & geosciences*, *37*(11), 1802–1815.

Bachu, S., D. Bonijoly, J. Bradshaw, R. Burruss, S. Holloway, N. P. Christensen, and O. M. Mathiassen (2007), Co2 storage capacity estimation: Methodology and gaps, *International Journal of Greenhouse Gas Control*, *1*(4), 430 – 443, doi:https://doi.org/10.1016/S1750-5836(07)00086-2.

Backhaus, S., K. Turitsyn, and R. E. Ecke (2011), Convective instability and mass transport of diffusion layers in a Hele-Shaw geometry, *Physical Review Letters*, doi:10.1103/PhysRevLett.106.104501.

Baines, S. J., and R. H. Worden (2004), The long-term fate of co2 in the subsurface: natural analogues for co2 storage, *Geological Society, London, Special Publications*, *233*(1), 59–85.

Brainard, J. (2018), News at a glance, *Science*, *362*(6414), 504–506, doi:10.1126/science.362.6414.504.

Celia, M. A., S. Bachu, J. M. Nordbotten, and K. W. Bandilla (2015), Status of CO2 storage in deep saline aquifers with emphasis on modeling approaches and practical simulations, *Water Resources Research*, doi:10.1002/2015WR017609.

Chadwick, R., P. Zweigel, U. Gregersen, G. Kirby, S. Holloway, and P. Johannessen (2004), Geological reservoir characterization of a co2 storage site: The utsira sand, sleipner, northern north sea, *Energy*, *29*(9-10), 1371–1381.

Chen, C., L. Zeng, and L. Shi (2013), Continuum-scale convective mixing in geological CO2 sequestration in anisotropic and heterogeneous saline aquifers, *Advances in Water Resources*, doi:10.1016/j.advwatres.2012.10.012.

Cheng, P., M. Bestehorn, and A. Firoozabadi (2012), Effect of permeability anisotropy on buoyancy-driven flow for CO 2 sequestration in saline aquifers, *Water Resources Research*, doi:10.1029/2012WR011939.

De Paoli, M., F. Zonta, and A. Soldati (2017), Dissolution in anisotropic porous media: Modelling convection regimes from onset to shutdown, *Physics of Fluids*, *29*(2), 026,601.

Deutsch, C. V., A. G. Journel, et al. (1992), Geostatistical software library and user's guide, *New York*, *119*(147), 578.

Elenius, M., and S. E. Gasda (2021), Convective mixing driven by non-monotonic density, *Transport in Porous Media*, *138*(1), 133–155.

Elenius, M. T., and S. E. Gasda (2013), Convective mixing in formations with horizontal barriers, *Advances in Water Resources*, doi:10.1016/j.advwatres.2013.10.010.

Elenius, M. T., and K. Johannsen (2012), On the time scales of nonlinear instability in miscible displacement porous media flow, *Computational Geosciences*, doi: 10.1007/s10596-012-9294-2.

Elenius, M. T., J. M. Nordbotten, and H. Kalisch (2012), Effects of a capillary transition zone on the stability of a diffusive boundary layer, *IMA Journal of Applied Mathematics (Institute of Mathematics and Its Applications)*, doi:10.1093/imamat/hxs054.

Elenius, M. T., J. M. Nordbotten, and H. Kalisch (2014), Convective mixing influenced by the capillary transition zone, *Computational Geosciences*, doi:10.1007/s10596-014-9415-1.

Elenius, M. T., D. V. Voskov, and H. A. Tchelepi (2015), Interactions between gravity currents and convective dissolution, *Advances in Water Resources*, doi:10.1016/j.advwatres.2015.05.006.

Elgahawy, Y., and J. Azaiez (2021), Dynamics of buoyancy driven miscible iso-viscous flows in heterogeneous layered porous media, *Physics of Fluids*, *33*(7), 074,104.

Emami-Meybodi, H. (2017), Stability analysis of dissolution-driven convection in porous media, *Physics of Fluids*, *29*(1), 014,102.

Emami-Meybodi, H., and H. Hassanzadeh (2015), Two-phase convective mixing under a buoyant plume of co2 in deep saline aquifers, *Advances in Water Resources*, *76*, 55 – 71, doi:https://doi.org/10.1016/j.advwatres.2014.11.011.

Ennis-King, J., and L. Paterson (2003), Role of convective mixing in the long-term storage of carbon dioxide in deep saline formations, in *SPE Annual Technical Conference and Exhibition?*, pp. SPE–84,344, SPE.

Ennis-King, J., and L. Paterson (2005), Role of convective mixing in the long-term storage of carbon dioxide in deep saline formations, *SPE Journal*, doi:10.2118/84344-PA.

Erfani, H., M. Babaei, C. F. Berg, and V. Niasar (2022), Scaling co2 convection in confined aquifers: Effects of dispersion, permeability anisotropy and geochemistry, *Advances in Water Resources*, *164*, 104,191.

European Commission (2014), General union environment action programme to 2020. living well, within the limits of our planet, *1386/2013/EU. 2013, The 7th Environment Action Programme: European Union*, p. 30.

Farajzadeh, R., P. Ranganathan, P. L. Zitha, and J. Bruining (2011), The effect of heterogeneity on the character of density-driven natural convection of CO2 overlying a brine layer, *Advances in Water Resources*, doi:10.1016/j.advwatres.2010.12.012.

Farajzadeh, R., B. Meulenbroek, D. Daniel, A. Riaz, and J. Bruining (2013), An empirical theory for gravitationally unstable flow in porous media, *Computational Geosciences*, doi:10.1007/s10596-012-9336-9.

Frykman, P., and D. Wessel-Berg (2014), Dissolution trapping-convection enhancement limited by geology, *Energy Procedia*, *63*, 5467–5478.

Fu, X., L. Cueto-Felgueroso, and R. Juanes (2013), Pattern formation and coarsening dynamics in three-dimensional convective mixing in porous media, *Philosophical Transactions of the Royal Society A: Mathematical, Physical and Engineering Sciences*, *371*(2004), 20120,355.

Garcia, J. E. (2003), Fluid Dynamics of Carbon Dioxide Disposal into Saline Aquifers, *TH: Thesis (Ph.D.); Submitted to the University of California, Berkeley, CA (US); PBD: 18 Dec 2003*.

Gasda, S. E., J. M. Nordbotten, and M. A. Celia (2011), Vertically averaged approaches for CO2 migration with solubility trapping, doi:10.1029/2010WR009075.

Gasda, S. E., J. M. Nordbotten, and M. A. Celia (2012), Application of simplified models to CO 2 migration and immobilization in large-scale geological systems, *International Journal of Greenhouse Gas Control*, doi:10.1016/j.ijggc.2012.03.001.

Gilfillan, S. M., B. S. Lollar, G. Holland, D. Blagburn, S. Stevens, M. Schoell, M. Cassidy, Z. Ding, Z. Zhou, G. Lacrampe-Couloume, and C. J. Ballentine (2009), Solubility trapping in formation water as dominant CO2 sink in natural gas fields, *Nature*, doi: 10.1038/nature07852.

Green, C. P., and J. Ennis-King (2010), Effect of vertical heterogeneity on long-term migration of CO2 in saline formations, *Transport in Porous Media*, doi:10.1007/s11242-009-9498-7.

Green, C. P., and J. Ennis-King (2014), Steady dissolution rate due to convective mixing in anisotropic porous media, *Advances in Water Resources*, doi:10.1016/j.advwatres.2014.07.002.

Hansen, S. K., Y. Tao, and S. Karra (2023), Impacts of permeability heterogeneity and background flow on supercritical co2 dissolution in the deep subsurface, *Water Resources Research*, *59*(11), e2023WR035,394.

Hassanzadeh, H., M. Pooladi-Darvish, and D. W. Keith (2007), Scaling behavior of convective mixing, with application to geological storage of CO2, *AIChE Journal*, doi: 10.1002/aic.11157.

Hassanzadeh, H., M. Pooladi-Darvish, A. M. Elsharkawy, D. W. Keith, and Y. Leonenko (2008), Predicting PVT data for CO2-brine mixtures for black-oil simulation of CO2 geological storage, *International Journal of Greenhouse Gas Control*, doi: 10.1016/S1750-5836(07)00010-2.

Hesse, M. (2008), Mathematical modeling and multiscale simulation for co2 storage in saline aquifers, Ph.D. thesis, Stanford, CA: Department of Energy Resources Engineering, Stanford University.

Hidalgo, J. J., and J. Carrera (2009), Effect of dispersion on the onset of convection during co2 sequestration, *Journal of Fluid Mechanics*, *640*, 441–452.

Iding, M., and P. Ringrose (2010), Evaluating the impact of fractures on the performance of the in salah co2 storage site, *International Journal of Greenhouse Gas Control*, *4*(2), 242–248.

Jafari Raad, S. M., H. Emami-Meybodi, and H. Hassanzadeh (2016), On the choice of analogue fluids in co2 convective dissolution experiments, *Water Resources Research*, *52*(6), 4458–4468, doi:10.1002/2015WR018040.

Jenkins, C., A. Chadwick, and S. D. Hovorka (2015), The state of the art in monitoring and verification—ten years on, *International Journal of Greenhouse Gas Control*, *40*, 312–349.

Journel, A., and C. Huijbregts (1976), Mining geostatistics.

Kim, M., K. Y. Kim, W. S. Han, J. Oh, and E. Park (2019), Density-Driven Convection in a Fractured Porous Media: Implications for Geological CO2 Storage, *Water Resources Research*, doi:10.1029/2019WR024822.

Kim, M. C. (2014), Onset of buoyancy-driven convection in a liquid-saturated cylindrical anisotropic porous layer supported by a gas phase, *Transport in porous media*, *102*(1), 31–42.

Knudby, C., and J. Carrera (2005), On the relationship between indicators of geostatistical, flow and transport connectivity, *Advances in Water Resources*, *28*(4), 405 – 421, doi:https://doi.org/10.1016/j.advwatres.2004.09.001.

Kong, X. Z., and M. O. Saar (2013), Numerical study of the effects of permeability heterogeneity on density-driven convective mixing during CO2 dissolution storage, *International Journal of Greenhouse Gas Control*, doi:10.1016/j.ijggc.2013.08.020.

Kumagai, A., and C. Yokoyama (1999), Viscosities of aqueous NaCl solutions containing CO2 at high pressures, *Journal of Chemical and Engineering Data*, doi: 10.1021/je980178p.

Kumar, A., R. Ozah, M. Noh, G. A. Pope, S. Bryant, K. Sepehmoori, and L. W. Lake (2005), Reservoir simulation of CO2 storage in deep saline aquifers, *SPE Journal*, doi: 10.2118/89343-pa.

Lapwood, E. (1948), Convection of a fluid in a porous medium, in *Mathematical proceedings of the cambridge philosophical society*, vol. 44, pp. 508–521, Cambridge University Press.

Lin, C.-P., C.-F. Ni, I.-H. Lee, and W.-C. Li (2016), Effects of permeability variations on co 2 convection in anisotropic and heterogeneous saline formations., *Terrestrial, Atmospheric & Oceanic Sciences*, *27*(1).

Lindeberg, E., and P. Bergmo (2003), The Long-Term Fate of CO2 Injected into an Aquifer, in *Greenhouse Gas Control Technologies - 6th International Conference*, doi: 10.1016/b978-008044276-1/50078-7.

Lindeberg, E., and D. Wessel-Berg (1997), Vertical convection in an aquifer column under a gas cap of co2, *Energy Conversion and Management*, *38*, S229 – S234, doi: https://doi.org/10.1016/S0196-8904(96)00274-9, proceedings of the Third International Conference on Carbon Dioxide Removal.

Lindeberg, E., and D. Wessel-Berg (2011), Upscaling studies of diffusion induced convection in homogeneous and heterogeneous aquifers, *Energy Procedia*, *4*, 3927–3934.

Liyanage, R. (2018), Convective dissolution in porous media: three-dimensional imaging experiments and numerical simulations, Ph.D. thesis, Imperial College London.

Macminn, C. W., and R. Juanes (2013), Buoyant currents arrested by convective dissolution, *Geophysical Research Letters*, doi:10.1002/grl.50473.

Mahyapour, R., S. Mahmoodpour, M. Singh, and S. Omrani (2022), Effect of permeability heterogeneity on the dissolution process during carbon dioxide sequestration in saline aquifers: two-and three-dimensional structures, *Geomechanics and Geophysics for Geo-Energy and Geo-Resources*, *8*(2), 1–22.

Maldal, T., and I. Tappel (2004), Co2 underground storage for snøhvit gas field development, *Energy*, *29*(9-10), 1403–1411.

Martinez, M. J., and M. A. Hesse (2016), Two-phase convective co2 dissolution in saline aquifers, *Water Resources Research*, *52*(1), 585–599, doi:10.1002/2015WR017085.

Matacic, C. (2018), News at a glance, *Science*, *362*(6421), 1334–1336, doi:10.1126/science.362.6421.1334.

Mathieson, A., I. Wright, D. Roberts, and P. Ringrose (2009), Satellite imaging to monitor co2 movement at krechba, algeria, *Energy Procedia*, *1*(1), 2201–2209.

Michel-Meyer, I., U. Shavit, A. Tsinober, and R. Rosenzweig (2020), The role of water flow and dispersive fluxes in the dissolution of co2 in deep saline aquifers, *Water Resources Research*, *56*(11), e2020WR028,184.

Neufeld, J. A., M. A. Hesse, A. Riaz, M. A. Hallworth, H. A. Tchelepi, and H. E. Huppert (2010), Convective dissolution of carbon dioxide in saline aquifers, *Geophysical Research Letters*, *37*(22), doi:10.1029/2010GL044728.

Nicot, J.-P. (2008), Evaluation of large-scale co2 storage on fresh-water sections of aquifers: An example from the texas gulf coast basin, *International Journal of Greenhouse Gas Control*, *2*(4), 582–593.

Nield, D. A., C. T. Simmons, A. V. Kuznetsov, and J. D. Ward (2008), On the evolution of salt lakes: Episodic convection beneath an evaporating salt lake, *Water Resources Research*, doi:10.1029/2007WR006161.

Pau, G. S., J. B. Bell, K. Pruess, A. S. Almgren, M. J. Lijewski, and K. Zhang (2010), High-resolution simulation and characterization of density-driven flow in co2 storage in saline aquifers, *Advances in Water Resources*, *33*(4), 443 – 455, doi:https://doi.org/10.1016/j.advwatres.2010.01.009.

Phillips, S. L., A. Igbene, J. A. Fair, H. Ozbek, and M. Tavana (1982), Technical Databook for Geothermal energy utilization., in *Proceedings of the Symposium on Thermophysical Properties*.

Prasad, A., and C. T. Simmons (2003), Unstable density-driven flow in heterogeneous porous media: A stochastic study of the elder [1967b]"short heater" problem, *Water Resources Research*, *39*(1), SBH–4.

Pritchard, D. (2007), Gravity currents over fractured substrates in a porous medium, *Journal of Fluid Mechanics*, doi:10.1017/S0022112007006623.

Pruess, K. (2005), Numerical studies of fluid leakage from a geologic disposal reservoir for CO2 show self-limiting feedback between fluid flow and heat transfer, *Geophysical Research Letters*, doi:10.1029/2005GL023250.

Pruess, K., and J. Nordbotten (2011), Numerical Simulation Studies of the Long-term Evolution of a CO2 Plume in a Saline Aquifer with a Sloping Caprock, *Transport in Porous Media*, doi:10.1007/s11242-011-9729-6.

Pruess, K., and K. Zhang (2008), Numerical Modeling Studies of The Dissolution-Diffusion-Convection Process During CO2 Storage in Saline Aquifers, *Lawrence Berkeley National Laboratory*.

Ranganathan, P., R. Farajzadeh, H. Bruining, and P. L. Zitha (2012), Numerical Simulation of Natural Convection in Heterogeneous Porous media for CO 2 Geological Storage, *Transport in Porous Media*, doi:10.1007/s11242-012-0031-z.

Rasmusson, M., F. Fagerlund, Y. Tsang, K. Rasmusson, and A. Niemi (2015), Prerequisites for density-driven instabilities and convective mixing under broad geological CO2 storage conditions, *Advances in Water Resources*, doi:10.1016/j.advwatres.2015.08.009.

Rasmusson, M., F. Fagerlund, K. Rasmusson, Y. Tsang, and A. Niemi (2017), Refractive-Light-Transmission Technique Applied to Density-Driven Convective Mixing in Porous Media With Implications for Geological CO2 Storage, *Water Resources Research*, doi: 10.1002/2017WR020730.

Renard, P., and G. de Marsily (1997), Calculating equivalent permeability: a review, *Advances in Water Resources*, *20*(5), 253–278, doi:https://doi.org/10.1016/S0309-1708(96)00050-4.

Riaz, A., M. HESSE, H. A. TCHELEPI, and F. M. ORR (2006), Onset of convection in a gravitationally unstable diffusive boundary layer in porous media, *Journal of Fluid Mechanics*, *548*, 87–111, doi:10.1017/S0022112005007494.

Saaltink, M. W., V. Vilarrasa, F. De Gaspari, O. Silva, J. Carrera, and T. S. Rötting (2013), A method for incorporating equilibrium chemical reactions into multiphase flow models for co2 storage, *Advances in Water Resources*, *62*, 431 – 441, doi: https://doi.org/10.1016/j.advwatres.2013.09.013, computational Methods in Geologic CO2 Sequestration.

Salibindla, A. K. R., R. Subedi, V. C. Shen, A. U. M. Masuk, and R. Ni (2018), Dissolution-driven convection in a heterogeneous porous medium, *Journal of Fluid Mechanics*, *857*, 61–79, doi:10.1017/jfm.2018.732.

Sanchez-Vila, X., A. Guadagnini, and J. Carrera (2006), Representative hydraulic conductivities in saturated groundwater flow, *Reviews of Geophysics*, *44*(3), doi: https://doi.org/10.1029/2005RG000169.

Sathaye, K. J., M. A. Hesse, M. Cassidy, and D. F. Stockli (2014), Constraints on the magnitude and rate of co2 dissolution at bravo dome natural gas field, *Proceedings of the National Academy of Sciences*, *111*(43), 15,332–15,337.

Schincariol, R. A., F. W. Schwartz, and C. A. Mendoza (1997), Instabilities in variable density flows: Stability and sensitivity analyses for homogeneous and heterogeneous media, *Water resources research*, *33*(1), 31–41.

Simmons, C. T., K. A. Narayan, and R. A. Wooding (1999), On a test case for density-dependent groundwater flow and solute transport models: The salt lake problem, *Water Resources Research*, doi:10.1029/1999WR900254.

Simmons, C. T., T. R. Fenstemaker, and J. M. Sharp Jr (2001), Variable-density groundwater flow and solute transport in heterogeneous porous media: approaches, resolutions and future challenges, *Journal of contaminant hydrology*, *52*(1-4), 245–275.

Slim, A. C. (2014), Solutal-convection regimes in a two-dimensional porous medium, *Journal of Fluid Mechanics*, *741*, 461–491, doi:10.1017/jfm.2013.673.

Soltanian, M. R., M. A. Amooie, N. Gershenzon, Z. Dai, R. Ritzi, F. Xiong, D. Cole, and J. Moortgat (2017), Dissolution Trapping of Carbon Dioxide in Heterogeneous Aquifers, *Environmental Science and Technology*, doi:10.1021/acs.est.7b01540.

Spycher, N., and K. Pruess (2005), CO2-H2O mixtures in the geological sequestration of CO2. II. Partitioning in chloride brines at 12-100°C and up to 600 bar, *Geochimica et Cosmochimica Acta*, doi:10.1016/j.gca.2005.01.015.

Spycher, N., K. Pruess, and J. Ennis-King (2003), CO2-H2O mixtures in the geological sequestration of CO2. I. Assessment and calculation of mutual solubilities from 12 to 100°C and up to 600 bar, *Geochimica et Cosmochimica Acta*, doi: 10.1016/S0016-7037(03)00273-4.

Strandli, C. W., and S. M. Benson (2013), Identifying diagnostics for reservoir structure and CO2 plume migration from multilevel pressure measurements, *Water Resources Research*, doi:10.1002/wrcr.20285.

Taheri, A., D. Wessel-Berg, O. Torsaeter, and M. Soroush (2012), The effects of anisotropy and heterogeneity on CO2 dissolution in deep saline aquifers, in *Society of Petroleum Engineers - Carbon Management Technology Conference 2012*, doi:10.7122/151345-ms.

Taheri, A., O. Torsæter, E. Lindeberg, N. J. Hadia, and D. Wessel-Berg (2018), Qualitative and quantitative experimental study of convective mixing process during storage of co2 in heterogeneous saline aquifers, *International Journal of Greenhouse Gas Control*, *71*, 212–226.

Tewes, F., and F. Boury (2005), Formation and rheological properties of the supercritical co2- water pure interface, *The Journal of Physical Chemistry B*, *109*(9), 3990–3997.

Tsai, P. A., K. Riesing, and H. A. Stone (2013), Density-driven convection enhanced by an inclined boundary: Implications for geological CO2 storage, *Physical Review E - Statistical, Nonlinear, and Soft Matter Physics*, doi:10.1103/PhysRevE.87.011003.

Tsinober, A., R. Rosenzweig, H. Class, R. Helmig, and U. Shavit (2022), The role of mixed convection and hydrodynamic dispersion during co2 dissolution in saline aquifers: A numerical study, *Water Resources Research*, *58*(3), e2021WR030,494.

Tutolo, B. M., A. J. Luhmann, X.-Z. Kong, M. O. Saar, and W. E. Seyfried Jr (2014), Experimental observation of permeability changes in dolomite at co2 sequestration conditions, *Environmental science & technology*, *48*(4), 2445–2452.

Tutolo, B. M., A. J. Luhmann, X.-Z. Kong, M. O. Saar, and W. E. Seyfried Jr (2015a), Co2 sequestration in feldspar-rich sandstone: coupled evolution of fluid chemistry, mineral reaction rates, and hydrogeochemical properties, *Geochimica et Cosmochimica Acta*, *160*, 132–154.

Tutolo, B. M., X.-Z. Kong, W. E. Seyfried Jr, and M. O. Saar (2015b), High performance reactive transport simulations examining the effects of thermal, hydraulic, and chemical (thc) gradients on fluid injectivity at carbonate ccus reservoir scales, *International Journal of Greenhouse Gas Control*, *39*, 285–301.

Vella, D., and H. E. Hupper (2006), Gravity currents in a porous medium at an inclined plane, *Journal of Fluid Mechanics*, doi:10.1017/S0022112006009578.

Vilarrasa, V. (2012), Thermo-hydro-mechanical impacts of carbon dioxide (co2) injection in deep saline aquifers, Ph.D. thesis, Technical University of Catalonia.

Vilarrasa, V., and J. Carrera (2015), Geologic carbon storage is unlikely to trigger large earthquakes and reactivate faults through which co2 could leak, *Proceedings of the National Academy of Sciences*, *112*(19), 5938–5943.

Vilarrasa, V., D. Bolster, S. Olivella, and J. Carrera (2010), Coupled hydromechanical modeling of co2 sequestration in deep saline aquifers, *International Journal of Greenhouse Gas Control*, *4*(6), 910 – 919, doi:https://doi.org/10.1016/j.ijggc.2010.06.006, cO2 Storage at the EGU General Assembly 2009.

Vilarrasa, V., O. Silva, J. Carrera, and S. Olivella (2013), Liquid co2 injection for geological storage in deep saline aquifers, *International Journal of Greenhouse Gas Control*, *14*, 84–96.

Vilarrasa, V., S. Olivella, J. Carrera, and J. Rutqvist (2014), Long term impacts of cold co2 injection on the caprock integrity, *International Journal of Greenhouse Gas Control*, *24*, 1–13.

Wang, S., C. Zucheng, Y. Zhang, L. Jiang, Y. Liu, and S. Yongchen (2021), Unstable Density-Driven Convection of CO 2 in Homogeneous and Heterogeneous Porous Media with Implications for Deep Saline Aquifers , *Water Resources Research*, doi: 10.1029/2020wr028132.

Wang, Y. (2022), Numerical Modeling of Geological Carbon Sequestration: Enhanced Dissolution in Randomly Heterogeneous Media, doi:10.5281/zenodo.6769788.

Wang, Y., D. Fernàndez-Garcia, and M. W. Saaltink (2022), Carbon dioxide (co2) dissolution efficiency during geological carbon sequestration (gcs) in randomly stratified formations, *Water Resources Research*, *58*(8), e2022WR032,325.

Wang, Y., D. Fernàndez-Garcia, and M. W. Saaltink (2023), Modeling reactive multi-component multi-phase flow for geological carbon sequestration (gcs) with matlab, *Computers & Geosciences*, p. 105300.

Weir, G. J., S. P. White, and W. M. Kissling (1996), Reservoir storage and containment of greenhouse gases, *Transport in Porous Media*, doi:10.1007/BF00145265.

Würdemann, H., F. Möller, M. Kühn, W. Heidug, N. P. Christensen, G. Borm, F. R. Schilling, C. Group, et al. (2010), Co2sink—from site characterisation and risk assessment to monitoring and verification: One year of operational experience with the field laboratory for co2 storage at ketzin, germany, *International Journal of Greenhouse Gas Control*, *4*(6), 938–951.

Xiao, T., B. McPherson, R. Esser, W. Jia, N. Moodie, S. Chu, and S.-Y. Lee (2019), Forecasting commercial-scale co2 storage capacity in deep saline reservoirs: Case study of buzzard's bench, central utah, *Computers & Geosciences*, *126*, 41–51.

Xu, T., J. A. Apps, K. Pruess, and H. Yamamoto (2007), Numerical modeling of injection and mineral trapping of co2 with h2s and so2 in a sandstone formation, *Chemical Geology*, *242*(3-4), 319–346.

Xu, X., S. Chen, and D. Zhang (2006), Convective stability analysis of the long-term storage of carbon dioxide in deep saline aquifers, *Advances in Water Resources*, doi: 10.1007/s11432-006-0397-z.

Yan, M., C. Lu, J. Yang, Y. Xie, and J. Luo (2019), Impact of low-or high-permeability inclusion on free convection in a porous medium, *Geofluids*, *2019*.

Zhang, H., and F. W. Schwartz (1995), Multispecies Contaminant Plumes in Variable Density Flow Systems, *Water Resources Research*, doi:10.1029/94WR02567.

Supporting Information for " Numerical Analysis of the Effect of Heterogeneity on CO_2 Dissolution Enhanced by Gravity Driven Convection"

Yufei Wang[1,2] Daniel Fernàndez-Garcia[1,2] Maarten W. Saaltink[1,2]

[1]Dept. of Civil and Environmental Engineering, Universitat Politècnica de Catalunya, Jordi Girona 1-3, 08034 Barcelona, Spain

[2]Associated Unit: Hydrogeology Group (UPC-CSIC)

Contents of this file

Introduction

This supporting information is comprised of two sections. The first section (S1) shows how to choose the grid size for numerical simulation, and the second section (S2) gives detailed results on gravity driven convection in homogeneous fields.

Text S1: Optimum Setup Design

An optimum setup design could represent the Gravity Driven Convection (GDC) with smallest number of grids and shortest simulation time. To get a good setup design we need to know both the behavior of the GDC and the properties of the field and the fluid.

First, two basic features of GDC are used as references in designing the simulation setup. We use characteristic wave length (or earliest finger width) ℓ_c to assist designing the grid and domain sizes, and use the characteristic onset time τ_c to assist setting the simulation time. They are, respectively, given as

$$\ell_c = \ell_c^* \frac{\mu\phi D}{\Delta\rho g \kappa_g} \tag{1}$$

and

$$\tau_c = \tau_c^* \frac{(\mu\phi)^2 D}{(\Delta\rho g \kappa_g)^2}, \tag{2}$$

where, ℓ_c^* and τ_c^* are, respectively, dimensionless characteristic wavelength and onset time, which are constants obtained from theoretical, numerical or experimental studies; μ is the viscosity; ϕ is the porosity; D is the diffusion coefficient; $\Delta\rho$ is the maximum density increase due to CO_2 dissolution; g is the gravitational acceleration; κ_g is the geometric mean permeability. For homogeneous media, the empirical values for ℓ_c^* and τ_c^* are listed in Table S1, which also contains the results from this study.

The domain size should be large enough to cover enough number of convection fingers, while the grid size should be smaller than or close to the size of convection fingers. From our testing simulations (see Figures S1 and S2), we find that the domain size of $30L_c \times 30L_c$ and grid size of $0.3L_c \times 0.3L_c$ are enough to describe the GDC. Increasing the domain size to $60L_c \times 30L_c$ and $30L_c \times 60L_c$ or reducing the grid size to $0.15L_c \times 0.3L_c$, $0.3L_c \times 0.15L_c$

and $0.15L_c \times 0.075L_c$ does not systematically affect the onset time and dissolution rate. We notice that reducing or increasing the (especially vertical) grid size could significantly affect the characteristic wave length (i.e., the width of earliest unstable fingers) but this does not affect the statistic dissolution rate. Results from Elenius et al. (2015) show that the dissolution can be correctly simulated even if the grid size is several times larger than the characteristic wave length, although the concentration profile is not precisely represented. For homogeneous fields, a simulation time of $6\tau_c$ is enough to obtain the asymptotic dissolution rate. For heterogeneous fields, the simulation is not terminated until the fast unstable finger touches the bottom, to make sure the finger has ergodically traveled the heterogeneous domain; here, we define the finger has touched the bottom when the maximum CO_2(aq) concentration on the bottom increases to 25% of the maximum CO_2(aq) concentration.

Second, for numerical simulations in heterogeneous fields, we need also to take into account the correlation length scale. The domain size should be, if possible, 4 times larger than the correlation length scale which should be at least 5 times larger than the grid size. Because the domain size is $30L_c$, the correlation length should be less than $10L_c$. Because the grid size is $0.3L_c$, the minimum correlation length is $1.5L_c$. Here, maximum employed correlation length is $8L_c$ and minimum employed correlation length is $2L_c$. Additionally, the horizontally layered formation is used to represent the infinite correlation length in the horizontal direction.

Text S2: Gravity-Driven Convection in Reference Homogeneous Fields

We begin the analysis of Gravity-Driven Convection (GDC) from the results in homogeneous fields. The analysis of GDC in homogeneous field is given for two reasons. First, the analysis on GDC in homogeneous field serves as benchmark of the numerical algorithm, since it has been well studied in literature. Second, it shares the general behavior of GDC, and thus it serves as reference for the heterogeneous field.

From Figure S3, we can see that the dimensionless dissolution rate in homogeneous media (F^*) initially follows the pure diffusion function, until when $t^* \approx 500$, after that, the dissolution rate increases due to the gravity driven convection enhances the dissolution rate. The dissolution rate finally reaches the asymptotic value of around 0.09. This dissolution rate ($F^* \approx$0.09) obtained in this work is slightly larger than 0.075 in Elenius & Johannsen (2012) and 0.065 in Martinez & Hesse (2016); in the latter the Capillary Transition Zone (CTZ) boundary is employed. If we compare the dissolution rate to the vertical and horizontal finger velocities, we can see that the increase of dissolution rate is accompanied by the increase of the vertical and horizontal finger velocities. This implies that the dissolution rate is dominated by advection when gravity-driven instability appears. The vertical finger velocity is around 0.30, which is larger than 0.21 obtained in Elenius & Johannsen (2012), because impermeable top boundary is employed in the latter study.

Here, we specially note that the onset time for the enhanced dissolution is defined as nonlinear onset time, which is the time when instability fingers emerge (Elenius & Johannsen, 2012). If we observe the middle panel of Figure S3, we can find that the vertical finger velocity first decreases and then increases at around $t^* = 250$. Hidalgo & Carrera

(2009) also show the flow rate initially decreases and then increases to a constant value. The time at the inflection point is defined as linear onset time (Elenius & Johannsen, 2012). Here, we only consider the nonlinear onset time because it is more related to the dissolution efficiency in practice. The nonlinear onset time is affected by the initial perturbation, the field heterogeneity and the computational accuracy. For the real heterogeneous field, the nonlinear onset time is negligibly small, as shown in the paper supported by this document.

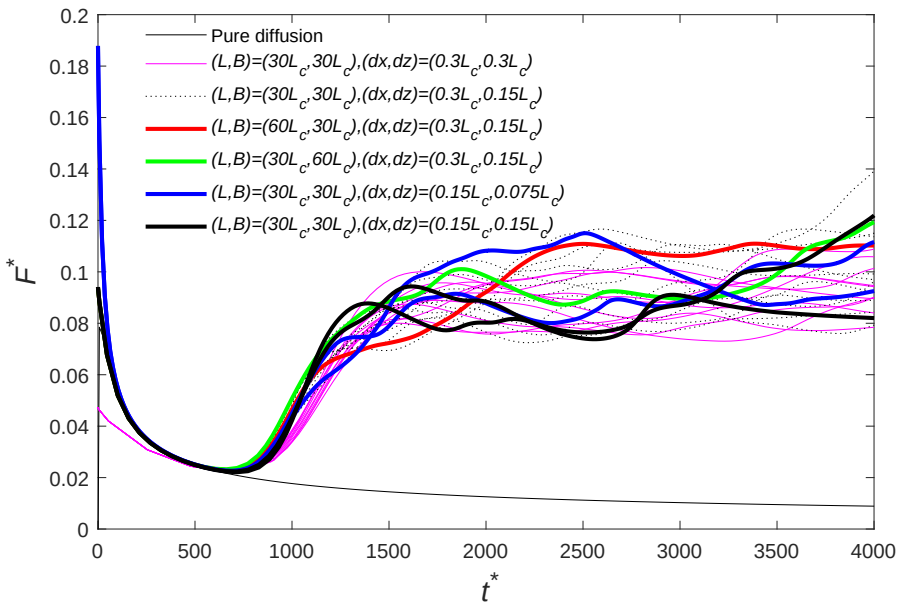

Figure S1: Analysis of the effect of grid size on the the dissolution rate.

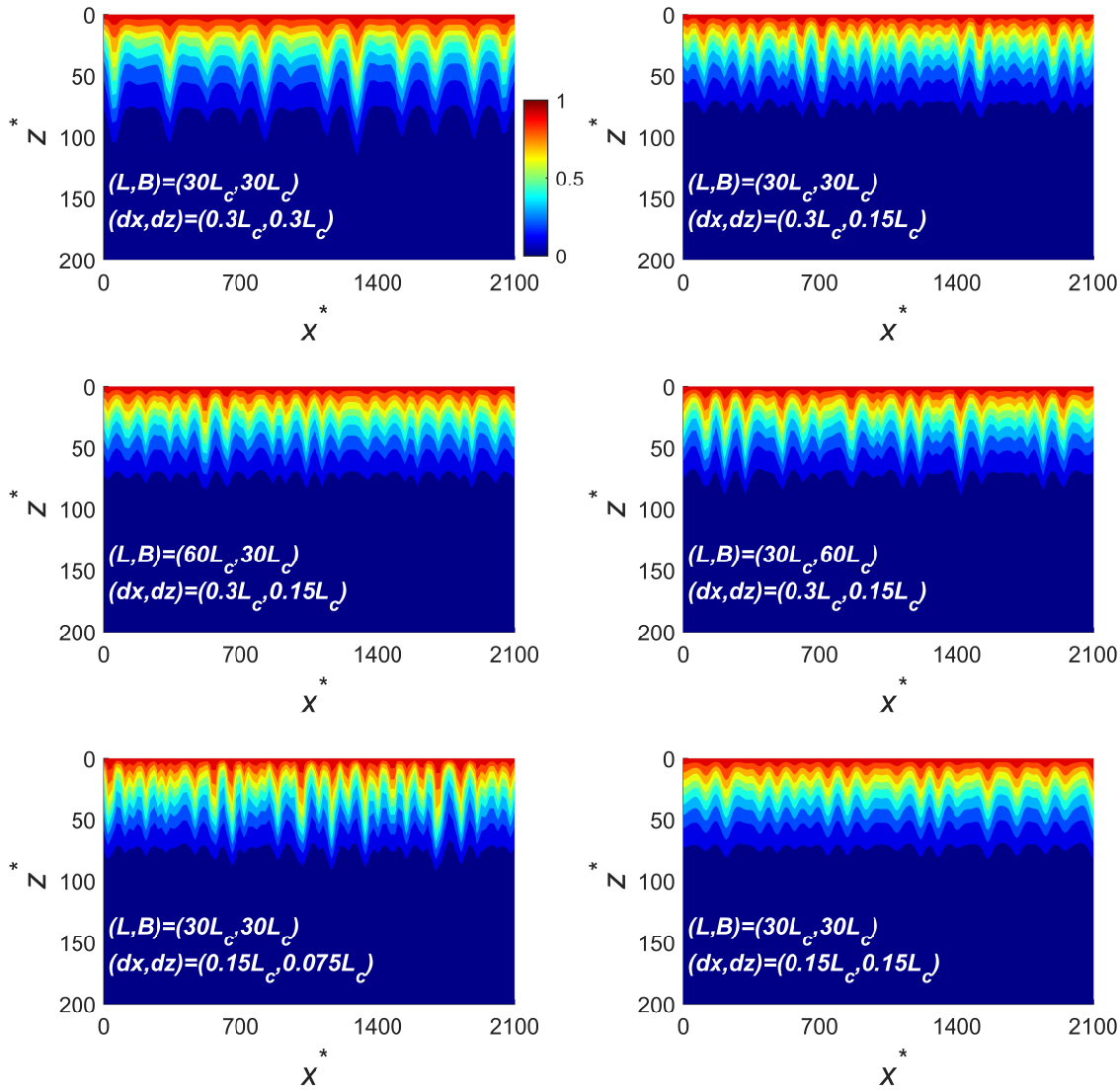

Figure S2: Analysis of the effect of grid size on the finger size(for the case of $(L, B) = (60L_c, 30L_c), (dx, dz) = (0.3L_c, 0.15L_c)$, we only show $x \in (0, 30L_c)$).

Table S1: Published data for dimensionless onset time (τ_c^*) and dimensionless wave length (ℓ_c^*) for (isotropic) homogeneous field.

Onset time (τ_c^*)	**Wave length** (ℓ_c^*)	**Top boundary**	**Method**	**Reference**
30,75	95	-	Theor.	Ennis-King et al. (2005)
78	92	-	Theor.	Ennis-King & Paterson (2005)
75	96	-	Theor.	Xu et al. (2006)
1,156- 1,412	34-38	diff. only[a]	Num.	Pruess & Zhang (2008)
146	90	-	Theor.	Riaz et al. (2006)
1,000- 5,000	-	diff. only	Num.	Pau et al. (2010)
47.9	115.3	-	Theor.	Cheng et al. (2012)
3,500	-	diff. only	Num..	Cheng et al. (2012)
4,860	170	diff. only	Num.	Elenius & Johannsen (2012)
31	73	-	Theor.	Elenius et al. (2012)
5800	-	diff. only	Num.	Elenius et al. (2012)
2500	-	CTZ[b]	Num.	Elenius et al. (2012)
845	-	diff. only	Num.	Azin et al. (2013)
1,200	80-140	diff. only	Num.	Slim (2014)
56	-	-	Theor.	Jafari Raad et al. (2016)
$Ra^{0.8573}$	-	Permeable	Exp.	Rasmusson et al. (2017)
500	70	Permeable	Num.	This study

[a] The top boundary only allows mass to go through the boundary via diffusion.

[b] The top boundary is capillary transition zone.

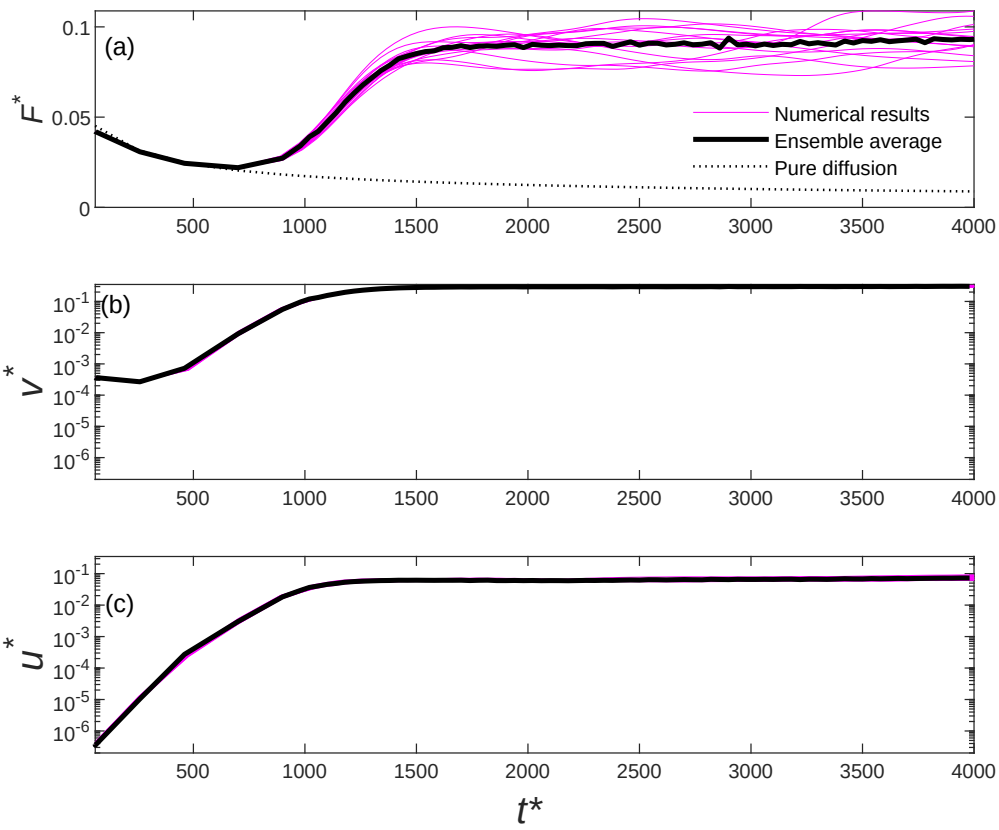

Figure S3: Homogeneous case: temporal developments of dimensionless dissolution rate (top), dimensionless vertical finger velocity (middle) and dimensionless horizontal finger velocity (bottom).

References

Azin, R., Raad, S. M. J., Osfouri, S., & Fatehi, R. (2013). Onset of instability in CO2 sequestration into saline aquifer: Scaling relationship and the effect of perturbed boundary. *Heat and Mass Transfer*. doi: 10.1007/s00231-013-1199-7

Cheng, P., Bestehorn, M., & Firoozabadi, A. (2012). Effect of permeability anisotropy on buoyancy-driven flow for CO 2 sequestration in saline aquifers. *Water Resources Research*. doi: 10.1029/2012WR011939

Elenius, M. T., & Johannsen, K. (2012). On the time scales of nonlinear instability in miscible displacement porous media flow. *Computational Geosciences*, *16*(4), 901-911. Retrieved from `https://doi.org/10.1007/s10596-012-9294-2` doi: 10.1007/s10596-012-9294-2

Elenius, M. T., Nordbotten, J. M., & Kalisch, H. (2012). Effects of a capillary transition zone on the stability of a diffusive boundary layer. *IMA Journal of Applied Mathematics (Institute of Mathematics and Its Applications)*. doi: 10.1093/imamat/hxs054

Elenius, M. T., Voskov, D. V., & Tchelepi, H. A. (2015). Interactions between gravity currents and convective dissolution. *Advances in Water Resources*. doi: 10.1016/j.advwatres.2015.05.006

Ennis-King, J., & Paterson, L. (2005). Role of convective mixing in the long-term storage of carbon dioxide in deep saline formations. *SPE Journal*. doi: 10.2118/84344-PA

Ennis-King, J., Preston, I., & Paterson, L. (2005). Onset of convection in anisotropic porous media subject to a rapid change in boundary conditions. *Physics of Fluids*. doi: 10.1063/1.2033911

Hidalgo, J. J., & Carrera, J. (2009). Effect of dispersion on the onset of convection during co2 sequestration. *Journal of Fluid Mechanics*, *640*, 441–452.

Jafari Raad, S. M., Emami-Meybodi, H., & Hassanzadeh, H. (2016). On the choice of analogue fluids in co2 convective dissolution experiments. *Water Resources Research*, *52*(6), 4458-4468. Retrieved from https://agupubs.onlinelibrary.wiley.com/doi/abs/10.1002/2015WR018040 doi: 10.1002/2015WR018040

Martinez, M. J., & Hesse, M. A. (2016). Two-phase convective co2 dissolution in saline aquifers. *Water Resources Research*, *52*(1), 585-599. Retrieved from https://agupubs.onlinelibrary.wiley.com/doi/abs/10.1002/2015WR017085 doi: 10.1002/2015WR017085

Pau, G. S., Bell, J. B., Pruess, K., Almgren, A. S., Lijewski, M. J., & Zhang, K. (2010). High-resolution simulation and characterization of density-driven flow in co2 storage in saline aquifers. *Advances in Water Resources*, *33*(4), 443 - 455. Retrieved from http://www.sciencedirect.com/science/article/pii/S0309170810000217 doi: https://doi.org/10.1016/j.advwatres.2010.01.009

Pruess, K., & Zhang, K. (2008). Numerical Modeling Studies of The Dissolution-Diffusion-Convection Process During CO2 Storage in Saline Aquifers. *Lawrence Berkeley National Laboratory*.

Rasmusson, M., Fagerlund, F., Rasmusson, K., Tsang, Y., & Niemi, A. (2017). Refractive-Light-Transmission Technique Applied to Density-Driven Convective Mixing in Porous Media With Implications for Geological CO2 Storage. *Water Resources Research*. doi: 10.1002/2017WR020730

Riaz, A., HESSE, M., TCHELEPI, H. A., & ORR, F. M. (2006). Onset of convection in a gravitationally unstable diffusive boundary layer in porous media. *Journal of Fluid Mechanics*, *548*, 87–111. doi: 10.1017/S0022112005007494

Slim, A. C. (2014). Solutal-convection regimes in a two-dimensional porous medium. *Journal*

of Fluid Mechanics, *741*, 461–491. doi: 10.1017/jfm.2013.673

Xu, X., Chen, S., & Zhang, D. (2006). Convective stability analysis of the long-term storage of carbon dioxide in deep saline aquifers. *Advances in Water Resources*. doi: 10.1007/s11432-006-0397-z